

# **Triana - a Deep Space Earth and Solar Observatory**

*Report prepared for the National Academy of Sciences by:*

*Francisco P. J. Valero, Jay Herman, Patrick Minnis, William D. Collins, Robert*

*Sadourny, Warren Wiscombe, Dan Lubin, and Keith Ogilvie*

*With contributions from members of the Triana Science Team*



## ***Triana Science Team:***

*Scripps Institution of Oceanography, University  
of California San Diego*

Francisco P. J. Valero, Triana Principal Investigator

Anthony Bucholtz

Brett C. Bush

Dan Lubin

Shelly K. Pope

V. Ramanathan

Sally K. Ride

*NASA Goddard Space Flight Center*

Jay Herman, GSFC Project Scientist

Keith Ogilvie

Warren J. Wiscombe

*National Institute of Standards and Technology*

Steven Lorentz

Joseph Rice

*NASA Langley Research Center*

Patrick Minnis

*NASA Ames Research Center*

Peter Pilewski

*National Center for Atmospheric Research*

William D. Collins

*Laboratoire de Meteorologie Dynamique, Ecole  
Normale Supérieure, France*

Claude Basdevant

Bernard Legras

Robert Sadourny

Hector Teitelbaum

*Lockheed Martin Advanced Technology Center*

John H. Doolittle

Keith D. Hutchison

*Los Alamos National Laboratory*

Sigfried A. W. Gerstl

*Virginia Polytechnic Institute*

G. Louis Smith

# TABLE OF CONTENTS

1. Overview.....	4
1.1 Vantage Point.....	5
1.2 Science Payload and Retrieved Quantities .....	6
1.3 Data Dissemination.....	7
2. Science Objectives in Brief.....	7
2.1 Earth’s Atmosphere and Surface with EPIC.....	7
2.2 Earth’s Radiation and Climate with NISTAR .....	9
2.3 Solar Wind and Space Weather with Plasma-Mag .....	10
3. Scientific Advantages of L-1 .....	12
3.1 Orbit Description .....	12
3.2 Scientific Significance of Triana’s Time and Space Domain.....	12
3.3 Advantages for Field Observations and Process Studies.....	19
4. Instrument Descriptions.....	20
4.1 EPIC.....	21
4.2 NISTAR.....	23
4.3 Relationship Between NISTAR and EPIC Data.....	23
4.4 Plasma-Mag .....	24
4.5 Data Characterization.....	26
5. Science Products .....	28
5.1 EPIC.....	28
5.1.1 Ozone .....	29
5.1.2 Aerosols .....	32
5.1.3 Cloud Phase and Particle Shape Characterization .....	37
5.1.4 Precipitable Water Vapor.....	40
5.1.5 Cloud Reflectivity.....	43
5.1.6 Ultraviolet Radiation.....	44
5.1.7 Hot Spot Analysis .....	47
5.1.8 Upper Atmosphere Dynamics.....	50
Planetary and Other Waves.....	50
The Polar Vortex.....	52
Ozone Miniholes.....	52
Filamentary Structure of the Vortex Edge.....	53
5.1.9 Advances in the Arctic from Triana.....	55
Stratospheric Ozone Depletion in the Arctic .....	55
Arctic Tropospheric Aerosols .....	56
Arctic Meteorology and Climate Change .....	57
5.1.10 Validation.....	59
5.2 NISTAR.....	60
5.2.1 Scientific Goals and Objectives.....	60
5.2.2 Global Change from NISTAR .....	62

5.2.3 Computation of Shortwave and Near-Infrared Albedo.....	63
5.2.4 Test of EOS-CERES Using NISTAR and EPIC.....	65
5.2.5 The Ratio of Near-Infrared to Visible Albedo: Implications for Climate .....	66
5.2.6 Tests of Radiative Transfer Models .....	70
5.3 Plasma-Mag .....	72
5.3.1 Scientific Goals and Objectives .....	74
5.3.2 Multi-Point Solar Wind and Space Weather Studies.....	75
5.3.3 Small-Scale Structures and High Time Resolution Measurements .....	76
5.3.4 Tangential Discontinuities .....	76
6. Data Distribution.....	77
Appendix A: Scripps-EPIC.....	81
I. Instrument Description .....	81
II. Radiometric Calibration Before Launch .....	83
III. In-Flight Calibration Using the Moon .....	84
Appendix B: Scripps-NISTAR .....	86
I. Design.....	86
II. Principle of Operation of the ACRs .....	87
III. Drop-Floor Algorithm.....	88
IV. Characterization and Calibration .....	88
V. NISTAR Performance.....	89
Appendix C: References .....	90
Appendix D: Acronyms .....	98

## 1. Overview

As early as 1960, Farquhar (1960, 1968) proposed L-1, the neutral gravity point between the Earth and the Sun, as an ideal deep space location for Earth and solar observations. Triana will be the first Earth-observing mission to L-1. From this stable vantage point, the satellite will have a continuous view of the entire sunlit face of the rotating Earth 1.5 million km away. Named for the sailor on Columbus's voyage who first spotted the New World, Triana is an exploratory mission to investigate the scientific and technological advantages of L-1 for Earth observation. The L-1 perspective provides a global, all-day view from sunrise to sunset, where daily climatological phenomenon will unfold in clear view of Triana's instrumentation. This will allow for continuous measurements over large areas for long periods of time – a viewpoint that is not possible from Low Earth Orbit (LEO) and Geosynchronous Earth Orbit (GEO) satellites. Hourly variations in the atmosphere will be clearly observed simultaneously over widely dispersed geographic areas.

Global climatic studies focus heavily on determining the interaction of incoming solar radiation with clouds and other constituents of the Earth's atmosphere. Triana is flying three scientific instruments that will make a broad set of measurements in this field, some unique to this mission, others collaborative with data from other sources, and some complementary to previous work. Taken together as a whole, this data will make significant advances in completing the "patchwork mosaic" of geographically and time-of-day restricted measurements collected by other observing platforms.

This paper discusses the unique features of the Triana deep space Earth and Solar observatory. The instrumentation is briefly described and some details are presented in the appendices. The planned retrievals are essentially similar to those possible from LEO and GEO, but with the unique added value of combining high time resolution and synoptic view (daytime only).

Triana will provide a global synoptic (i.e. simultaneous over the entire globe) view of water vapor, aerosols, column ozone, upper troposphere winds, stratospheric wave structures and circulation, cloud amount and properties, albedos, and aerosols, plus accurate broadband measurements of the Earth's reflected and emitted radiation from 0.2 to 100  $\mu\text{m}$ . This comprehensive and synoptic view of the Earth will enable us to test and develop new understanding of the climate system. The quantities retrieved from the

Triana measurements (data products) will be used to address a variety of scientific problems and generate new applications.

Triana carries a combination of three new instruments: the Scripps-Earth Polychromatic Imaging Camera (EPIC) 10-channel telescope-spectroradiometer, the Scripps-NIST Advanced Radiometer (NISTAR) four-channel radiometer (three absolute cavities plus one photo-diode), and the Goddard Space Flight Center (GSFC) Plasma-Mag solar weather magnetometer, electron spectrometer, and Faraday cup. Triana will obtain entirely new observations of the Earth's atmosphere and surface, its radiation balance, and the Earth's space environment. A small, highly capable spacecraft, the GSFC SMEX-Lite, will support the instruments in orbit and provide the data transmission capabilities.

### **1.1 Vantage Point**

Multispectral imagery and broadband radiometry from a deep space Lagrange-1 orbit (L-1) offer an exciting opportunity to look at the Earth in a bulk thermodynamic sense, particularly as an open system exchanging radiative energy with the Sun and space. "The Earth as a planet" astronomers would say, as opposed to the "pixelated" Earth. This is a fundamental scientific goal with very appealing prospects for Earth sciences. The location at L-1 is also ideal to monitor the Sun and study solar weather.

Triana will have a *continuous (from sunrise to sunset)* and *simultaneous* view of the sunlit face of the Earth as it rotates beneath the spacecraft. This ability alone gives the Triana observations a capability never available from any other spacecraft or Earth observing platform in the past. Additionally, Triana will always observe from the near retro-reflection position, a unique viewing geometry. Spectral images and radiometric measurements will be made to obtain important atmospheric environmental data (e.g., ozone, UV-irradiance at the Earth's surface, water vapor, aerosols, cloud height, etc.) and information related to the Earth's energy balance. Triana measurements will have the advantage of synoptic context, high temporal and spatial resolution, and accurate in-flight lunar calibrations. Except for the period immediately after launch, Triana will observe from near the retro-reflection position and gain a unique piece of the Earth's energy-balance data, along with having increased sensitivity to changes on the Earth's surface.

In this document we describe the questions that can be addressed by the Triana data. We also demonstrate the value of deep-space observatories for acquiring important

data not available in other ways. A few key points emphasizing the unique features of the spacecraft's L-1 view of the Earth will be presented here.

## 1.2 Science Payload and Retrieved Quantities

The scientific payload is composed of the following instruments:

**Scripps-EPIC**, a 10-channel spectroradiometer (ultraviolet, visible, and near infrared) that uses a 30 cm telescope and a state of the art detector array (near infrared, visible, and ultraviolet sensitive 2048 x 2048 CCD) to achieve the required sensitivity and spatial resolution. EPIC will send back Earth-reflected radiances that will be transformed into data products (e.g., ozone; aerosols; cloud fraction, thickness, optical depth, and height; sulfur dioxide; precipitable water vapor; volcanic ash; and UV irradiance) every hour for the entire globe at 8-14 km surface resolution. That is, hourly observations from sunrise to sunset instead of just once per day (as with TOMS, MODIS, SeaWifs, etc.). EPIC will make monthly measurements and images of the lunar surface at all 10 wavelengths (317.5 to 905 nm) as part of its calibration procedure.

**Scripps-NISTAR** is a greatly improved, advanced technology version of the radiometers presently flown to monitor the total solar irradiance and the radiation reflected and emitted by the Earth. It consists of 4 radiometric channels (3 highly accurate and sensitive self-calibrating absolute cavities and 1 photo-diode) that will measure the total UV, visible, and IR radiances (0.2 to 100  $\mu\text{m}$ ) reflected or emitted from the entire sunlit Earth. Location at the L-1 observing position will permit long integration times, since no scanning is required. A radiometric accuracy of 0.1% is expected, a factor of about 10 improvement in accuracy (compared to Earth-orbiting satellites). These will be the only measurements of the entire Earth's reflected and emitted radiation at the retro-reflection angles. As such, NISTAR will fill in important missing data not obtainable by any Earth-orbiting satellite. NISTAR radiances will be used for: *a*) estimating the albedo for the Earth-atmosphere system, *b*) evaluating estimates of the Earth radiation budget (ERB) from other monitoring systems like CERES, *c*) validating the mean radiance fields that can be directly computed from GCMs, *d*) evaluating the theoretical ratios of near-infrared to total reflectance, which are of intrinsic interest to the vegetation, cloud and snow/ice communities, and *e*) attempting to use the thermal infrared as integrative measures of global change.

**GSFC Plasma-Mag** includes three instruments (Faraday cup, magnetometer, and electron spectrometer) that will obtain measurements of solar wind energetics and magnetic field characteristics at high temporal resolution. This is possible because Triana is a fixed orientation spacecraft (not spin stabilized), always having approximately the same position relative to the Earth-Sun line.

### **1.3 Data Dissemination**

All of the data from the Triana instruments will be made available to the science team and to the general scientific community within hours after reception at the Triana Science Operations Center (TSOC). Archive of the EPIC and NISTAR data will be managed at the Langley Distributed Active Archive Center. Plasma-Mag solar weather data will be available within minutes from acquisition, and provided to the National Oceanic and Atmospheric Administration (NOAA) for use in generating space weather forecasts and advisories.

## **2. Science Objectives in Brief**

### **2.1 Earth's Atmosphere and Surface with EPIC**

For the first time, it will be possible to determine the daily cycles in total ozone, aerosols, and column water vapor at high temporal and spatial resolution. Ten global spectral images of the sunlit side of the Earth will be acquired within 2 minutes with a spatial resolution of 8 km at nadir to 14 km near the Earth's limb.

Ozone anomalies arising from a variety of sources can be tracked with much improved accuracy and related to their meteorological environment. This new knowledge should greatly enhance our basic understanding of ozone processing in the atmosphere and permit more accurate modeling and prediction of ozone variations. The ozone data, in combination with data-assimilation modeling, will also be used to study wave motions, including gravity waves, in the stratosphere much better than previously possible. Other dynamical processes such as the polar vortex structure, near-tropopause circulations, and jet stream winds can be observed. Arctic ozone depletion events can also be detected to assess their ecological threats through enhanced UV radiation. The Triana ozone, cloud, and aerosol data can be used to compute surface UV irradiance each hour so that exposures and health risks can be more accurately determined.

Aerosols will be monitored hourly during the day using combinations of UV and visible wavelengths. The new combination of wavelengths allows determination of optical depth, single scattering albedo, and particle size. Previous use of visible wavelengths for aerosols has been limited to water or forest backgrounds. This new information, provided at high spatial and temporal resolution, will be extremely useful for understanding and modeling the processes that disperse and deplete aerosols, allowing for better assessment and prediction of their chemical, cloud, and radiative impacts. Detection of aerosols in the Arctic Basin, where anthropogenic haze (Arctic Haze) is a significant factor, permits a more accurate determination of the aerosol impact in this extremely sensitive part of the world. The ability to detect aerosols each hour at high spatial resolution will be exploited to provide timely warnings of volcanic ash events and visibility anomalies (smoke and dust plumes) to the air transportation industry (through the FAA), the US Park Service, and the EPA.

EPIC data will also be used to develop valuable new information about cloud, water vapor, and surface properties. Since LEO/GEO satellites are being used to develop comprehensive climatologies of cloud properties at high spatial and temporal resolution, the unique viewing geometry of EPIC can be exploited in conjunction with these other satellites to determine cloud phase and particle shape. Cloud particle habit (shape) is an assumed parameter in current retrieval methods and in mesoscale models and GCMs. Retrieval of this parameter on a global basis will reduce the uncertainties in cloud and radiation modeling as well as in the retrievals of cloud particle size and ice water path. The atmospheric column water vapor will also be derived from reflected measurements over all surfaces on an hourly basis that will complement similar estimates from infrared retrievals of upper tropospheric water vapor column. The near retro-reflection geometry of the EPIC view can also be used to determine anisotropic reflectance properties of various types of vegetation and to improve characterization of canopy structure and plant condition. Diurnal variations of surface spectral albedo will also be derived to provide more accurate models for radiation calculations in GCMs and other atmospheric models.

Triana is a valuable platform for half of a multi-angle remote sensing program because its EPIC images can be collocated with those from any other satellite with close temporal and spatial tolerances. Although only one multi-angle application has been noted, it is expected that the ease of matching EPIC and other satellite data will be an extremely valuable resource for remote sensing and, ultimately, climate modeling,

especially in the area of validation. Conversely, other satellite and ground-based measurements taken at sparse temporal or spatial resolution will serve to verify Triana's hourly retrievals.

Triana's use of the "far side" of the Moon as a calibration reference can also help to assess the calibration of other satellite sensors through matching of co-angled collocated pixels. It is expected that the data will be used to characterize the spectral response of the lunar surface.

The global, high-resolution monitoring of the Earth with EPIC's unique spectral complement will also be valuable for scientific field missions. Phenomena such as aerosol plumes that were only detectable with once-per-day satellite observations can be compared in the field each hour. Mission guidance can be provided for aircraft observations of aerosol plumes or ozone changes. Thus, large-scale context can be characterized more accurately and more information can be provided to mission planners.

## **2.2 Earth's Radiation and Climate with NISTAR**

The thermal infrared radiances measured by NISTAR will provide broadband observations that can serve as a global index of the Earth's climate. The data can be interpreted in terms of the effective emitting temperature of the planet and thus, NISTAR can act as a kind of global thermometer. The observed seasonal and interannual variability could be compared with simulated signals from climate models to assess the significance of any observed short or long-term fluctuations.

When combined with the EPIC imagery and retrievals of cloud properties, the NISTAR shortwave radiances will produce estimates of the global albedo. The derived albedo values, or the original radiance data, can serve to evaluate the radiation calculations in GCMs. The NISTAR shortwave and longwave radiances will also be used to estimate errors in the albedos and longwave fluxes derived from interpolations of sparsely sampled LEO data, the more conventional technique for measuring the Earth radiation balance.

The NISTAR spectral complement will also provide new data to confirm or negate previous estimates of the ratio of near-infrared (NIR) to visible (VIS) albedos. The NIR/VIS ratios have been used extensively to quantify differences between

measured and modeled cloud radiative properties. It will provide a globally integrated test of the episodic but highly time- and space-localized findings of discrepant NIR/VIS cloud albedo ratios (Stephens and Tsay, 1990; Francis et al., 1997; Valero et al., 1997, 1999).

Because the near-infrared channel is sensitive to vegetation and snow/ice cover in addition to clouds, the NIR/VIS ratio is an attractively simple and fundamental analysis tool for studying global change, and Triana is the perfect vantage point to begin using that tool. (No current or planned LEO or GEO Earth radiation budget satellites have a broadband near-infrared channel, although CERES is apparently planning to add one in the post-2003 timeframe, which should serve as a nice complement to that on Triana.)

A modeling infrastructure will be developed based upon existing efforts at NCAR, participating NASA laboratories, and other institutions. This modeling infrastructure will be used to simulate the NISTAR signals and EPIC spectral imagery. Because of Triana's simple viewing geometry and relatively simple data processing requirements compared to LEO satellites, scientists and students would be able to study a wide variety of phenomena without many of the complexities usually associated with remote sensing. Because of the lunar calibration for EPIC and absolute calibration for NISTAR, the scientific community would be able to focus on geophysical applications of a stable, high-accurate data set. This could have important repercussions both for remote sensing and climate.

### **2.3 Solar Wind and Space Weather with Plasma-Mag**

The Plasma-Mag investigation will contribute to both the source and structure of the slow solar wind and the heating of the corona. The mechanisms for heating the solar corona to temperatures that are much hotter than the photosphere are not well understood. Waves in the solar wind almost certainly undergo a turbulent cascade to heat the wind at small scales, but our current descriptions of this are mostly phenomenological. More generally, the coupling between magnetic and electric fluctuations and particle distribution functions is a fundamental plasma interaction, important in a wide variety of contexts, but difficult to study directly. The improved time resolution of Triana/Plasma-Mag provides an opportunity to determine the mechanism by which small-scale fluctuations dissipate in plasmas. A time resolution of less than 1s will provide

information to determine how the plasma responds to the simultaneously measured magnetic fields.

Triana would also provide a monitor of the solar wind in addition to any other spacecraft that may still be available at the time of its launch. This would allow the detailed study of the non-radial correlation with solar wind fluctuations. This study was begun with earlier spacecraft such as the Explorers, IMP, and ISEE, but new opportunities would now be available. For example, if WIND or a STEREO spacecraft were measuring the solar wind at a variety of positions away from L-1, this would provide correlation at multiple baselines. These measurements would help to determine the symmetry of the fluctuations in the wind that in turn determine the way in which energetic particles propagate in the heliosphere. This basic understanding is also central to determining how, for example, solar events affect the Earth and its near-space environment, and thus is important for determining the effects of solar activity on spacecraft and manned space flights.

The Plasma-Mag instruments will measure the magnetic field and the velocity distribution functions of the electron, proton, and alpha components of the solar wind with higher time resolution than existing spacecraft.

The three Plasma-Mag instruments (Faraday cup, magnetometer, and electron spectrometer) will obtain 3-dimensional measurements of the velocity distribution functions of protons, helium ions, and electrons, and the interplanetary magnetic field. The data can be collected with high temporal resolution because Triana is a fixed orientation spacecraft that permits the solar wind ions and electrons to strike the Faraday cup continuously. The data collected by Plasma-Mag will provide early warning of solar events that may cause damage to power generation, communications, and other satellites. Together, the Plasma-Mag suite of instruments will provide a 1-hour warning to the appropriate agencies that safeguard electrical equipment on Earth and satellites in Earth orbit. Present plans include routinely providing the data to NOAA with typically only a 5-minute data processing delay from detection of an event at the Triana spacecraft position to the time that it is delivered. Monitoring of the solar weather has become a mandatory function of government due to the growth of civilian and military satellite communications. Plasma-Mag will add to, or replace, the first generation space-weather monitors, such as WIND, IMP-8, and ACE.

### 3. Scientific Advantages of L-1

#### 3.1 Orbit Description

The Triana mission is scheduled for launch on the space shuttle in 2001. After separation from the shuttle, the Triana spacecraft is expected to take about 3 months to travel 1.5 million kilometers from Earth to reach the vicinity of the L-1 orbit position, and another 3 months to enter its Lissajous orbit (Figure 1).

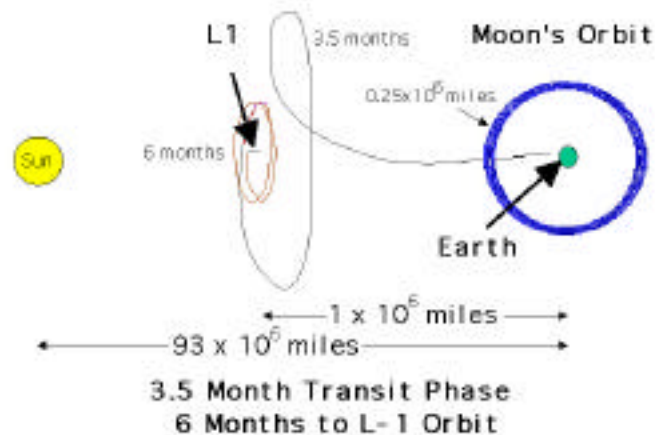


**Figure 1** The injection path for Triana showing the distances and time to reach the L-1 orbit position.

The details of the spacecraft orbit and its position relative to the Earth and the Moon are given in Figure 2. The key point of this diagram is to illustrate the manner in which Triana's instruments will be able to view the sunlit Earth. For the particular Lissajous injection planned for Triana, we will have a view of the entire Northern Hemisphere polar region from about April through August.

#### 3.2 Scientific Significance of Triana's Time and Space Domain

Because of its position in deep space, Triana will look at the Earth in a fundamentally different way that will offer unique data for Earth studies. Its deep space location will secure scientifically important information not presently accessible; most points on the sunlit side of the surface and atmosphere will be viewed simultaneously from sunrise to sunset with high temporal and spatial resolutions. Such a continuous global view and related retrievals will undoubtedly catalyze major advances in our understanding of the climate system. For example, none of the past major satellite

experiments such as Nimbus-7, Earth Radiation Budget experiment, UARS, or the upcoming EOS-Terra provide a complete dayside synoptic (simultaneous data from the entire globe) view. These orbiting satellites sample the Earth in strips about 2000 to 3000 km wide once every few hours. It is to obtain this synoptic view that meteorological centers worldwide launch about 4000 weather sondes twice daily. Why is this synoptic view so important? For example, this is the only reliable way we can infer how the fast atmospheric dynamics, such as tropical meso-scale convective systems, hurricanes, and mid-latitude storm tracks affect the regional ozone, aerosol, and cloud distributions on the planet. Another potential example is that the continuous view of the dayside of the planet will accelerate and maximize the scientific insights we get from our field observations (elaborated later). Deep space observatories, when associated with other satellite, airborne, and surface observational platforms, will enhance our ability to acquire the data needed to test our understanding of the climate system and to advance the Earth sciences.

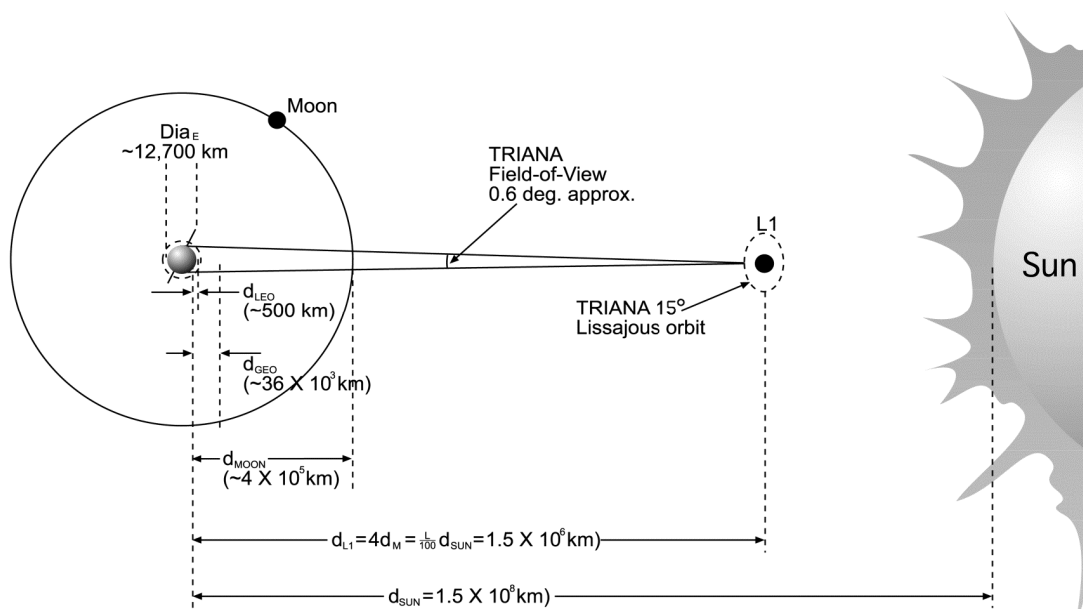


**Figure 2** A summary of major orbital parameters and comparisons with the distances of conventional low Earth orbit satellites  $d_{LEO}$  and geostationary satellites  $d_{GEO}$ . The diagram shows the Moon in approximately the position it will be viewed for Triana calibration purposes, and with the Earth in a solstice configuration allowing a complete view of a polar region.

To illustrate the new perspective that Triana may contribute in terms of scientific information, a brief comparison with geosynchronous and low Earth orbit satellite platforms is in order.

The one satellite platform that can duplicate part of Triana's global view is the GEO satellite. Current weather satellites produce a global view that excludes all areas poleward of  $72^\circ$  every 3 hours. Complete longitudinal coverage could be achieved using 5 of the current GEO satellites. This stitched view introduces discontinuities in the viewing and illumination conditions as well as discontinuities in time and spatial resolution at the boundaries between each GEO satellite. A major source of uncertainties related to the use of GEO satellites is the lack of on-board calibration of their spectral instruments. This problem is exacerbated when one attempts to use multiple GEO satellites to produce a global view, since the calibration problem becomes one of cross-calibration of multiple, different instruments in five different satellites. In addition, the current group of GEO satellites and Triana have different science objectives which require different instrumentation.

Figure 3 depicts the view afforded by five of the current GEO satellites. They would cover about 96% of the planet when "stitched" together, leaving out the polar regions. However, the 96% figure, while true for communication purposes, is misleading when it comes to the collection of scientific data. Because of the curvature of the Earth, everything beyond about  $70^\circ$  satellite viewing zenith angle, or about 6500 km from the sub-satellite point, is too distorted to be useful for scientific analysis without extensive manipulation. Even at  $70^\circ$ , the data are frequently of questionable value because of the viewing perspective. For rigorous scientific utilization, only data up to about  $50\text{-}60^\circ$  is commonly used. See, for example, the web site [[www.iitap.iastate.edu/gcp/satellite/./satellite\\_lecture.html](http://www.iitap.iastate.edu/gcp/satellite/./satellite_lecture.html)].

Useful angle coverage problems will also affect Triana but, since Triana will see points on the surface and atmosphere from sunrise to sunset, this effect will be much reduced in the longitudinal direction as the Earth rotates. The Triana algorithms have been developed to work up to about  $80^\circ$  in either solar zenith angle or satellite view angle, giving a view to within 20 minutes of sunrise or sunset. Unlike GEO satellites, for Triana the two angles are approximately equal, which permits viewing closer to the poles. For example, when Triana is in the ecliptic plane, a point at  $70^\circ$  latitude will be viewed at a VZA of  $70^\circ$  at local noon, whereas it would be almost at the tangential point for a GEO satellite all of the time. Additionally, the combination of the Lissajous orbit of Triana around L-1 and the seasonal change in relative Earth orientation, will enable the periodic view of the higher latitudes including full view of the polar regions (see Figures 5 and 6) for periods close to the summer solstice in each hemisphere. While Triana will see to

within about 20 minutes of sunrise or sunset, GEO satellites of course obtain a better view of the sunrise and sunset terminators.

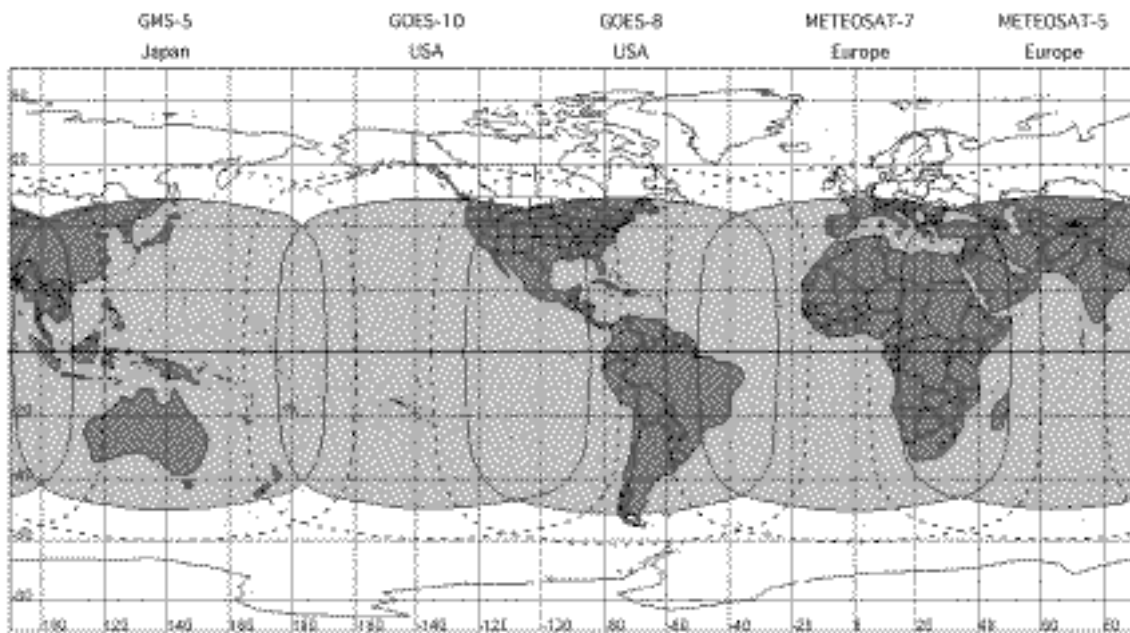


**Figure 3** Shaded regions show a GEO satellite view within 50° and dashed lines correspond to 60°.

Most GEO satellites carry spectral imagers that are unique to the particular satellite. While all of them may have some channels in common, there are usually distinct differences in the specific filter functions even for the common channels. There is only one channel (visible) in the solar spectrum that is common to all of the satellites. For example, the GOES-I series of satellites has a visible ( $0.65 \mu\text{m}$ ) channel but its filter function is slightly different than the previous series of GOES instruments and differs markedly from the broad Meteosat visible channel that extends to  $1.1 \mu\text{m}$ . Although the next generation of Meteosats (MSG) will carry a narrowband visible channel centered at  $0.65 \mu\text{m}$ , both the new and older Meteosats will operate simultaneously. While these imagers can be cross-calibrated to some extent (e.g., Nguyen et al., 1999), spectral differences will remain between them, especially for the Meteosat visible channel. The one common visible channel can be used to produce a discontinuous, near-global, black and white view of the Earth. Triana views all areas from continuously changing viewing and illumination conditions with a single set of instruments including broadband radiances in four channels covering the range from  $0.2$  to  $100 \mu\text{m}$  and images in the ultraviolet, red, green, blue, and two near-infrared channels.

Each GEO series has a different spatial resolution. GOES-7, GOES-8, GMS, MSG, and Meteosat have nominal resolutions of 8, 4, 5, 3, and 10 km, respectively for their infrared channels and 1, 1, 1.25, 1, and 2.5 km for their visible channels. Each GEO has its own imaging schedule such that full-disc views are only available from all satellites only once every 3 hours. Meteosat starts scanning from the south and ends at the northern edge of the Earth. The other satellites begin at the north and scan to the south taking 15-18 minutes to complete a single multispectral image. Each hour, Triana images the entire Earth in 10 channels within 2 minutes with a single resolution that is dependent on the position of the pixel in the array. It provides a three-channel view of the Earth every 15 minutes. At the Earth surface, the spatial resolution varies gradually and continuously.

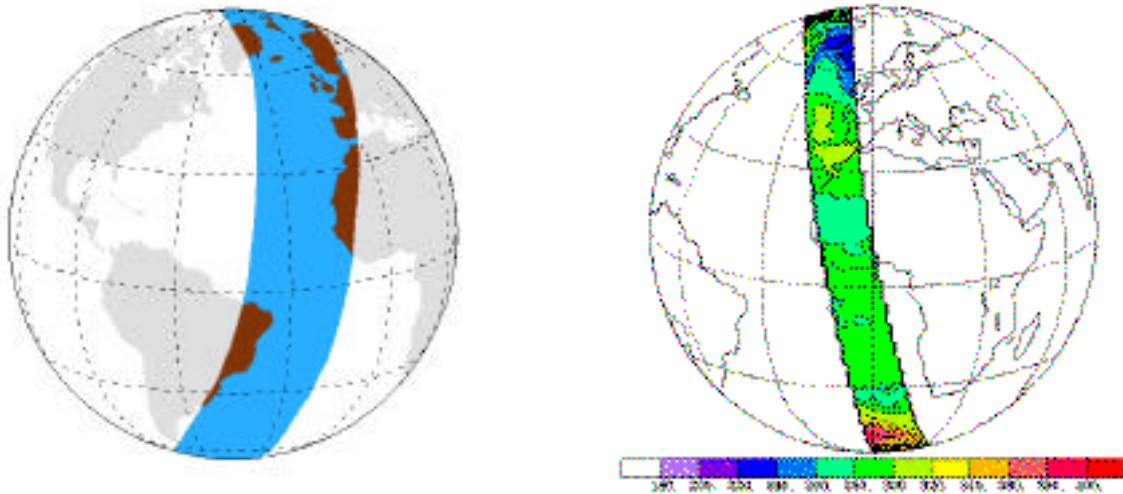


**Figure 4** On the left a single track of the AVHRR satellite, covered in ~50 minutes, is shown. On the right a track from the TOMS covered in ~45 minutes is shown. All points are seen near noon only.

LEO satellites carry some of the same channels as Triana at different spatial resolutions but with much less geographic coverage. Figure 4 depicts a single track of the NOAA 14 (AVHRR) satellite that includes the AVHRR with 645 and 870 nm channels. It takes over 50 minutes to cover the ground (atmosphere) track shown. A similar ground track is produced by the Nimbus-7 that carried a TOMS for ozone measurement at an average resolution of 80 km. While one can merge images of the whole planet from LEO spectral images, these images lack the scientific value provided by the combination of simultaneous global view, high time resolution and sunrise to sunset continuous coverage.

Triana will require approximately 30 seconds to acquire a global ozone map of the entire sunlit half of the Earth (see Figure 5) and 15 minutes to transmit it to the surface (all spectral images are acquired within 2 minutes but the data cannot be transmitted at the same rate).

Polar regions will be best observed by Triana near the summer solstice. However, proper phasing of Triana's orbit around L-1 with the seasonal changes in solar illumination may be used to improve the observation of polar regions during periods of interest, for example spring, as shown in Figure 5 for the southern hemisphere.

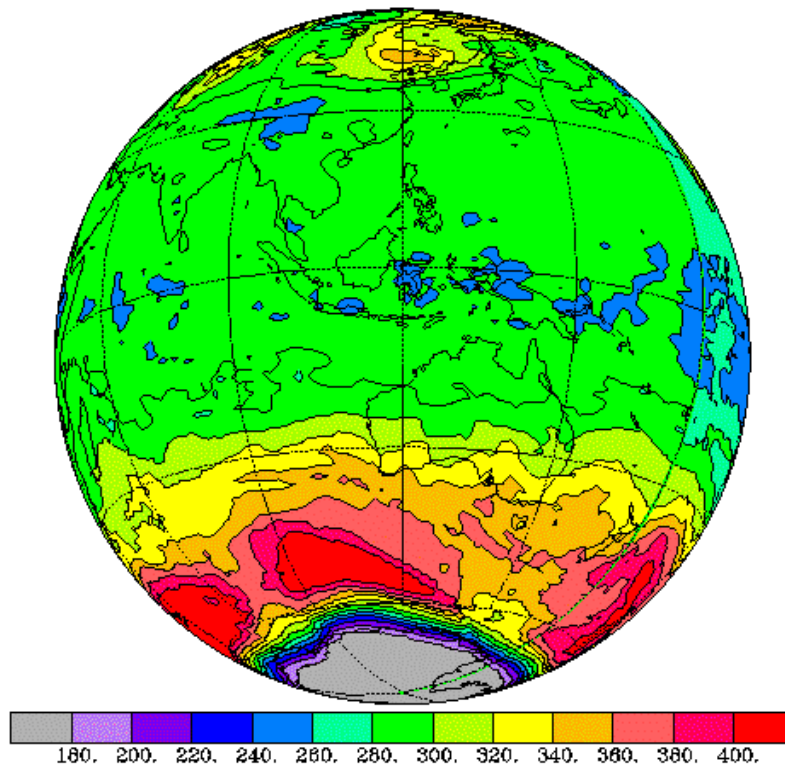


**Figure 5** TOMS data was used to simulate the nearly instantaneous global ozone map (in Dobson units) as will be seen from Triana during the southern hemisphere spring. Triana's position on the Lissajous orbit has been optimized for seeing southern polar regions. Actual Triana views will have higher spatial and time resolutions and will not be limited to near local noon. A strong gradient of column ozone is seen at the edge of the polar vortex. The variations in column ozone around the vortex are associated with planetary waves as discussed later.

Another example of the nearly instantaneous view of the Earth and Moon is shown in Figure 6. While this is a view of the Earth as seen in visible light, the 10-

channel EPIC spectroradiometer will see a much more complex set of scenes that can yield maps of ozone (Figure 5), aerosols, cloud optical thickness, sulfur dioxide, precipitable water vapor, and volcanic ash.

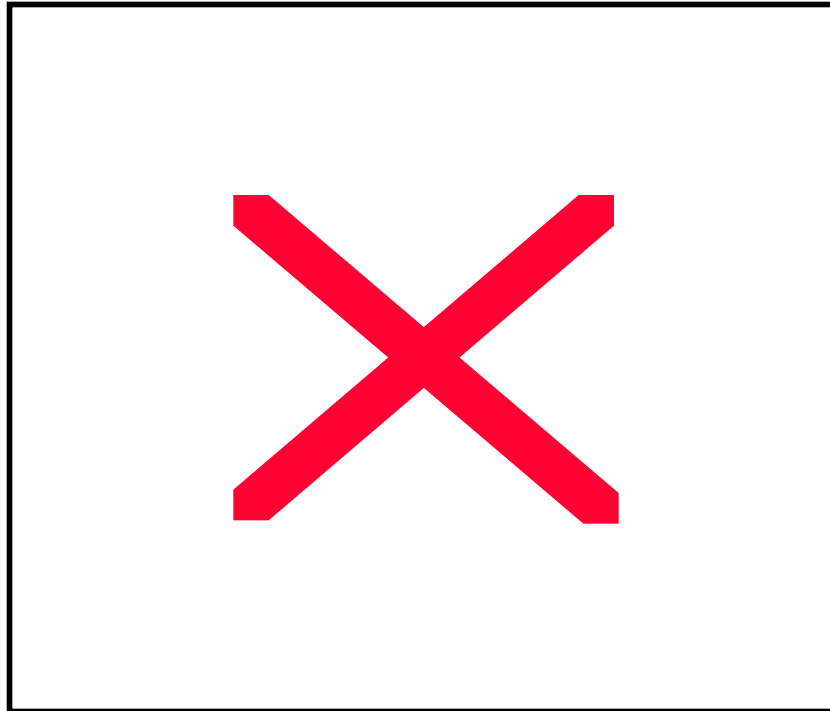


**Figure 6** Simulated nearly instantaneous Triana view of clouds constructed from actual cloud observations seen by the Galileo spacecraft near L-1. The Moon has been inserted from observations of the sunlit side using Clementine data. The Moon view will be used for in-flight calibration of the EPIC spectral channels.

The novel contributions of Triana in the domain of space-time resolution are illustrated for the case of ozone in Figure 7, where the spatial and temporal resolutions of TOMS are plotted together with those corresponding to Triana. TOMS mean spatial resolution of ~ 80 km and temporal resolution of 24 hours are compared to Triana's corresponding 8-14 km and 15 minutes (for ozone retrievals). It should be noted here that Triana incorporates the mesoscale at high time resolution. This is particularly important now that most major weather forecasting centers are already preparing the assimilation of such tracers as ozone in their operational analysis systems.

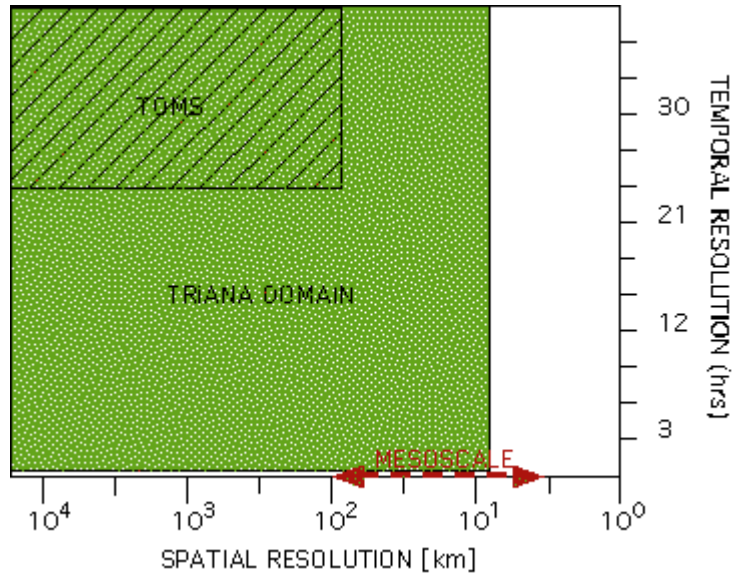


**Figure 7** The spatial and temporal resolutions of TOMS (shaded) are compared to those of Triana (green).

As discussed in some of the following sections, multi-angle views of a particular scene will provide valuable information for climate and vegetation monitoring. By combining Triana radiances and similar data from other satellites taken at different angles, it will be possible to derive new parameters and perform additional studies that are not possible from either platform alone.

### 3.3 Advantages for Field Observations and Process Studies

Field experiments that employ aircraft, ships, and surface stations are an important and integral part of the overall strategy to improve our understanding of weather, climate, and chemistry. But, to extend such field observations to the longer time scales and larger space scales relevant for climate studies, we have to integrate these with satellite observations. ***This integration process requires flying the aircraft under the overhead satellites.*** Orbiting satellites offer limited opportunities to do so. Triana will help to fill this need every day from sunrise to sunset by providing continuous retrievals of aerosols, water vapor, ozone, plus the view in the global context of the processes under study. All of these retrievals will be available using single, in-flight calibrated, stable instrumentation. Examples of important possible synergism are the EOS, the ARM CART sites, the NSF sponsored ACE and INDOEX, the NASA FIRE and FIRE.ACE, and other present and future field experiments that require satellite retrievals.

Triana will be just the first step in an effort to incorporate deep space observatories of the Earth to acquire data, which although similar in spectral composition to that retrieved from existing satellites, will provide a space-time coverage not presently available. Future deep space Earth observatories, for example at L-2, would allow observations of the “night-side” of the planet and complement the “sunlit” view. As the first step in an emerging multi-perspective (LEO, GEO, and L-1) approach to understanding and observing all elements of the Earth system, the Triana vantage point offers several opportunities for examining aspects of the Earth not presently accessible. Indeed, armed with remote sensing instrumentation, Triana could provide never before available observations of dynamic aspects of atmospheric aerosols and clouds, ozone, regional ecological responses on short time scales, and other variabilities. There are many scientific advantages of the synoptic, constant-illumination, Triana vantage point that could be exploited to add further scientific and human value (education included) to deep space observatories. We are convinced that Triana will be a stepping stone to a much more robust future distributed Earth Sensing System.

#### 4. Instrument Descriptions

The Triana spacecraft carries 3 basic instruments: EPIC (Earth Polychromatic Imaging Camera, a 10-wavelength spectroradiometer), NISTAR (NIST Active Radiometer, a 3-channel cavity radiometer for sunlit-Earth energy emission), and Plasma-Mag (a Faraday cup and magnetometer for space weather observations). A drawing of the spacecraft and instruments is shown in Figure 8.

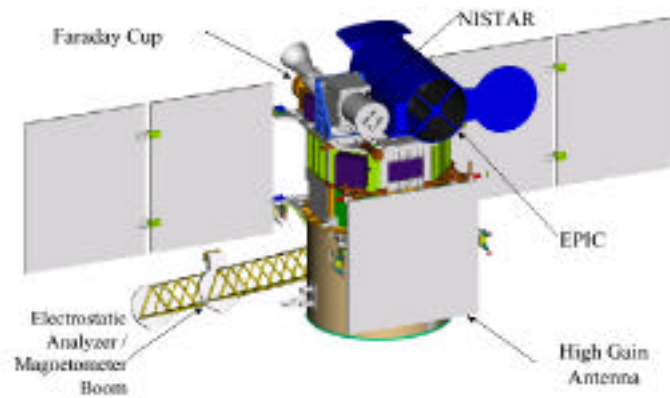


**Figure 8** A drawing of the Triana spacecraft and instruments.

In addition to the instruments, Figure 8 shows the extended solar panels, high gain antenna (flat gray square), and the magnetometer boom. EPIC is shown with its “open-once” cover in the open position. NISTAR is mounted to its right showing the 3 cavity radiometer openings and reference diode. The solar wind analyzer (Faraday cup) is shown mounted on the sun-side of the spacecraft.

#### 4.1 EPIC

The 10-channel EPIC spectroradiometer is shown in Figure 9 and described in some detail in Appendix A. It spans the wavelength range from the ultraviolet to the near infrared (317.5, 325, 340, 388, 393.5, 443, 551, 645, 870, and 905 nm, see Table A-1). To view the Earth, EPIC contains a state of the art 2048 x 2048 CCD detector that has been modified to be very sensitive over the entire wavelength range. Because of the 12-inch telescope optics, the 4 million CCD elements map the Earth with a resolution of about 8 km. The real resolution is somewhat less, about 10 km at the center of the Earth and larger near the edges. The decrease in resolution from 8 to 10 km arises primarily from the “point-spread function” of the optics. A summary comparison of EPIC with some other satellite instruments is given in Table 1.

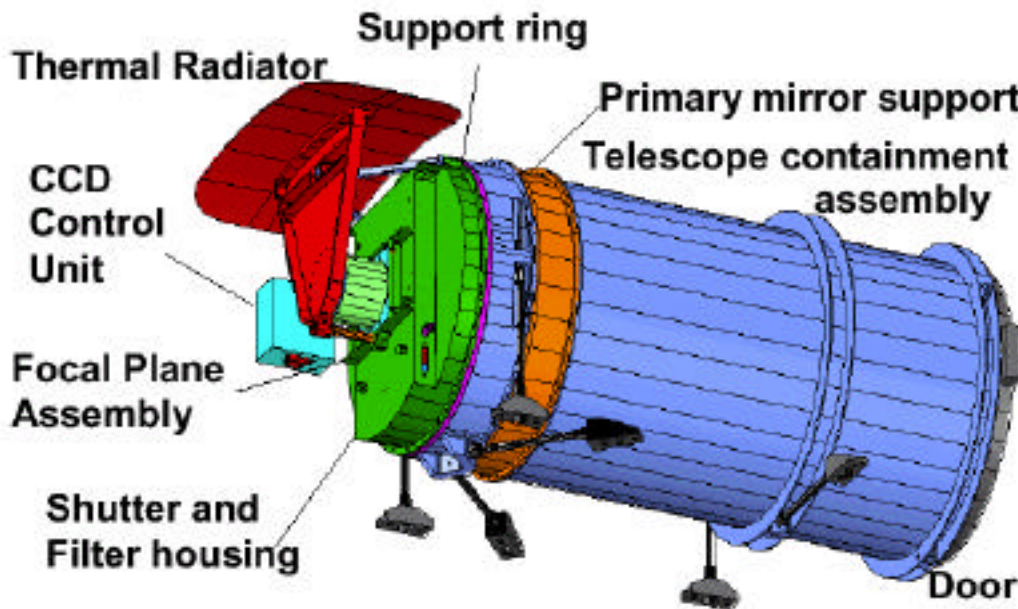


**Figure 9** Scripps-EPIC spectroradiometer telescope assembly (view from below mounting surface) showing the thermal radiator to keep the CCD at  $-40^{\circ}$  C.

**Table 1** Comparison of Triana EPIC at L-1 with LEO/TOMS and GEO/GOES Spacecraft

	<u>Triana at L-1</u>	<u>TOMS at LEO</u>	<u>GOES at GEO</u>
Spatial Coverage	Whole sunlit Earth Every hour	80% of sunlit Earth Once per day (11:30)	1/3 of Earth every 15 min, No Polar View
Spatial Resolution	8-14 km	45 to 90 km	1 km visible; 4 to 8 km IR
Type of Measurement	UV to Near-IR Filter Instrument, 10 Channels, 317 to 905 nm	UV Grating Spectrometer, 6 Channels, 308 to 360 nm	1-Visible; 4- IR
Frequency of Measurement	RGB every 15 minutes, 10 Channels every hour for each of 4,000,000 scenes	6 channels once per day for each of 52,000 Earth scenes	5 channels every 15 minutes; Visible channel > 50,000,000 scenes
Science quantities	Ozone, Sulfur Dioxide (SO <sub>2</sub> ), Aerosols (dust, smoke, and pollution), Cloud Height, UV Radiation at the Ground, Cloud Transmittance and Reflectivity, Cloud Distribution, Cloud Optical Depth, Volcanic ash (hourly aircraft hazard warning) Precipitable Water With auxiliary data: Cloud Phase Cloud Particle Shape, Surface Retro-reflection	Ozone, Sulfur Dioxide (SO <sub>2</sub> ), Aerosols (dust, smoke, and pollution), UV Radiation at the Ground, Cloud Transmittance and Reflectivity Volcanic Ash once per day	Cloud Distribution, Cloud Height, Cloud Particle Size, Cloud Optical Depth, Aerosols over Ocean, Surface Reflectance, Surface Temperature Fire Detection, Storm Tracking
Main Advantage	Whole-Earth coverage from Sunrise to Sunset; First mission to measure hourly changes in ozone, clouds & aerosols over the whole globe Fixed azimuth angle	Highly stable and accurate instrument suitable for trend studies; enables estimates of surface UV radiation Nearly constant solar zenith angle	High spatial and temporal resolution; views day and night Fixed viewing zenith angle
Main Disadvantages	Unproven stability; not known if level of accuracy will be sufficient for ozone trend studies	Low spatial resolution and only 1 measurement per day at each geographic location	Views only 1/3 of Earth with no views of polar regions; 5 platforms are needed to cover globe allowing for overlap; Visible channel accuracy of 3%

## 4.2 NISTAR

The NISTAR radiometer is shown in Figure 10 and described in detail in Appendix B. It is a 4-channel radiometer. Three of those channels are absolute cavities and the fourth is a silicon photodiode radiometer. The instrument views the sunlit Earth continuously to obtain Earth radiation data from 0.2 to 100  $\mu\text{m}$  in 4 wavelength bands. An accuracy of 0.1% is expected. The accuracy goal is based on the high sensitivity of the instrument and on the ability to integrate for long times (minutes) due to the deep space location. The spectral channels are:

1. A visible to far infrared (0.2 to 100  $\mu\text{m}$ ) channel to measure total radiant power in the UV, visible, and infrared wavelengths.
2. A solar (0.2 to 4  $\mu\text{m}$ ) channel to measure reflected solar radiance in the UV, visible and near infrared wavelengths.
3. A near infrared (0.7 to 4  $\mu\text{m}$ ) channel to measure reflected IR solar radiance.
4. A photodiode (0.3 to 1  $\mu\text{m}$ ) channel for calibration reference for the spectroradiometer.

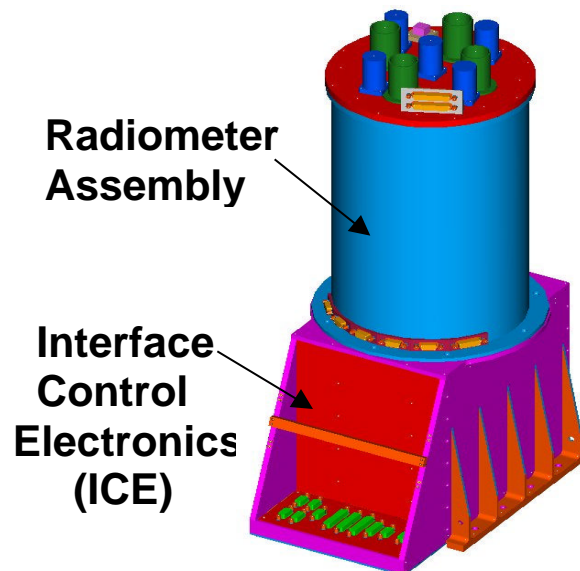


**Figure 10** View of the Scripps-NISTAR multi-channel absolute radiometer.

## 4.3 Relationship Between NISTAR and EPIC Data

The interpretation of the NISTAR data in terms of the global albedo needed for energy balance calculations is complicated by the large variation in albedo over the Earth's surface-atmosphere system, changes in albedo with solar zenith angle, and

anisotropy of the reflected solar radiation (Smith, 1999). In addition to these general effects, there is the diurnal and daily variation in the amount of cloud cover and its reflectivity. An analysis of the problem shows that the effects can be summarized in an effective phase function for the various scene types typical of the Earth. Information concerning the distribution of albedo (clouds) and scene-dependent anisotropy of the reflected radiation can be provided by EPIC.

At least 3 EPIC channels will be required to compute the broadband albedo of Earth scenes. Data from a broadband instrument (e.g., CERES onboard Terra) will be used initially to calibrate and validate the broadband albedo data from EPIC. Since EPIC and NISTAR always have the same Earth viewpoint, EPIC data will then be used to account for the anisotropy of reflected solar radiation in the computation of global albedo from NISTAR measurements. Conversely, the NISTAR active cavity radiometer can provide ongoing calibration maintenance for albedo maps from the EPIC spectroradiometer.

#### **4.4 Plasma-Mag**

The Plasma-Mag package consists of three parts: 1) a Faraday cup to measure the 3-D distribution function of proton and alpha components of the solar wind with a time resolution (repetition rate) of 90 milliseconds, 2) a “tophat” analyzer to give 3-D electron velocity distribution functions in 800 ms (480 points), and 3) a flux-gate magnetometer to make a vector measurement in 30 to 40 milliseconds. A much-improved time resolution is possible because Triana is a 3-axis stabilized spacecraft permitting near-continuous measurements. Previous solar-wind measurements from the spin-stabilized WIND spacecraft could only be made when the Faraday cup pointed towards the Sun.

The Faraday cup is particularly suited for precise solar-wind measurements on a stabilized spacecraft because of its large field of view ( $\pm 60$  degrees). The use of multiple collectors allows the full range of the solar wind deflections (approx.  $\pm 15$  degrees in all directions) to be detected, while still allowing a full 3-D velocity-distribution function to be accommodated. The whole distribution function remains in the field of view, so that more accurate density measurements can be made, especially at high densities.

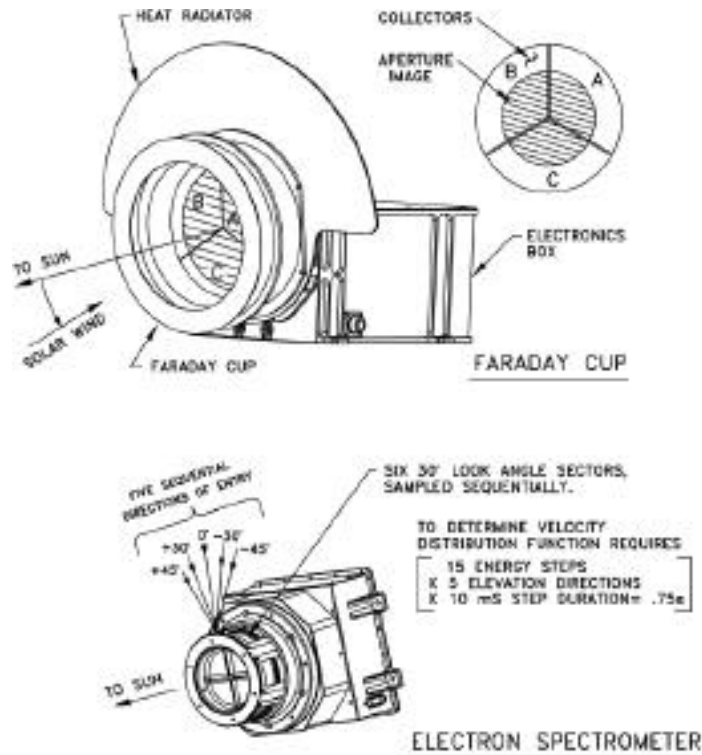


**Figure 11** Schematic drawing of the Faraday cup electron spectrometer showing the ability to analyze the particle distribution function in terms of energy level and angle of velocity vector.

The tophat electrostatic analyzer will make measurements of the electron distribution function between 3 eV and 2 keV in a time as short as 800 milliseconds. The 3D measurement will be accomplished by electronically simulating the data sampling of an electron spectrometer on a spinning spacecraft. The instrument has a set of anodes distributed uniformly in azimuth, each with a field of view  $50^\circ \times 7^\circ$  in azimuth and elevation. The anode distribution around the circumference of the symmetry plane ( $0^\circ$  elevation) provides azimuthal coverage over  $2\pi$ . The coverage in elevation is between  $+60^\circ$  and  $-60^\circ$  above and below the plane of the anodes is accomplished by varying the potential of external deflection plates.

In addition to studies of the Sun and solar wind, the data also are used to provide early warning of solar events that might cause damage to power generation, communications, and other satellites. Together, the Plasma-Mag suite of instruments will provide a 1-hour warning to the appropriate agencies that safeguard electrical equipment on Earth and satellites in Earth orbit. Present plans include routinely giving the data to NOAA with only a 5-minute data processing delay from detection of an event at the

Triana spacecraft position and reception at the ground station to the time that it is delivered.

Plasma-Mag contains a triaxial-fluxgate magnetometer that will investigate solar-wind magnetic fields with a sensitivity level of better than 0.1 nanoTesla. The Plasma-Mag instrument is an evolution of a long line of magnetometers developed at the Goddard Space Flight Center. The present design has been optimized for small size, low power, simplicity, and a very large dynamic range. Using the latest technology in sigma-delta converters it achieves a dynamic range of almost 8 orders of magnitude in field measurement capability, simplifying its implementation aboard the Triana spacecraft. The commercial-technology sensor is small and light (65 gram) and will be mounted at the end of an extensible boom remote from the spacecraft body. Although as many as 100 samples of the vector magnetic-field measurement can be acquired per second, only a fraction of these will be formatted and transmitted to Earth, the baseline being 1 sample per second.

Table 2 summarizes the comparison between Triana and other NASA solar missions to L-1.

#### **4.5 Data Characterization**

The EPIC Level-2 data will consist of hourly frames of 4 million calibrated Earth-located radiances along with ancillary data related to the Triana orbit and Earth geometry. These ancillary data will be sufficient to derive the main science products and any additional science quantities related to the Earth's surface and atmosphere as well as the lunar surface. The main science products will also be available for each of the 4 million Earth radiance locations. The radiance data obtained every 15 minutes from the 443, 551, and 645 nm visible channels will also be available for science and Earth images. EPIC Level-3 data will consist of the main derived science products on a fixed latitude by longitude grid at a resolution of at least  $0.5^\circ$  along with false-color images suitable for animation. Each Level 2 main science-product or radiance-channel data will consist of approximately  $4096 \times 4096 \times 12/8 \times 24 = 0.6$  Gbytes per day ( $\sim 0.2$  Terabytes per year per data product or radiance) plus ancillary data that could be of comparable size or larger. The data are expected to be in HDF (or other standard self-documenting format) that could add 10 to 20% overhead in size. Primary data distribution will be through a NASA DAAC and through the Scripps Science Operations Center.

**Table 2** Comparison of NASA Solar Wind Missions to L-1

Triana	SOHO	ACE	WIND	Genesis
Launch in 2001	Launched 1995	Launched 1997	Launched 1994	Launch Jan. 2001
<p><u>Mission:</u> Provides real-time solar wind info. with much better time resolution than WIND or ACE*</p> <p>Covers period of decreasing solar activity.</p>	<p><u>Mission:</u> Study the internal structure of the Sun, its extensive outer atmosphere, and the origin of the solar wind. Does <u>not</u> measure magnetic field, which is essential for space weather and solar wind studies.</p>	<p><u>Mission:</u> Determine and compare the isotopic and elemental composition of several distinct samples of matter, including the solar corona, the interplanetary medium, the local interstellar medium, and Galactic matter.</p> <p>Provides real-time space weather info.**</p>	<p><u>Mission:</u> Use a changing orbit to provide complete plasma, energetic particle, and magnetic field input for magnetospheric and ionospheric studies. (No longer at L-1; operating at other orbits closer to Earth.)</p>	<p><u>Mission:</u> Collect solar wind samples at L-1 and return to Earth.</p>
Earth-viewing, with solar wind instrument positioned sunward to make continuous measurements	Continuous Sun-viewing	Continuous Sun-viewing	Intermittent Sun-viewing	Sun-viewing

\*Triana assures the continuity of space weather data beyond the design lifetime of ACE.

\*\* For the period that both Triana and ACE are operating, they will operate from opposite positions in the orbit around L-1, enabling comparisons and more detailed study of solar wind structure.

NISTAR data will consist of a total daylight-side Earth-radiance time series from each of the 4 channels along with ancillary data related to the viewing geometry. The one-second time resolution of the data translates as approximately 25 megabytes per day, or 9 Gbytes per year.

Plasma-Mag data will consist of time series for magnetic field, solar wind speed, and plasma energy along with ancillary data related to the spacecraft-Sun geometry. The data size is a few megabytes per day, or about 1 Gbyte per year.

## 5. Science Products

### 5.1 EPIC

Most of the science products (see Table 3) are obtained by combining pairs of radiances measured at different wavelengths to extract information based on their differences. To improve the measurements, the measured Earth radiances are normalized to lunar radiances measured by EPIC on a regular basis. Use of the resulting normalized radiances, I/F, cancels a number of possible instrument errors (e.g., radiometric drift). A similar solar normalization (using a diffuser plate instead of the Moon) is used for TOMS and GOME data processing. Use of the lunar radiances is a complicated problem that is discussed later.

The Triana viewing geometry is different from observations at other angles because of reflections over oceans (sun-glint) and increased effective reflectivity from land surfaces (hot spot phenomenon caused by decreased shadows from plants and rocks when the Sun is behind the observer). For UV wavelengths, the hot-spot increased reflectivity from land is not a problem because of strong Rayleigh scattering in the atmosphere. However, the increased ocean reflection still must be taken into account. For average wind speeds of about 10 km/hour, the ocean albedo increases from about 4% at the edges to about 20% in the center of the sun-glint region (a circle of about 20° of latitude in diameter). As wind speed increases, the albedo decreases from 20% until whitecaps occur. These effects are included in the algorithms through the measured reflectivity and knowledge of the sun-glint region geometry. This technique is currently used in the TOMS data analysis to permit ozone and aerosol amounts to be retrieved throughout the sun-glint region.

In each case, the science quantity is obtained for scenes at a spatial resolution of 8 km x 8 km corresponding to the 2048 x 2048 CCD elements distributed over the image of the sunlit Earth. The expected accuracy is shown in Table 4. Of course, the area projected onto the Earth's surface increases towards the limb. The data reduction algorithms contain routines for geolocation of the measured radiances on a pre-determined latitude by longitude grid.

**Table 3** Spectral channels in the Scripps-EPIC. The spectral resolution corresponds to the sub-satellite point at the Earth’s surface. The 10 wavelengths will be measured once per hour for the entire globe. Spatial resolution corresponds to sub-satellite point. The longest exposure time is 0.1 seconds.

$\lambda$ (nm)	$\Delta\lambda$ (nm) FWHM	Quantity Retrieved	Spatial Resol. (km)
317.5	1	Ozone, SO <sub>2</sub>	8
325	1	Ozone, SO <sub>2</sub>	8
340	3	Aerosols	8
383	3	Aerosols, Clouds	8
393.5	1	Cloud Height	8
443	10	Blue, Aerosols	8
551	10	Green, Aerosols, Ozone	8
645	10	Red, Aerosols, Vegetation, Clouds	8
870	15	Clouds, Vegetation	8
905	30	Precipitable Water	8

**Table 4** Expected Accuracy of Main Data Products

Product	Spatial resolution		Comment
	8km	16km	
Ozone	±3%	±2%	Using 3 bands
Aerosol Optical Depth	±30%	±30%	Without height modeling
Aerosol Optical Depth	±10%	±10%	With height modeling
Cloud height	±40 mb	±20 mb	Raman technique
Cloud height	±15 mb	±15 mb	Water technique
UV Irradiance	±10%	±10%	Except with snow
Precipitable Water	±10%	±10%	
Sulfur Dioxide	±20%	±10%	For volcanic eruptions

### 5.1.1 Ozone

The derivation of the Triana total ozone amounts is based on the TOMS (Total Ozone Mapping Spectrometer) algorithms with adjustments for the Triana view angles. Four of the EPIC UV wavelengths (317.5±0.5, 325±0.5, 340±1.5, and 388±1.5 nm) were chosen to match closely those that were used by the highly successful original Nimbus-7/TOMS instrument (1978 to 1993). The fifth UV wavelength is centered on the solar calcium-K Fraunhofer line at 393.5±0.5 nm. Filling in of the Fraunhofer line as a function of altitude is used for cloud height analysis (see discussion below) and to improve the retrieval of total column ozone.

The amount and distribution of total ozone over the globe is sensitive to the state of the atmosphere with regard to pollution (e.g. man-made chlorine bearing chemicals) and the effects of atmospheric temperature changes. The total amount of ozone contained in a column is obtained from the ratios of measured radiances  $I(317.5)/I(340)$  or  $I(325)/I(340)$ . The reduced sensitivity of 325 nm to ozone absorption compared to 317.5 nm is used to extend the measurements to higher solar zenith angles than is possible with 317.5 nm. At high solar zenith angles, the 317.5 nm solar irradiance does not penetrate all the way to the surface, and so does not detect the total column ozone amount. The radiance at 340 nm is almost unaffected by ozone absorption, and is used as the reference channel to characterize the Rayleigh scattering atmosphere. The 388 nm channel can also be used as a reference channel.

The method of inversion to obtain ozone amounts from the measured radiances is based on precomputed lookup tables derived from radiative transfer solutions. The algorithm includes the effects of clouds derived from a measurement of the increased scene reflectivity (340 or 388 nm) over the normal clear-sky UV surface reflectivity (2 to 8%). Corrections are also made for the presence of aerosols within each scene (dust, smoke, and pollution, see below).

A further measure of ozone can be obtained using the weak absorption in the Chappuis band at 551 nm as discussed in the following paragraphs. An example, shown in Figure 12, of the expected ozone detection capability has been simulated using data from TOMS.

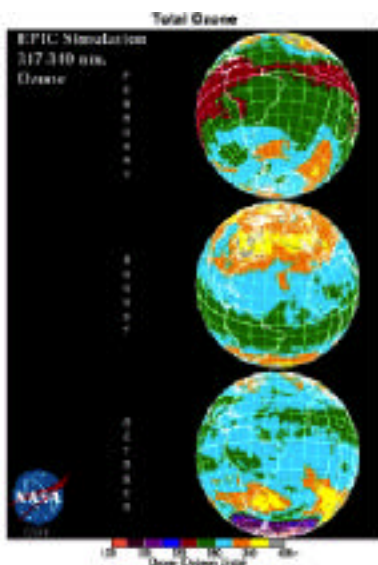


**Figure 12** A simulation of an EPIC view of total ozone amount for 3 different seasons represented by the monthly averages for February, August, and October obtained from TOMS data. The tilt of the Earth as seen from L-1 is shown for the respective months. EPIC will observe the diurnal variation of ozone each day over the entire sunlit globe.

Chappuis-band ozone detection is used to extend the latitude range over which measurements can be accurately made (to within 5%). This will allow EPIC to observe the development of ozone changes in the sunlit portion of the Arctic, particularly during the important spring season (see Figure 13). Depending on the orbit, EPIC will also be able to

observe the springtime development of the Antarctic ozone hole.

For radiation at 317.5 or 325 nm, only a small fraction of the photons back-scattered from the atmosphere come from low altitudes when solar zenith angles are large ( $SZA > 70^\circ$ ). The problem arises from two sources: both the ozone absorption and Rayleigh scattering are roughly proportional to  $e^{-(n+N)/2\cos(SZA)}$  for EPIC observations,

where  $\sigma$  is the ozone absorption coefficient ( $\text{cm}^{-1}$ )  
 $n$  is the column amount of ozone (cm)  
 $\sigma_r$  is the Rayleigh scattering coefficient ( $\text{cm}^{-1}$ )  
 $N$  is the column amount of molecular atmosphere (cm).

The result is that UV wavelengths that are weakly sensitive to ozone absorption cannot be used at high SZA because of intense Rayleigh scattering. The problem is made worse as  $N/\cos(SZA)$  increases because of multiple scattering effects. The Rayleigh scattering problem can be greatly reduced if measurements are made in the visible wavelengths where there is also weak ozone absorption.

The peak Chappuis-band ozone absorption in the visible wavelengths occurs near 605 nm and is negligible for wavelengths shorter than 450 nm and longer than 750 nm. As currently configured, EPIC contains a filter position at  $551 \pm 5$  nm (green) where the Chappuis band ozone absorption is still strong and where the Rayleigh scattering is relatively small. The reference channel could be one of the following existing wavelength channels, 443, 645, or 870 nm. Radiative transfer analysis indicates

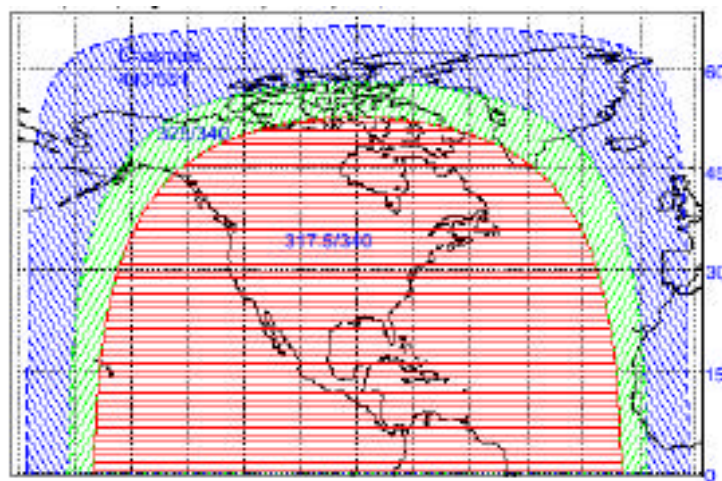


**Figure 13** An illustration of the geographic coverage afforded by the three different ozone sensitive wavelength pairs: 317.5/340, 325/340, and 443/551. The Chappuis band extends the observations to high latitudes and nearer to sunset/sunrise terminator.

that 443±5 nm (blue) is the best choice, since it has almost no ozone absorption (compared to 645 nm) and is much closer to 551 nm than 870 nm. The more sensitive channel at 605 nm was not used so as to include a water-sensitive channel at 905 nm and still have only 10 wavelengths.

As with other calculations, the radiative transfer analysis has been performed with a full spherical geometry calculation (Herman et al., 1996) and with the pseudo-spherical program that has been extensively validated over the past 20 years (Dave, 1965). Both calculations agree up to 80° SZA with the results from the full spherical geometry calculation used between 80° and 90°. The results are contained in a lookup table for  $C(\text{ozone}, \text{SZA})$ .

$$C(\text{ozone}, \text{SZA}) = \frac{I_{443}}{I_{551}}$$

At solar zenith angles near 60°, where total column ozone can be determined by both  $I_{443}/I_{551}$  and  $I_{325}/I_{340}$ , the values will be compared to assess the accuracy of the Chappuis-band analysis. This is needed because the Chappuis-band estimation of ozone is sensitive to the underlying surface reflectivity, which is variable in the blue and green wavelengths. The blue and green surface reflectivities will be estimated at smaller SZA and used at angles greater than or equal to 60°. A possible problem is that the surface reflectivities have an angle dependence that is not known for Triana observing conditions, and can cause an error in calculated ozone amounts. The comparison with the  $I_{325}/I_{340}$  determination of ozone will help determine this angular dependence.

### 5.1.2 Aerosols

Aerosols in the atmosphere arise mainly from dust (e.g., from the Sahara and China), smoke (from biomass burning in South America and Africa), and sulfates (from industrial pollution). Aerosols are detected using the differences between the measured 340 and 388 nm radiances  $I_{340}$  and  $I_{388}$  after removal of the surface and Rayleigh scattering contributions. Surface contributions are removed by using seasonal minimum reflectivity values derived from 14 years of TOMS reflectivity data (Herman and Celarier, 1997). The contribution is quite small, since reflectivity for the surface ranges from 2 to 8% at UV wavelengths.

A direct method for detecting aerosols in the atmosphere consists in using an aerosol index AI. This quantity is much simpler to compute than the optical depth, and does not need aerosol properties (e.g., refractive index and particle size) for its computation.

$$A_I = -100 \text{ Log}_{10} \frac{I_{340}}{I_{388}}_{\text{Measured}} - \text{Log}_{10} \frac{I_{340}}{I_{388}}_{\text{Calculated}}$$

The sign has been selected so that  $AI > 0$  for absorbing aerosols (e.g., dust and smoke) and  $AI < 0$  for non-absorbing aerosols (e.g., sulfates) (Herman et al., 1997; Torres et al., 1998). There are two terms in the equation for AI. The first represents the measured ratio of radiances and contains the effects of Rayleigh scattering, surface reflectance, and aerosols. The second term is calculated for a pure Rayleigh scattering atmosphere, at the same geometry appropriate for the measured radiances, over the measured and climatological surface reflectivity (Herman and Celarier, 1997). AI is a measure of the deviation of  $I_{340}/I_{388}$  from a pure Rayleigh atmosphere.

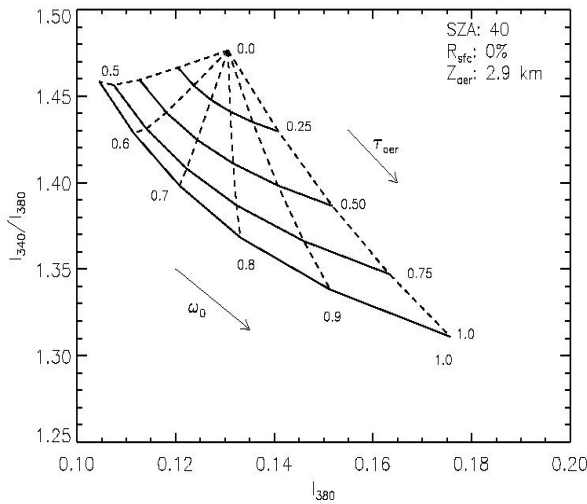


**Figure 14** A graphed example of pre-computed aerosol optical depth and single scattering albedo tables. The numbers labeling the dashed lines are single scattering albedos and those labeling the solid lines are optical depths.

The value of AI is zero for the large scattering particles (~10 microns or larger) in clouds. For sulfate aerosols, the particle size near the accumulation mode is ~ 0.1 microns and produces a contrast effect between  $I_{340}$  and  $I_{388}$  caused by the wavelength dependent Mie scattering. For absorbing aerosols, the  $AI > 0$  effect is produced by interference with the  $\lambda^{-4}$  wavelength dependence of Rayleigh scattering from the atmosphere below the aerosol plume. The interference occurs whether or not the aerosol plume has a wavelength dependent absorption.

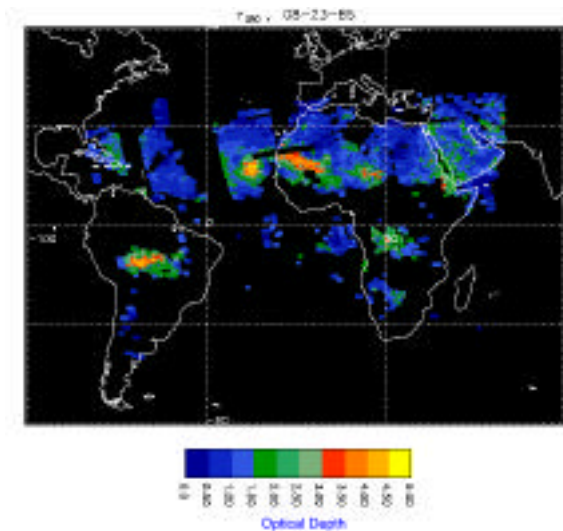


**Figure 15** The optical depth of dust (Arabian Peninsula, Africa, and Atlantic Ocean) and smoke (Equatorial Africa and Brazil) derived from  $I_{340}$  and  $I_{380}$  for the 11:00 am overpass time of TOMS. Note the dust extending to the Caribbean and Florida. The difference for EPIC will be that the longitudinal coordinate will be equivalent to time. In this map, the afternoon fires in Africa would be seen at the same time as morning fires in South America. Smoke is at a minimum in the morning and peaks in the late afternoon.

AI is useful for the basic detection of the presence of aerosols and will be used for the volcanic-ash aircraft warning capability. However, AI combines the effects of optical depth, particle size, single scattering albedo (absorption), and aerosol plume height. As such, it is not as useful as optical depth and single scattering albedo for quantitative calculations of atmospheric effects caused by the presence of aerosols.

The optical depth and single scattering albedo can be obtained using pre-computed tables of radiances as a function of  $\lambda$  and  $\tau$  (Hsu et al., 1999b) if other aerosol parameters are known or assumed (e.g., plume height, particle size, refractive index). The tables are computed with  $I_{340}/I_{388}$  and  $I_{340}$  as independent variables. A sample table is illustrated in Figure 14 and results for the optical depth are shown in Figure 15. For the results to be accurate, the 8 km x 8 km scene must be nearly cloud free. That is, the computed scene reflectivity must be less than about 15%.

Of the unknown parameters, the calculated optical depth is most sensitive to uncertainties in the plume height for absorbing aerosols (see next paragraph). Non-absorbing aerosol retrievals do not require knowledge of the plume height. The refractive index is estimated from the known aerosol type, dust, smoke, or volcanic ash. Estimates for these values are known from samples obtained from the local regions of origin (e.g., Saharan dust). Finally, the calculated values are weakly sensitive to the assumed particle size distribution (assumed to be lognormal) and mean particle radius. The mean particle radius is taken from typical values measured for either dust or smoke.

Use of AI or is very useful for tracking dust plumes based on the wind motions in the 2 to 5 km region of the troposphere. The tracking of aerosol plumes using a data assimilation model or GCM containing known wind fields can be used to determine the aerosol-plume height. This is possible because of wind shears in the lower troposphere causing tracers to follow the observed aerosol plume only if the tracer is at the same altitude as the center of the plume. The hourly measurements from EPIC at 8 km spatial resolution will greatly improve this capability compared to a similar analysis successfully used for TOMS at 100 km resolution and once per day. The accuracy of this method is estimated to be 0.5 km and will reduce the error in optical depth determination from  $\pm 30\%$  to  $\pm 10\%$ . There is a large network of sunphotometers present on the ground (AERONET) from which the optical depth can be directly determined and used to provide validation for EPIC aerosol retrievals (Hsu et al., 1999b).

The more frequent hourly observations afforded by Triana-EPIC will enable the diurnal variation of both dust and smoke plumes to be observed for the first time over wide areas. For example, it is well known from ground-based observations that smoke from large fires is a minimum in the mornings and peaks in the late afternoon. Observing this variation over wide areas is important for the estimation of the radiative forcing of aerosols and their contribution to overall radiative energy balance of the Earth (Hsu et al., 1996).

One of the unique features of UV-radiance detection of aerosols is that they can be detected over both land and water. In the absence of ground-based data to locate aerosol plumes, visible wavelength detection of aerosols, such as done by AVHRR and MODIS, is largely confined to detection over water, or certain highly vegetated areas, where the surface reflectivity is low. For the UV wavelengths, detection of smoke and dust can be carried out over any surface, even highly reflective snow and ice (Hsu et al., 1999c). Detection of non-absorbing sulfate aerosols can be carried out over both land and water since the surface reflectivity is always between 2 and 8% (Herman and Celarier, 1997).

EPIC will be the first Earth observing spacecraft instrument to combine measurements in both UV and visible wavelengths. This will enable additional aerosol properties to be determined. Presently, TOMS can only determine two properties, optical depth and single scattering albedo, and must assume the others. By adding the visible channels, the aerosol mean particle size can also be determined. This quantity is

important for distinguishing smoke from dust, and for estimates of radiative forcing caused by the presence of aerosols in the atmosphere.

A dramatic example of detecting large plumes over land with UV wavelengths was obtained during the 1998 Mexican fires that covered the southern US and occasionally extended up to Canada. Figure 16 shows a simulated Triana view of aerosol optical depth corresponding to this event. The EPA used the TOMS data shown in the figure to consider possible exemptions from pollution standards. Triana scenes will be even more useful since they will be at higher resolution and at all times of the day. In this case, for example, current satellite observations missed the increase in the smoke plume that is known to have occurred later in the day. The smoke from these fires also caused a direct environmental risk when the air became unhealthy to breathe in parts of Texas and Florida. Other parts of the US are regularly affected by smaller amounts of smoke every year, such as from the annual Canadian boreal fires and California-Oregon fires. The hourly data from EPIC can be used as an environmental warning system for regions threatened by such smoke plumes. As with TOMS aerosol data, the EPA (Environmental Protection Agency) is expected to be interested in the higher time and spatial resolution EPIC data.

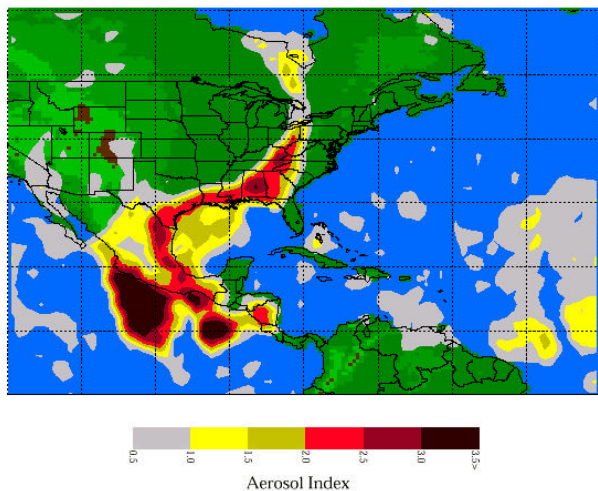


**Figure 16** Triana-EPIC simulation using TOMS data on absorbing aerosols over Mexico on May 16, 1998. The aerosol index is roughly equal to the optical depth. Particulates to the east of South America are Saharan dust.

EPIC aerosol data will be made available to the FAA (volcanic ash), US Park Service (smoke), EPA (smoke and dust), and others for their operational needs. The detection of volcanic ash is particularly important in the Northern Hemisphere Pacific rim region where there is frequent volcanic activity and a high density of aircraft routes. Volcanic ash plumes at 3 to 15 km have caused major damage to aircraft and in extreme circumstances could cause accidents.

### 5.1.3 Cloud Phase and Particle Shape Characterization

Triana measures visible and near-infrared reflectance globally from sunrise to sunset at an almost constant scattering angle between  $165^\circ$  and  $178^\circ$ . The scattering angle for any other satellite at a given location varies with time of day and overpass (e.g., Minnis et al., 1998). Triana's spatial and spectral coverage and the scattering angles resulting from its unique view are ideally suited for helping us to monitor clouds, a critical component of the climate system, and to determine the statistics of the global distribution of cloud particle shape.

In recent years, advances have been made in our capabilities for monitoring clouds and their constituents. However, statistically reliable measurements of the shapes of ice crystals comprising cirrus clouds are poorly known. Ice-crystal shape and size determine the basic reflectance properties of clouds. Cloud reflectance is a key factor in calculations of how the Earth responds to incoming solar radiation.

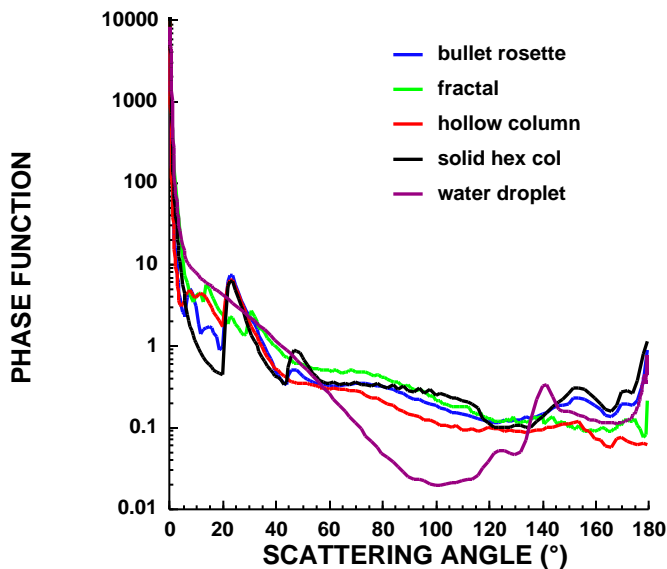


**Figure 17** Scattering phase function for various common cloud-particle shapes. Note the similarities in the change of the phase function with angle until the scattering angle exceeds  $160^\circ$ .

From in situ aircraft measurements, it is known that ice-crystal shapes vary considerably from cloud to cloud. But it is not known how frequently or in what conditions a particular crystal shape occurs. These shapes produce very different scattering phase functions (see Figure 17). Ice crystal habit is difficult to monitor because different crystal shapes can produce similar reflectances in a given direction by adjusting the individual crystal sizes. One means to differentiate one crystal habit from another is to analyze simultaneous measurements from two different angles such that the solutions for different habits yield distinctly difference reflectance ratios. The optimal pairs of angles for such measurements include one between  $160^\circ$  and  $178^\circ$  and another between  $60^\circ$  and  $180^\circ$  to maximize the relative differences in the scattering phase functions (e.g., Figure 17).

Nearly simultaneous measurements from two different satellites have been used to determine the correct optical depth by selecting the phase function that yields the same optical depth from both satellite views (Minnis et al., 1993). Because of differences in the shape of the phase function and the asymmetry factors, the optical depth for an ice crystal will differ from that for a water droplet at the Triana scattering angle ( $\sim 175^\circ$ ). Ratios of reflectance observed at angles other than  $175^\circ$  will also be considerably different at most angles (Figure 18a) thus providing an estimate of phase. Figure 18b shows a matched set of images from GOES-8 ( $75^\circ\text{W}$ ) and GOES-10 ( $135^\circ\text{W}$ ). The GOES-10 reflectances are generally smaller than those observed from GOES-8 which views the entire scene from a scattering angle of  $\sim 167^\circ$ , in the range seen from Triana. The ratios of the GOES-10 reflectances to those from GOES-8 show that, except in the areas with shadows, the values for the cold clouds (see Fig. 18b) are close to 1.0 while the warmer clouds have ratios closer to 0.85. These ratios are consistent with the results on the right in Figure 18a indicating that the colder clouds are composed of hexagonal ice crystals and water droplets comprise the lower clouds. Similar differences in the ratios exist for clouds composed of crystals having different predominant shapes (e.g. Fig. 17).

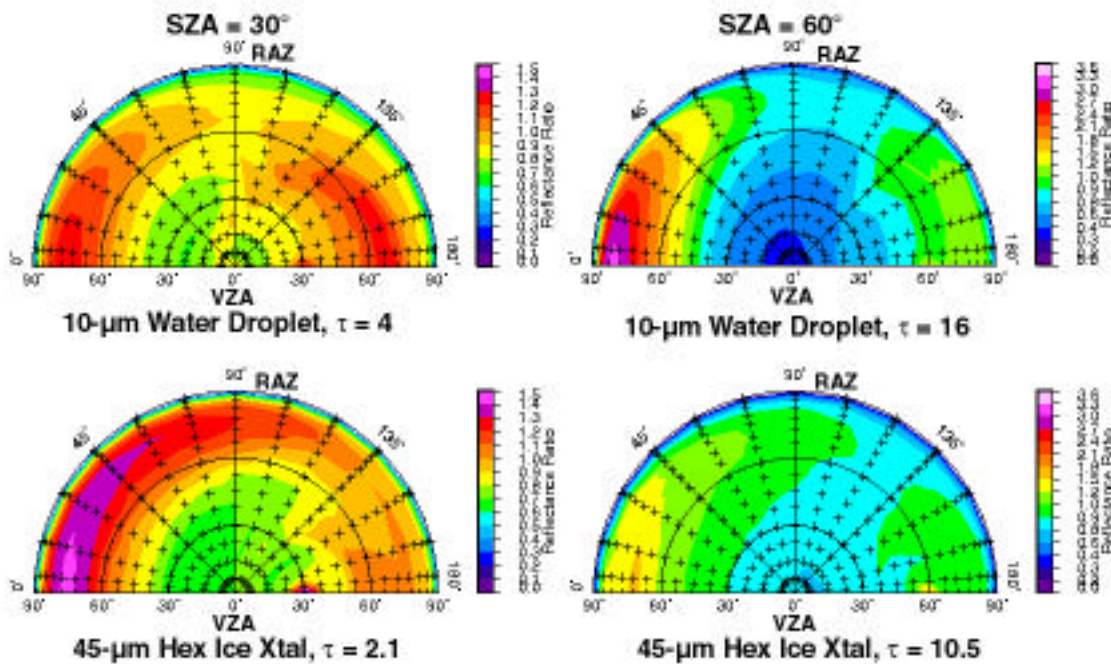


**Figure 18a** Angular dependence of  $0.65\text{-}\mu\text{m}$  reflectance ratios relative to the reflectance at a scattering angle of  $175^\circ$ . Ice crystal optical depth must be reduced to match the reflectance at  $175^\circ$  computed for the water droplet model. Note, the ratios for the water droplet at a given solar zenith angle (SZA) are generally different from the corresponding values for the ice crystal.

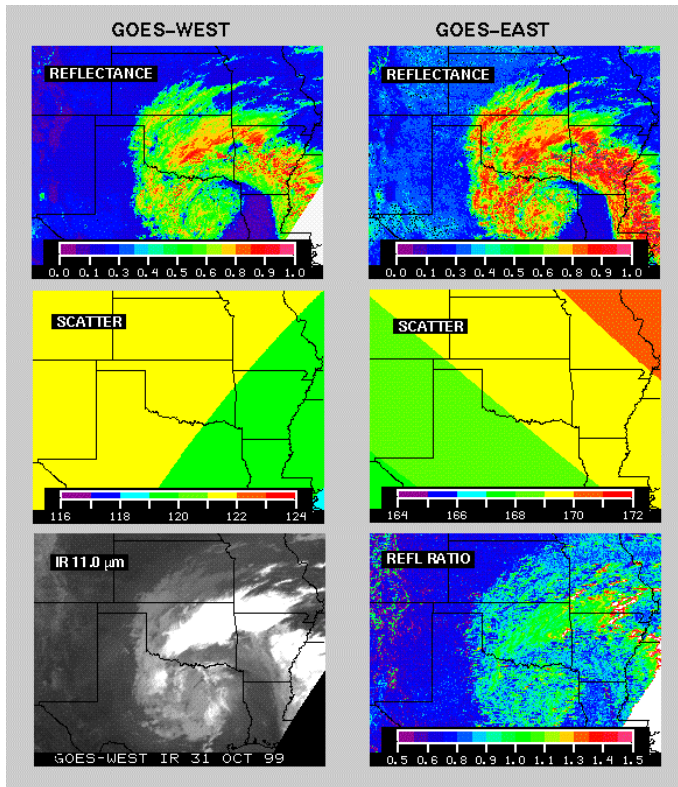


**Figure 18b** Reflectance, scattering angles, and reflectance ratios for matched GOES-8 (East) and GOES-10 (West) imagery taken over the central U.S. at 1700 UTC, 31 October 1999. The ratios differentiate low-level liquid water clouds (blues and light green) from high-altitude ice clouds (deep greens and reds).

One of the greatest stumbling blocks to using multiple satellite measurements is calibration. This obstacle can be eliminated by using the technique of Nguyen et al. (1999) to produce near-real-time intercalibration tables normalizing Triana and other satellites to a common standard. This technique

uses simultaneous data from two satellites with nearly identical viewing conditions to obtain a relative calibration from one to another. It is currently applied to GOES-8, GOES-10, GMS, NOAA-12, VIRS, and ATSR-2 using the NOAA-14 calibration as a standard. When Triana is in its prescribed orbit, its 645 and 870 nm channels will be calibrated against similar channels on the Terra MODIS instruments. This calibration can then be easily transferred to VIRS, the NOAA-14/15 AVHRRs, and the GEO satellites, including the new Meteosat which will have comparable visible channels, to facilitate scientific analyses of multiple satellite data sets.

Cloudy Triana pixels will be determined via multispectral thresholding against expected clear-sky reflectances. An initial clear-sky reflectance map will be developed for the 645 and 870 nm channels from existing databases used by the CERES program (Trepte et al., 1999; Sun-Mack et al., 1999). These databases will be updated for the 645 and 870 nm channels and for other channels using the initial Triana observations. Screening for clear pixels will involve both subjective—initially—and objective minimum reflectance techniques. Shadows will not be problematic because of the Triana scattering angles. Over ocean, the updated bi-directional reflectance model of Minnis and Harrison (1984) will be used for characterizing the reflectance patterns for clear ocean, except near the coasts. Appropriate sets of thresholds will then be established for

each channel and surface type to discriminate cloudy and clear pixels automatically in the Triana data set. The resulting cloudy pixels will be used in the algorithms for determining cloud height, while optical depth will be derived using assumed particle sizes and shapes as in Minnis and Smith (1998) based on the cloud height. The clear pixels will be used in other studies including the hot spot analyses discussed below.

A large database of cloud reflectances based on a variety of different particle shapes and sizes will be constructed for the two relevant Triana channels and, for the other satellites, all of the appropriate channels required for particle size, phase, and optical depth retrievals. Current retrieval algorithms will be applied to pixel-level data from the other satellites to obtain solutions for all of the various shapes. These results will then be matched to the Triana pixels. This matching will be accomplished by compiling groups of high-resolution LEO/GEO pixels into the 8-km Triana pixels. The optical depth for each pixel will be computed for each of the solutions using the Triana-observed radiances. Particle shape will be selected by determining which Triana-derived optical depth most closely matches its counterpart from the other satellite.

Extensive GEO and LEO data sets including GOES, GMS, AVHRR, and VIRS are currently downloaded and archived at NASA Langley Research Center. In the future, MODIS and Meteosat data will be included. These data sets will be used to establish a prototype, semi-operational pixel-matching algorithm that can be expanded in the future to a more operational process.

#### **5.1.4 Precipitable Water Vapor**

The amount of precipitable water vapor can be calculated from observations in two channels 870 and 905 nm, where only one (905 nm) is sensitive to water vapor absorption. As with other wavelength-pair analysis, radiative-transfer analysis (LOWTRAN) is used to generate tables (illustrated in Figure 19) for  $W$ , equal to the ratio

$$W = \frac{I_{905}}{I_{870}}$$

of measured radiances at the Triana observing angles.

The precipitable-water tables are directly based on analysis done for the MODIS instrument onboard the Terra satellite scheduled for launch in the near future (Kaufman

and Gao, 1992). The method was successfully applied to data obtained from AVIRIS (Airborne Visible Infrared Imaging Spectrometer), used as a MODIS simulator.

Triana-EPIC will be able to see clouds form and dissipate against a background of water vapor, thereby showing atmospheric modelers the processes that they cannot see at present. This will lead to an improved representation of clouds and cloud formation in general circulation models.

Since the water vapor measurement using W depends on backscatter of sunlight, it is able to detect total column water vapor. Infrared sounders depend on thermal contrast, and cannot give information on water vapor down to the planetary boundary layer. Yet much more water vapor is contained within this low-altitude layer, per millibar, than the layers above it. The EPIC  $I_{905} / I_{870}$  nm will give the only complete sunrise to sunset water-vapor data obtained from space, and will be able to match up with a similar once per day measurement from MODIS on the polar orbiting Terra satellite. With measurements of water vapor throughout each day, we can improve our estimates of latent heat transport, and improve our understanding of climate. A regional application of the effect of water vapor on the radiative forcing of dust aerosols has been discussed by Hsu et al. (1999a).

A further novel application to cloud height determination can be made with the total water vapor measurements. If the scene is cloud filled to at least a cloud fraction of 0.5, then the observed amount of total water vapor is greatly reduced since there is a large altitude gradient for water-vapor content above the Earth's surface. When the water vapor measurements from AVIRIS above a cloud are compared with AVIRIS cloud-top temperature measurements (made in the  $12 \mu$  infrared), there is a very good correlation as shown in Figure 20.

The Triana estimates of total precipitable water over cloud filled scenes will be used to estimate cloud heights and compared with the same scenes observed in the solar Fraunhofer line channel (393.5 nm). Cloud heights determined by the two methods (water vapor and the Ring effect from Raman scattering) will be compared. Cloud top temperature is a standard technique used to estimate cloud height, and is the basis for the ISSCP cloud height climatology database determined from AVHRR and GEO satellite data.

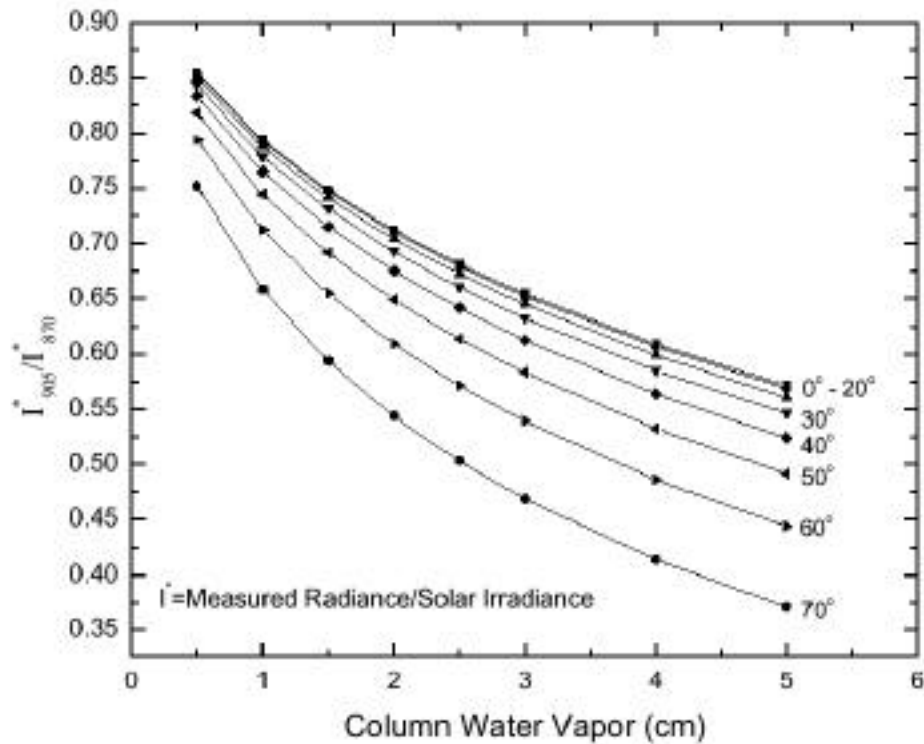


**Figure 19** An example of the sensitivity of the ratio of 905 to 870 radiances to column water vapor amount as a function of solar zenith angle (0 to 70°). The data were calculated from the LOWTRAN radiative transfer program.

Validation and calibration of the two methods of cloud-height determination will be made by comparing with infrared temperature based determinations using matched

scenes from MODIS, AVHRR, and GEO imagers.

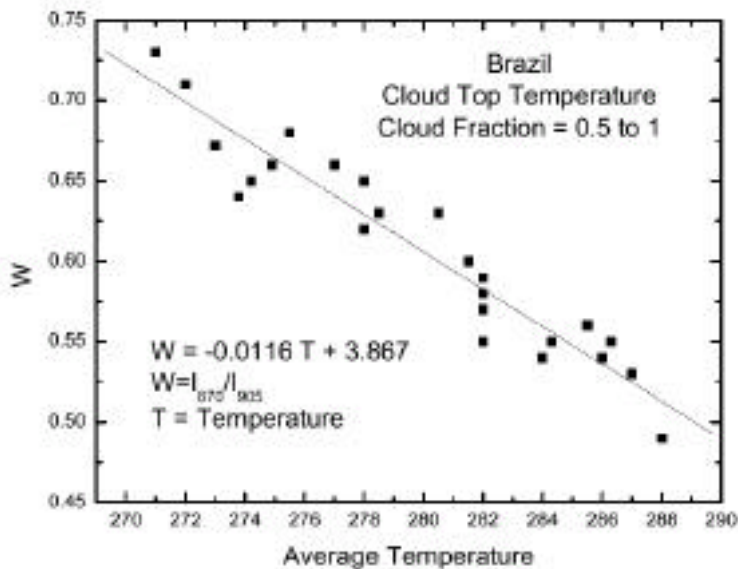


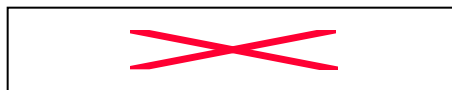
**Figure 20** The correlation of  $W=I_{870}/I_{905}$  with cloud top temperature T determined from the 12-micron channel from the AVIRIS instrument over Brazil.

### 5.1.5 Cloud Reflectivity (in Support of other Retrievals)

Cloud reflectivity  $R$  is calculated to support the ozone, aerosol, and UV irradiance algorithms. For ozone, it is necessary to estimate the amount of ozone beneath the clouds, when present, and to account directly for the additional backscattered radiance in the ozone absorbing wavelengths. The amount of aerosols can only be estimated for cloud-free pixels. This means that the aerosol index can only be converted into optical depth when the reflectivity is about 15% or less. Aerosol plumes (smoke or dust) frequently have reflectivities of about 15%. The presence of clouds is the largest factor in reducing the amount of UV reaching the ground at a given location. To first order, the UV irradiance is reduced by the fraction  $1 - R$ .

In addition to its support role, the reflectivity values can be converted into effective cloud optical depth for each pixel. As with any remote sensing instrument, the cloud fraction within a pixel cannot be determined so that only an effective optical depth can be calculated for that pixel.

The 340 or 388 nm LER (Lambert Equivalent Reflectivity) is calculated by requiring that the measured TOMS radiance  $I_{SM}$  match the calculated radiance  $I_S$  (see Equation 1) by adjusting a single free parameter  $R$  in the formal solution of the radiative transfer equation



where

- = viewing geometry (solar zenith angle, satellite zenith angle, azimuth angle, etc.)
- $R$  = LER (the combined effect of the surface, clouds, water haze, and aerosols)
- $P_o$  = reflecting surface pressure
- $S_b$  = fraction scattered back to  $P_o$  from the atmosphere
- $I_d$  = sum of direct and diffuse radiation reaching  $P_o$
- $f$  = fraction of radiation reflected from  $P_o$  reaching the satellite

The resulting values of  $R$  represent the LER of the scene from measured backscattered radiances originating from the ground, aerosols, and clouds as components of the reflectivity. Certain scenes, such as those containing ice or specular reflection, are distinctly non-Lambertian, as are clouds observed at large solar zenith angles.

In magnitude,  $R$  ranges from 0 to 1, but can be negative or greater than 1 if there are absorbing aerosols that are not taken into account or the reflecting surfaces are sufficiently non-Lambertian (e.g., sun-glint from ice). Another possibility for errors in  $R$  can occur if the phase functions of aerosols present in the atmosphere are not adequately approximated. In practice, the values of  $R$  are usually between 0 and 1 for the Nimbus-7/TOMS observations. Most exceptions are over regions of ocean sun-glint and after injection of volcanic aerosols into the stratosphere (e.g., after the 1983 El Chichon and 1991 Mt. Pinatubo eruptions). Corrections can be applied for these effects (Torres et al., 1995; Herman et al., 1993). When clouds are present, the scene reflectivity  $R$  is frequently composed of a mixture of sub-pixel clouds, the surface reflectivity, and possible aerosol backscatter. The approximation of the scene albedo by the LER (instead of the more complicated bi-directional reflectivity distribution) is improved by having a field of view (8-10 km) large enough to help average out the effects of individual clouds or surface features.

It is important to note that the cloud transmission of UV irradiance to the ground is approximately given by  $1-R$  with corrections that can be derived for solar zenith angle and satellite zenith angle (Herman et al., 1999a; Krotkov et al., 1999). These angles are approximately equal for Triana observations and fall between  $165^\circ$  and  $177^\circ$ . The Triana spacecraft cannot get nearer to the Earth-Sun line than about  $3^\circ$  before solar radio noise interferes with the telemetry transmission back to Earth.

### **5.1.6 Ultraviolet Radiation**

The amount of UV radiation that reaches the Earth's surface from the Sun can be estimated using a combination of radiative transfer calculations and the measured amounts of ozone, cloud reflectivity or cloud-optical depth, aerosol optical depth, and known amounts of Rayleigh scattering. While complicated, the methods for obtaining the amount of UV irradiance between 290 and 400 nm striking the Earth's surface at any location are well developed and have been applied to TOMS data (Krotkov et al., 1998, 1999; Herman et al., 1996, 1999b; Kalliskota et al., 1999). The amounts calculated have been successfully compared to ground-based measurements made by broadband instruments and spectrometers.

The importance of identifying the regions of high UV irradiance and correlating them with human, plant, and animal health is well understood (UNEP, 1991). Regions

such as Australia, the southwestern US, and most of the tropics are subject to high UV radiation levels. In Australia, the problem is recognized as a major public health problem (Green and Williams, 1993; Herlihy et al., 1994) as it is, to a lesser degree, in the US. The most common problems are increased incidence of skin cancer (de Gruijl and Van der Leun, 1993; Moan and Dahlback, 1993), eye cataracts (Zigman, 1993), and reduced yields in agricultural products (Bornman and Teramura, 1993; Teramura et al., 1990). An example of UV irradiance estimates possible from spacecraft observations and the correlation with skin cancer is shown in Fig. 21.

The difficulty with satellite estimates of UV irradiance has always been that the estimates are confined to the single time of the satellite overpass (usually near noon). The result has been that the variability of the cloud cover, and to a lesser extent the ozone variability, cannot be determined from the satellite data and compared with the ground measurements. With Triana-EPIC there will be measurements of ozone and aerosols once per hour, and measurements of cloud reflectivity every 15 minutes. This will put the spacecraft determination of UV irradiance on an equal basis when comparing with ground observing sites (e.g., Herman et al., 1999b, Correll et al., 1992; Weiler and Penhale, 1994; Zerefos et al., 1997).

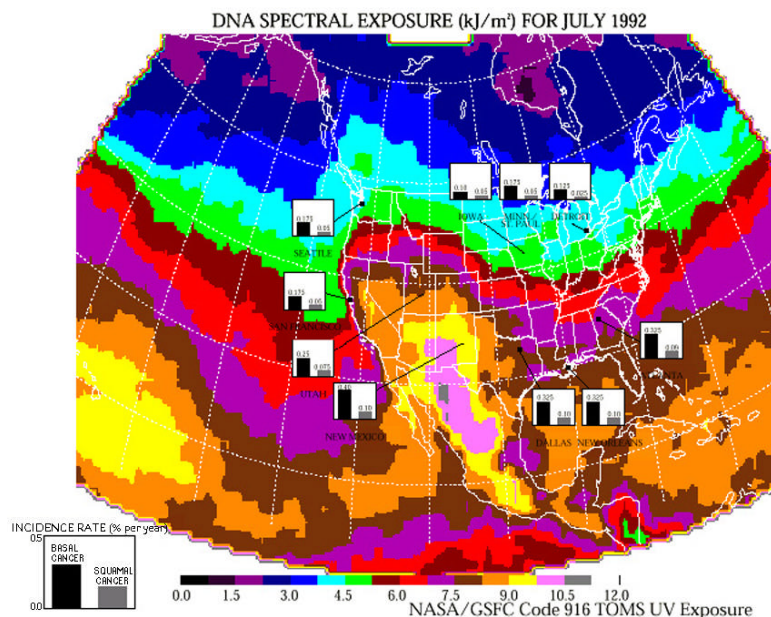


**Figure 21** UV irradiance weighted for DNA damage over the US determined from TOMS radiance measurements for July 1982 and a correlation with the incidence of skin cancer (Scientific American, July, 1996).

The most important variables affecting the amount of UV irradiance reaching the ground are latitude, cloud cover, and ozone amount. When all other biological factors are equal, the regional differences in cloud cover are the most important factor in determining the health risk to UV exposure. An example of this is the effect of summertime UV exposure on the similar populations that originated in England and now live in Australia or the US at similar latitudes. While there is a small decrease in ozone amount between the Southern and Northern Hemispheres, at the same latitude, there is a major decrease in cloudiness. The reduced cloudiness causes almost double the noontime UV exposure in Australia compared to the US (see Figure 22 for January and July). A similar condition occurs at the equator during the equinoxes when there is much less cloud cover in March than at the same latitude in September, while the ozone amount is approximately the same.

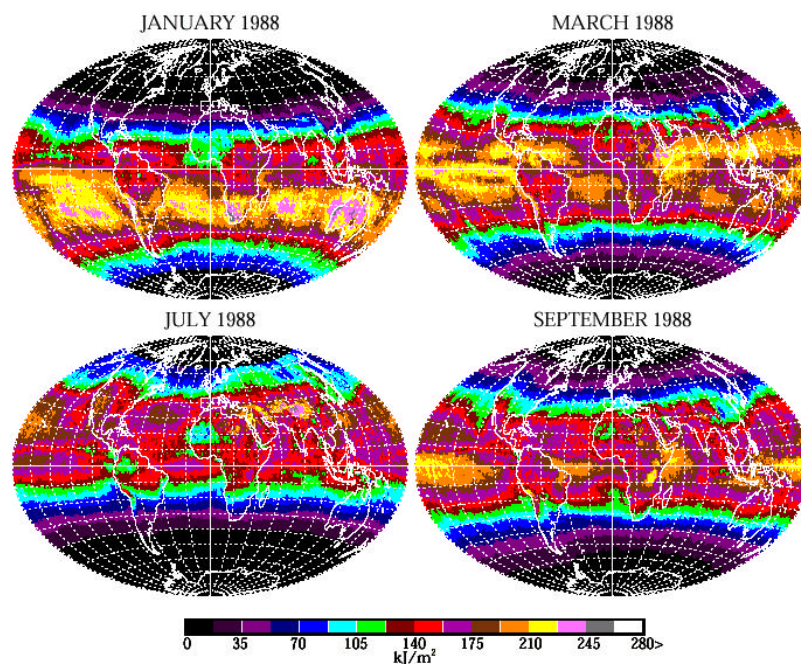


**Figure 22** Exposure to UV irradiance weighted for skin damage (erythemal weighting). Note the large differences between the summertime exposures in the Northern Hemisphere (July) and those at the same latitude in the Southern Hemisphere (January).

Other less extreme cases may depend on knowledge of the difference between morning and afternoon cloudiness to understand the biological impact of UV exposure in

a given region, and especially long-term changes in that exposure caused by ozone or climate change. This is why the global cloud measurements from Triana for the entire day will be important.

### 5.1.7 Hotspot Analysis

The angular distribution of radiation reflected by a three-dimensional surface that is illuminated by a directional source exhibits a sharp maximum in the retro-reflection direction. Indeed, when observed along the same direction as the incident radiation, only the directly illuminated structures are seen; no shadows are visible, thus there is a peak in the retro-reflected light. This effect is known as the opposition effect in astronomy, the Heiligenschein in meteorology, and the hotspot effect in remote sensing.

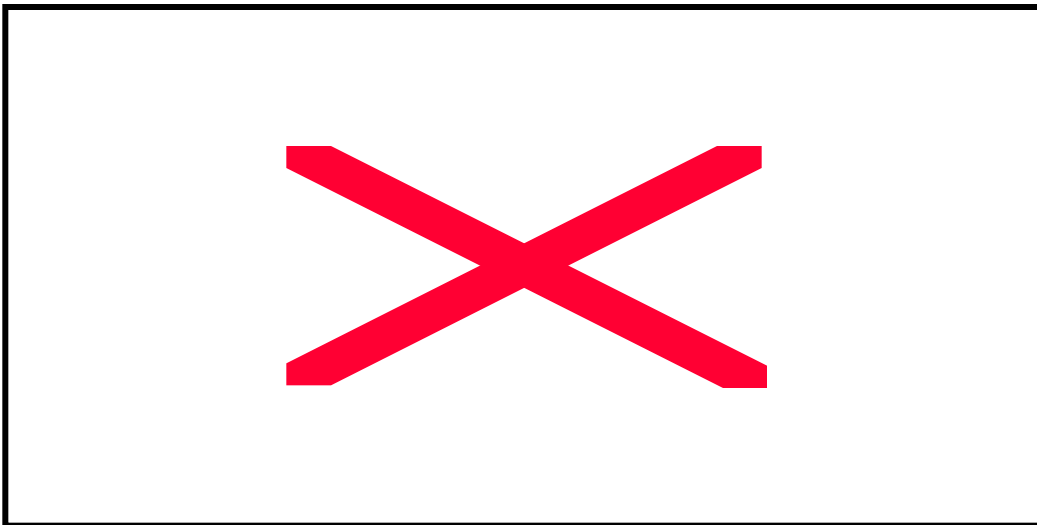


**Figure 23a** Schematic representation of the radiance enhancement between  $\pm 10^\circ$  from the Earth-Sun line at L-1 (Gerstl, 1999). W stands for full width at half maximum.

Located close to L-1 (4 to  $15^\circ$  from the Sun-Earth line), Triana will acquire images of the Earth near the solar retro-reflection direction. Such images will exhibit an angular signature, as schematically illustrated in Figure 23a (Gerstl and Simmer, 1986; Gerstl, 1988). This viewing direction is useful for the remote observation and monitoring of vegetated land surfaces because of the retro-reflection sensitivity to vegetation

characteristics, in particular canopy structure, vegetation leaf structure, vegetation health and stress situations, vegetation amount, and fractional land cover.

The enhanced radiances fall within an observation cone of about  $10^\circ$  around the Earth-Sun line. Since the Earth occupies only  $0.5^\circ$  in EPIC's field of view, the entire Earth is within the hotspot region. Under ideal clear sky conditions, the hotspot can cause a doubling of the radiance reflected exactly in the L-1 direction (Gerstl, 1988). The characteristics of the actual orbit around L-1 will allow observations away from the retro-reflection peak, as shown in Figure 23a. Actually, the full angular region between 4 and 15 degrees will be covered as the orbit evolves, thus providing observations of the "wings" of the angular signature.

Figures 23b and 23c depict examples of the anisotropic reflection properties of vegetated land surfaces. Such anisotropic effects are correlated with scattering and absorption events and enable the retrieval of several surface parameters (described below) from the remotely sensed angular distribution of the reflected radiation.

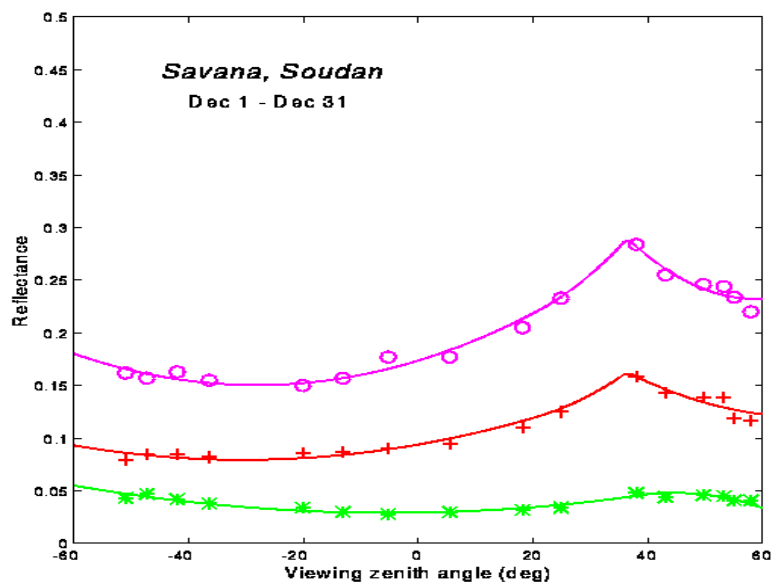


**Figure 23b** Satellite-measured BRDF distribution for 865, 670, and 443 nm, from a cut through the principal plane in POLDER observations. The reflectances are composed of data from different orbits and spatial resolutions between 15 and 30 km. Although the POLDER angle scale is different, the radiance peak in the retro-reflection direction can be clearly seen.

Hotspot analysis will yield forest-canopy structure data such as canopy height and leaf-phytoelement size and shape by using pre-established correlations between canopy structural parameters and the hotspot parameters {W, C}, where W is the hotspot angular width and C the hotspot strength or magnitude (Gerstl, 1988, 1999). These are results not obtainable by classical remote sensing measurements that primarily rely on spectral signatures (e.g., the vegetation index planned for MODIS). Therefore, the angular signatures from Triana canopy hotspot measurements promise to be an ideal complement

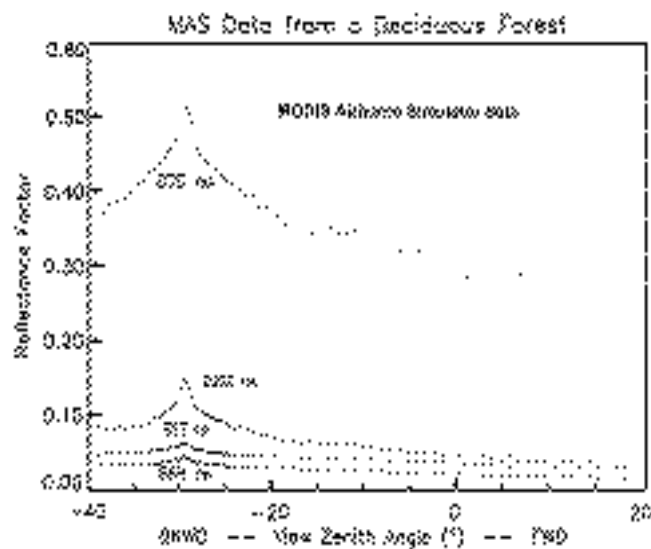


**Figure 23c** Measured canopy hotspot angular distribution from 20 km above a deciduous forest in visible and near infrared wavelengths from the MODIS Airborne Simulator at solar zenith angle of -29 degrees and 50 m spatial resolution.

to the existing spectral index characterizations of vegetation cover. Continuous observations with Triana will allow us to establish time-series of ecological parameters for all biomes by longitude, latitude, wavelength, and season, which will form the basis data set for a new global hotspot land vegetation ecology (Gerstl, 1999).

Triana data coupled with Terra data will allow an estimate of the hotspot contribution to Earth radiation budget. While this is expected to be small, it may be important as we place tighter and tighter requirements on our estimates of global change.

### 5.1.8 Upper Atmosphere Dynamics

*“The correspondence of total ozone to isentropic pressure suggests the former as a diagnostic of vertical air motion in the lower stratosphere . . . . Ultimately, this application of total ozone measurements is limited by the once daily asynoptic sampling of TOMS, which is inadequate to resolve small scale structure continuously in time.”*

*Salby and Callaghan, 1993*

Triana does indeed fulfill this gap.

Upper atmosphere dynamics will be studied using ozone as a tracer together with data assimilation models and direct high time and space resolution observations from Triana. The first-time use of sunrise to sunset data will greatly improve the retrieval of winds and wave structure through data assimilation.

#### Planetary and Other Waves

Waves can produce an uplift of stratospheric layers in certain regions and down drafts in others. When an air parcel goes up, its pressure diminishes and so does its ozone partial pressure (it is important to note that it is the partial pressure that decreases and not the ozone mixing ratio). When the layer where most of the ozone is concentrated is uplifted, the total ozone, *i.e.* the ozone content of a unit section column, diminishes. Thus from total ozone measurements one can detect atmospheric waves. This has been demonstrated by comparing TOMS or TOVS measurements with NMC or ECMWF analyses. However, the construction of TOMS or TOVS total ozone images requires a time lag of several hours, during which the spatial structures may vary; this will not be the case with TRIANA data, which will provide instantaneous views of the total ozone field.

The ozone fields retrieved from TOMS and TOVS have indeed been used up to now to detect planetary waves. This has been possible because the spatial extent of these waves is large and their motion relatively slow. We believe however that Triana will bring a better monitoring of planetary waves, due to its instantaneous planetary view associated with high temporal resolution.

Figure 24a displays the ozone field as Triana can view it<sup>1</sup>; the map has been constructed using total ozone observations from TOMS. The high ozone zones found around the Arctic region are the signatures of planetary waves (Teitelbaum et al., 1998). Figure 24b shows the corresponding geopotential field on the 475K isentropic surface, calculated from ECMWF analyses. Comparing Figure 24a and 24b, it is clear that high ozone zones correspond to downward motions of isentropic surfaces.

In addition, the space resolution of Triana will allow an almost continuous monitoring of gravity waves, whose small horizontal scale could not hitherto be resolved by TOMS or TOVS. In particular, Triana should be able to detect the variations of total ozone content induced by large vertical uplifts of air masses within localized areas, associated with orographic waves propagating much higher than the tropopause. The detection of other types of gravity waves, such as those triggered by deep convection, frontogenesis or jet instabilities, is still open to discussion. Knowing more about the distribution of gravity waves in the stratosphere (especially orographic waves) is an important input for general circulation models.

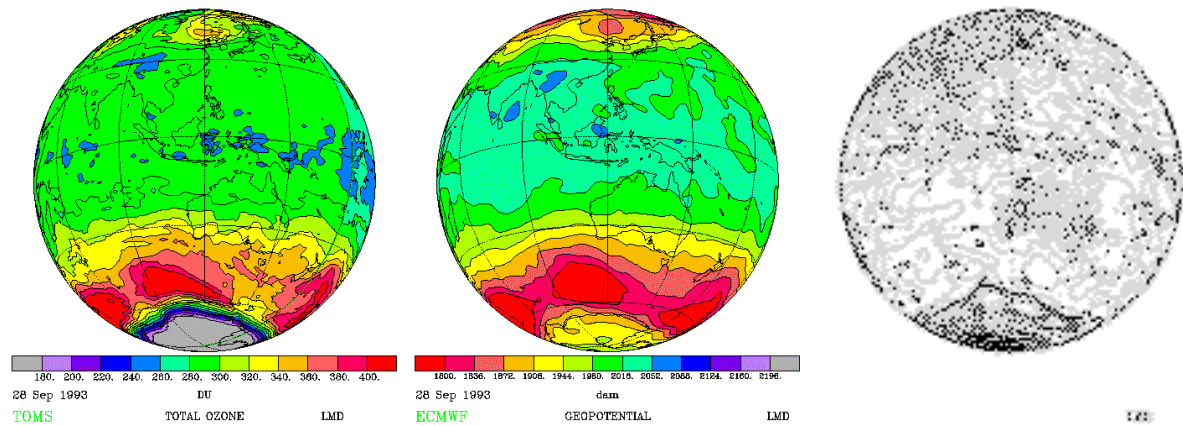


**Figure 24** Depictions of (a) a simulated Triana ozone view, (b) the corresponding geopotential field on the 475K isentropic surface, and (c) the corresponding Ertel potential vorticity map.

<sup>1</sup> All fields are represented here from a Triana viewpoint. The season is close to the spring equinox, the most interesting period for investigating the polar vortex in connection to the ozone hole. We suppose that the phasing of Triana on the Lissajous orbit can be programmed in such a way that at the equinoxes the Earth can be seen at the maximum angle of about 15 degrees with respect to the Earth-Sun axis, allowing maximum visibility of the spring side polar region.

## The Polar Vortex

Figure 24 shows the southern ozone hole surrounded by a border where there is a strong gradient of total ozone. This border in general coincides with the vortex edge defined on an isentropic surface near 475K. This is illustrated in Figure 24c that depicts the corresponding Ertel potential vorticity (EPV) map at 475K calculated from ECMWF analyses. The Antarctic polar vortex appears on the Ertel's potential vorticity (EPV) map. The equatorward edge of the vortex region is shown as a thick line in the figure.

On the other side of the Earth, view centered at 45°W, the structure of ozone (Figure 25) is very different. Such a structure appears when an uplift of isentropic surfaces occurs in the vortex edge region. Then the edge dilates by separation of

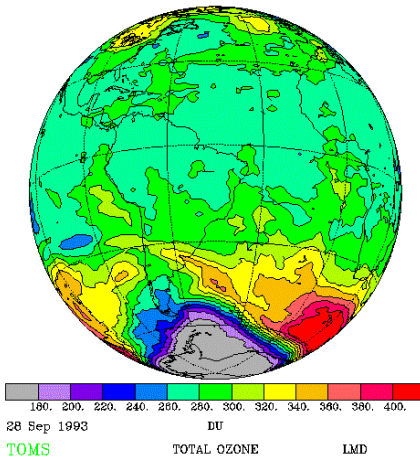


**Figure 25** Simulated Triana view of ozone, centered at 45°W.

potential vorticity isolines producing what has been called “macrofilaments” (Teitelbaum et al., 1998). It is clear that Triana will see this type of structure with higher spatial and temporal resolution. Contrary to the filaments produced by horizontal velocity gradients, which lead to fine structures and mixing in an irreversible process, “macrofilaments” are partly due to elastic, meteorological reversible processes. It is important to study how such reversible processes do affect the mixing of air masses and diffusion across the vortex edge region.

## Ozone Miniholes

Triana will allow the study of the existence of EPV anomalies, anticyclones and cyclones in the vicinity of the tropopause, and their displacements with a precision not yet attained. Ozone miniholes are localized regions (a few thousands of km<sup>2</sup>) of low total ozone content. The dynamical basis is explained in Hoskins et al. (1985). In the vicinity of the tropopause differential advection often produces a localized decrease (increase) of Ertel's potential vorticity; the EPV decrease (increase) appears together with an anticyclone (cyclone). The EPV anomaly extends its influence upward under the form of an uplift of air masses in the case of an anti-cyclonic wind, or a downward motion when

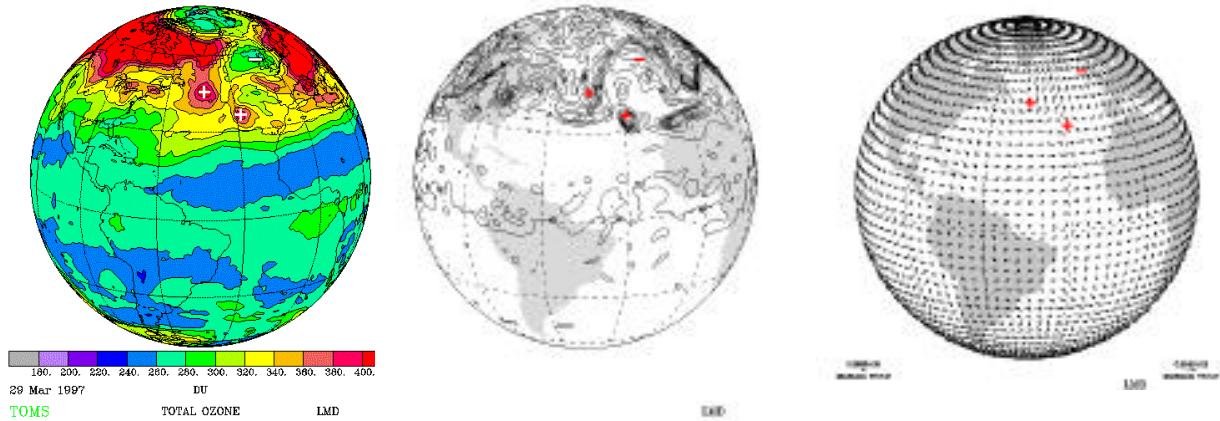


**Figure 26** Depictions of (a) an ozone map, (b) the corresponding EPV map on the 325K isentropic surface, and (c) the wind at 300 mb.

the wind is cyclonic. The consequences on total ozone of this vertical movement are discussed by Salby and Callaghan (1993).

An example is shown in Figure 26a. The total ozone TOMS map shows two localized increases (+) and one decrease (—) of ozone. In Figure 26b we can see the corresponding EPV map on the 325K isentropic surface. EPV anomalies appear at the same geographical positions as the total ozone anomalies. Finally Figure 26c shows the wind at 300 mb; one anticyclone and two cyclones are seen in the wind field.

We can add another possibility although of some speculative character. Mini-holes are the signature of an uplift of isentropic surfaces and then of the cooling of air masses. When the season and the latitude indicate the possibility of low background temperature, this uplift decreases the temperature further and may induce the formation of a PSC. The relationship between uplifts, miniholes, and PSC has been shown in McKenna et al. (1989) and in Teitelbaum and Sadourny (1998).

#### Filamentary Structure of the Vortex Edge

Triana measurements may also be most useful for detecting the filaments induced by quasi-two-dimensional differential advection in the stratosphere.

Fine scale layering of the lower stratosphere is often observed in ozone vertical or horizontal profiles. It was demonstrated recently that those laminae in ozone profiles which cannot be explained by gravity waves are essentially associated to filamentary structures generated by differential advection along isentropic surfaces. Up to now, the existence of filaments has only been proven in numerical simulations by the means of contour dynamics (Dritschel and Saravanan, 1994); the only experimental support is partial and relies on aircraft observations and vertical soundings (Waugh et al., 1994). Triana has the potential to provide us for the first time a full two-dimensional view of the filaments and their evolution in time. Modeling and theoretical considerations suggest that, in absence of vigorous vertical mixing, these filaments should survive for more than two weeks until their vertical scale is reduced to a few tens of meters and horizontal scale to about ten kilometers. The production of such filaments at the vortex edge is critical for the exchanges and mixing of air masses between inside and outside the polar stratospheric vortex. In particular, during the polar night, they can induce transport of chemically perturbed vortex air to mid-latitudes, resulting in photochemical ozone destruction there; in late winter or spring, filaments can also transport ozone depleted vortex air to mid-latitudes. Present observations such as the ones by TOMS are unable to resolve such filamentary structures, and similarly the crude resolution of operational meteorological analyses produces filtered potential vorticity maps that do not resolve these filaments.

Although filaments are local structures both in the vertical and in the horizontal, high-resolution total ozone will be helpful to detect these structures when located near the altitude of ozone highest concentration (level of potential temperature about 475-500K). Calculations done with profiles with laminae show that the variation in the total ozone may be of the order of 5% to 20%, well within the accuracy of Triana instruments.

It is clear that the possibility to follow almost continuously the deformation of such structures will bring new information on lower stratosphere dynamics. Tracking these filaments will bring direct information on the winds. (All major weather forecasting centers are already preparing the assimilation of tracers such as ozone in their operational analysis systems.) Observation of the filamentary structures will bring valuable information on the evolution of small-scale structures and mixing processes in the lower stratosphere and allow studying their relationship with gravity and orographic waves. They will be very useful to validate high-resolution transport studies and chemical models.

Possible synergism of Triana with other space missions like UARS, POAM, and ENVISAT are being studied. We are also considering complementing ozone with other dynamics tracers like aerosols and possibly PSCs. In parallel, we plan to use our second generation atmospheric GCM (LMDZ-T) whose vertical resolution is currently being increased to 50 levels to simulate and eventually assimilate Triana data.

### **5.1.9 Advances in the Arctic from Triana**

The L-1 orbit of Triana improves the view of the high latitudes during the sunlit part of the year (see Figures 5 and 6). This is much improved over the view of high latitude locations available from standard geostationary satellites (GOES, GMS) that are also capable of viewing from sunrise to sunset. Instruments aboard GOES or GMS have their fields of view centered on the equator, and their images of high latitudes therefore contain too much geometric distortion for many remote sensing applications. Triana's orbit and good spatial resolution give EPIC an ability to make major contributions to problems in Arctic atmospheric science and climate study, including stratospheric ozone depletion and UV radiation, tropospheric aerosols (the Arctic "haze"), and polar meteorology.

#### Stratospheric Ozone Depletion in the Arctic

Arctic ozone depletion events, significant examples of which have occurred during half of the 1990s' northern-hemisphere springs (e.g., Müller et al., 1997), are more complex and geographically less extensive than the similar depletion in the Antarctic. The conventional understanding of ozone depletion in the Arctic suggests that springtime ozone depletion is not as severe as in the Antarctic due to a less pronounced northern hemisphere polar vortex (Solomon, 1999). In the northern hemisphere, greater atmospheric wave activity induced orographically by land results in a warmer stratosphere with less PSC (Polar Stratospheric Cloud) formation during winter, and earlier springtime stratospheric warmings. Dynamical considerations that have so far limited the size of Arctic ozone depletion events also render them more geographically variable. The coarse spatial resolution of TOMS is often inadequate to resolve the spatial structure of the Arctic polar vortex boundary and to follow the complete time history of an Arctic ozone depletion event that might cover a limited geographical area.

The Arctic is host to a considerable human population and more extensive land ecosystems compared to Antarctica. These may be adversely impacted by enhanced UV radiation under stratospheric ozone depletion events. Monitoring springtime Arctic ozone depletion, including the mapping of enhanced UV-B radiation at the ground (Lubin et al., 1998), will be a valuable activity for both ecological studies and public health awareness in northern high latitude communities (e.g., Scandinavia; Moan and Dahlback, 1993). The Triana 14-km resolution (at high latitudes) will provide major improvements to satellite UV monitoring capability: first in the ability to validate more accurately such remote sensing retrievals with ground-based spectroradiometer measurements made by NSF Office of Polar Programs or ARM at Barrow, Alaska and by European researchers at Tromsø; second in the ability to resolve more accurately the spatial variability in the surface UV radiation field.

There is a well-known coupling between CO<sub>2</sub>-induced tropospheric warming and stratospheric cooling (Fels et al., 1980; Shindell et al., 1998). Austin et al. (1992) have shown how an increasing tropospheric CO<sub>2</sub> burden may eventually lead to Arctic ozone depletion events that approach the severity of those in the Antarctic. EPIC will be able to monitor stratospheric ozone concentrations throughout the Arctic with high spatial resolution for several years. The observed ozone variability can be correlated with stratospheric and tropospheric temperatures and dynamics (from NCEP or ECMWF reanalyses, or infrared sounder data) and also with any observed trends in Arctic tropospheric mean temperature. This capability will enhance our understanding of the relationship between stratospheric ozone depletion and the various factors that govern temperature in the lower stratosphere.

#### Arctic Tropospheric Aerosols

There is a well-known anthropogenic aerosol burden in the Arctic troposphere, known as the “Arctic haze”. It is now recognized that tropospheric aerosols play an important role in regional climate forcing (Kiehl and Briegleb, 1993). In the Arctic, tropospheric aerosols have an opacity that is sufficient to affect directly shortwave radiative fluxes and tropospheric heating rates (Pilewskie and Valero, 1993; Tsay et al., 1989; Valero et al., 1984, 1988). There is also a potential “indirect” radiative effect of aerosols, in which the presence of aerosols (acting as condensation nuclei) biases the cloud droplet size distribution toward a smaller effective radius, which thereby increases cloud opacity and albedo for a given liquid water path (e.g., Platnick and Twomey,

1994). This indirect radiative effect has not yet been verified by experiment in the Arctic (it is difficult to quantify empirically with standard field methods), but it must be a focus of future Arctic climate studies. The surface radiation budget is known to be sensitive to the particle size distribution in the extensive stratiform cloud cover that is a prominent feature of Arctic meteorology (Curry and Ebert, 1992).

To date, most of our knowledge about the geographic and temporal variability in Arctic haze has come from a handful of ground stations, particularly in Alaska (e.g., Shaw, 1982; Polissar et al., 1998). Alaska has proven to be a useful location for these studies, because Alaska is affected alternately by Arctic and Pacific air mass systems. In the Pacific air mass system, aerosol chemical composition is characterized by enrichment in elements related to sea salt. In the Arctic air mass system, pollutants such as excess sulfates are transported over long distances to Alaska. The abundance of these excess sulfates has been shown to exhibit a general negative gradient from northwestern to southeastern Alaska, indicating a long-distance source to the northwest of Alaska (e.g., industrial activity in or near the Russian Arctic). The overall seasonal cycle in the Arctic haze involves a maximum tropospheric aerosol burden during late winter and spring, with a decrease toward a minimum during mid-summer due primarily to removal by increased precipitation. For future climate study, it will be important to (a) better characterize the temporal and spatial variability in aerosol opacity with a better resolution than is available from a handful of ground stations, and (b) identify possible transport pathways. EPIC's unique UV/visible wavelength capability for aerosol opacity retrieval should facilitate greater understanding of the mesoscale and large-scale behavior of the Arctic haze. During the spring and summer, much of the Arctic exhibits low enough surface albedo (e.g., tundra, open ocean, broken sea-ice cover) that EPIC's aerosol retrieval algorithms will be effective. The high time resolution of the EPIC imagery, combined with large-scale views of the Arctic, will maximize the number of cloud-free scenes from which we can map aerosol opacity.

### Arctic Meteorology and Climate Change

The Arctic is expected to exhibit a particularly sensitive response to radiative forcing from anthropogenic greenhouse gases, due to climatological mean surface and lower tropospheric temperatures near the triple point of water. Satellite passive microwave observations of Arctic sea-ice have already revealed downward trends in total sea-ice extent that are consistent with a "global warming" scenario (Cavalieri et al., 1997). Although the fundamental "ice-albedo" and "cloud-radiation" feedback

mechanisms have been identified (Curry and Webster, 1999), GCM simulations of present-day Arctic climate remain inadequate. Current GCMs tend to make large errors in simulating cloud amount (Chen et al., 1995; Curry et al., 1996), and also tend to underestimate natural climate variability in the Arctic (Battisti et al., 1997).

While modern field studies such as the year-long Surface Heat Budget of the Arctic experiment (SHEBA, led by NSF Office of Polar Programs during 1997-98) are providing many important advances in our understanding of local thermodynamics, cloud microphysics, and radiation, future work must involve tropospheric dynamics. The Arctic surface radiation budget is strongly modulated by the pervasive stratiform cloud cover, and this cloud cover is governed to a large extent by the advection of warm air and moisture from lower latitudes (Curry and Herman, 1985; Pinto, 1998). The mean poleward transport of water vapor is found to be positive at most low-to-mid tropospheric levels (Serreze et al., 1995), but with considerable geographic variability, and with an understanding of interannual variability still yet to be realized. In order to fully understand the response of the Arctic climate system to possible anthropogenic changes in “greenhouse” gas forcing, it is necessary to understand the dynamical factors that govern meridional energy transport between lower latitudes and the Arctic, such that we can simulate this energy transport with GCMs. High-time-resolution imagery of large-scale cloud fields, and retrievals of water vapor, can help us reach this goal. According to Stone (1997), “A basin-wide assessment of the temporal and spatial relationship between temperature and cloud distributions is needed to verify simulations of Arctic climate. This must include an evaluation of the advective processes that impact those distributions. Because it is impossible to collect the necessary data to accomplish this task at the surface, we must rely on satellite data ultimately to make these assessments and to monitor Arctic climate in the future.”

Clearly then, a satellite instrument that can provide useful imagery for synoptic meteorology in the Arctic can make important contributions. Standard geostationary instruments cannot image high latitudes without considerable geometric distortion. Existing polar-orbiting instruments, such as the Advanced Very High Resolution Radiometers (AVHRR) aboard the NOAA spacecraft, offer the potential for many images over the course of a day due to the convergence of the orbital subtracks at high latitudes. However, there is at present no unified data collection strategy in the Arctic for these spacecraft, which typically provide only line-of-sight telemetry and therefore require antennas located in the Arctic to collect Arctic data. Piecing together AVHRR (or

similar) images for long time periods, with high temporal resolution (several images per day), from disparate viewing angles, and covering large geographic areas (i.e., the entire sub-Arctic and Arctic), is cumbersome to the point of near-impossibility.

During the sunlit half of the year, Triana's whole-Earth view overcomes these limitations. We should mention that EPIC will not be perfect for this purpose, due to its lack of thermal infrared channels. EPIC's limitation to wavelengths shorter than 1.1 microns will make cloud detection problematic over regions containing near-100% sea-ice cover. Over Arctic land masses during summer (e.g., tundra), and over the open ocean, clouds will be easily identified by radiance contrast with the underlying surface. Over the Arctic Ocean in the marginal ice zone (sea-ice concentrations less than 50-60%), image texture can be used to distinguish clouds from the underlying high-albedo surface (e.g., Ebert, 1987; Lubin and Morrow, 1998). Over uniform high albedo surfaces, such as the majority of multiyear ice in the central Arctic Ocean, neither radiance contrast nor texture is entirely reliable for identifying clouds. However, for climate study, this limitation of EPIC is partially offset by the fact that we are interested mainly in tracking air masses moving from lower latitudes into the Arctic. Also, for study of Arctic ozone depletion describe above, retrieval of total column ozone abundance is not hampered by a high albedo surface. Thus, we are not claiming that Triana will be an *ideal* platform for all meteorological applications over the Arctic. Nonetheless, Triana *will* overcome many of the viewing limitations with existing satellite platforms, and in conjunction with continuous detailed surface data from the ARM site at Barrow, Alaska (Stamnes et al., 1999), should further our understanding of Arctic meteorology and climate.

#### **5.1.10 Validation**

Because of the unique viewpoint of Triana, all Earth orbiting satellites are in view throughout the day. In particular, the near-noon polar orbiting satellites TOMS, SeaWifs, MODIS, and AVHRR will view the same scenes whenever Triana is obtaining global data from sunrise to sunset. Since the EPIC wavelength channels were selected to match closely with TOMS in the UV and with MODIS in the visible, the data products will be very similar and can be directly compared. These comparisons will validate both the calibration and data reduction algorithms. Other near-noon observing satellite instruments have similar wavelength channels and data products that can also be included in validation studies (e.g., SeaWifs, AVHRR, and CERES). In addition to validation, the

greater temporal coverage of EPIC will be used to extend their observations to both morning and afternoon hours.

There are numerous ground-based measurements made of ozone (e.g., Dobson network), aerosols (e.g., Aeronet), and UV irradiance (e.g., Brewer network) throughout the day at many locations on the Earth's surface. Triana-EPIC can be directly compared with these data throughout the sunlit portion of the day. The most powerful test of the Triana-EPIC data will be for those locations that have instruments from all three networks at the same location as well as an aerosol lidar. Cloud properties will also be validated using other ground sites maintained by the DOE ARM Program. Unlike the satellite comparisons, the ground-based validation will provide high temporal resolution, but at a fixed location.

The combination of satellite and ground-based validations will allow the Triana data to be used with confidence to extend both the satellite and ground-based observations into regions where neither can reach.

## **5.2 NISTAR**

### **5.2.1 Scientific Goals and Objectives**

The Triana NISTAR measures the whole-Earth radiation in three absolute (self-calibrated) broad band channels:

- 1) A visible to far infrared (0.2 to 100  $\mu\text{m}$ ) channel to measure total radiant power in the UV, visible, and infrared wavelengths
- 2) A solar (0.2 to 4  $\mu\text{m}$ ) channel to measure reflected solar radiance in the UV, visible, and near infrared wavelengths
- 3) A near infrared (0.7 to 4  $\mu\text{m}$ ) channel to measure reflected IR solar radiance
- 4) A non-absolutely calibrated photodiode (0.3 to 1  $\mu\text{m}$ ) channel for calibration reference for the spectroradiometer

The earliest precedent would be Suomi's black and white flat-plate radiometers on the first Tiros satellite in 1963. Like NISTAR, Suomi's radiometers were designed to study the radiation balance of Earth, had a field of view encompassing the whole disk of the planet (from LEO), and co-flew with an imager.

Since Suomi, wide-field-of-view (WFOV) radiometers continued flying in LEO, but they were paid less and less attention by the radiation community. The tendency in radiation balance research has been toward a more statistical mechanics point of view, in which every pixel on Earth is accounted for separately. This has many advantages, including the production of monthly-average maps and the separation of cloud from non-cloud effects. But another reason for disinterest in WFOV data was that the orbits were just too low for them to be of much use. They could not reveal meaningful patterns, except for something as big and long-lasting as El Nino, because the spatial resolution was too low; and they could not be added up to give the integrated global picture. The big fields of view were a jigsaw puzzle impossible to fit together perfectly and many assumptions about diurnal cycle were necessary to fill the unsampled times of day. The NISTAR returns to the simple thermodynamic view of the Earth that Suomi was pursuing, but from a much better orbit that does not require merging data from successive orbits or making assumptions regarding the diurnal cycle.

The NISTAR also begins the process of looking at the Earth as a planet, rather than as a collection of pixels. In spite of Earth's complexity when seen from a worm's-eye LEO view, this complexity must average out over time and space to produce a planet satisfying some relatively simple laws. Some of these laws are not known yet, for example those relating global cloudiness to global warming. We are as unlikely to discover those laws from a worm's-eye view as to discover the perfect gas laws from tracking individual gas molecules. NISTAR cannot entirely solve this problem, but it is a first step down a worthwhile path which has, for a time, been somewhat abandoned.

Technologically, NISTAR is the *avant-garde* member of the Triana instrument suite. Like Suomi's experiment in its time, the NISTAR pushes the limits of absolute radiometry. Indeed, radiometry experts initially said that it couldn't be done. With any practical collection aperture at L-1, they said, there were too few photons to cause measurable changes in detector temperature. The Sun was easy, but the Earth, with a radiance less than  $10^{-5}$  that of the Sun, was very hard. The NISTAR is the answer to this challenge. It achieves a remarkable 0.1% accuracy without cryo-cooling. And it defines a technological path forward that will someday lead to spatially resolved absolute radiometry of Earth from L-1, affording the advantages both of the pixelated view and the integrated global view simultaneously.

The Triana NISTAR radiances will be used in several ways:

- (a) to make integrative measures of global change (longwave channel);
- (b) to estimate Earth albedo;
- (c) to attempt to interpret the near-infrared to visible albedo ratio;
- (d) to test EOS-CERES algorithms in an integral sense;
- (e) to provide an extensive integral test of how well radiative transfer in the Earth-atmosphere system is understood.

These usages are discussed in corresponding sub-sections below.

### **5.2.2 Global Change from NISTAR**

Our original hopes for using the NISTAR to measure global change were muted by the realities of the Triana halo orbit (ranging from 4 to 15 degrees away from the Earth-Sun line and not the same from one year to the next). This use of NISTAR would only be perfect if Triana were exactly at L-1. Especially in the shortwave, the halo orbit scrambles global and seasonal change in a way that would be nearly impossible to unscramble in a few-years mission.

However, because of:

- (a) surface and atmosphere thermal lag times,
- (b) the relatively slow change of Earth's effective temperature with latitude, and
- (c) the high longwave opacity of the atmosphere outside the 8–12 micron window,

the longwave radiance is much less affected by this scrambling than the shortwave. Thus, in spite of the halo orbit, we expect NISTAR to be able to “take the Earth's temperature” in an integral sense and obtain a result at least as meaningful as (although certainly not equivalent to) the observed globally averaged surface temperature.

Of course, unlike the ~4000 separate instruments in the surface network, the NISTAR is a single absolutely calibrated instrument with no data voids over the ocean. (Although there is one large data void over the Earth's night side where the Earth is 1–2 degrees cooler, perhaps this can be predicted using global models and known thermal lag times.) And the NISTAR automatically integrates over half of the diurnal cycle. Thus, in spite of the orbit drawbacks, we think that the NISTAR longwave result will be a valuable addition to the small arsenal of integrative measures of global change.

### 5.2.3 Computation of Shortwave and Near-Infrared Albedo

The radiance measured by NISTAR can be represented as

$$L_{\Delta\lambda} = ADM_{\Delta\lambda} M_{\Delta\lambda} / \pi, \quad (1)$$

where  $M_{\Delta\lambda}$  is the flux leaving the entire Triana-viewed hemisphere in all directions and  $ADM_{\Delta\lambda}$  is the effective anisotropic directional model for the wavelength interval  $\Delta\lambda$ . The value of the ADM depends on the scenes comprising the hemisphere and their angular positions relative to the satellite and Sun as given by the solar zenith angle  $\theta_o$ , viewing zenith angle  $\theta_v$ , and relative azimuth angle  $\phi$ . Estimation of the flux from the Triana radiance requires a value of  $ADM_{\Delta\lambda}$  for each measurement because the scene changes as the Earth rotates under the satellite. For simplicity, the shortwave Triana ADM is designated  $ADM_T$ , while the longwave ADM is  $ADM_L$ .

The shortwave ADM can be estimated from the EPIC data at time  $t$  as

$$\chi_T(t) = \frac{\sum_{i=1}^N \mu_o R_i(t) A_i}{\sum_{i=1}^N \mu_o R_i(t) A_i / \chi(K_i(t), \theta_o, \theta_v, \phi)}, \quad (2)$$

where  $R_i$  is the weighted average reflectance for the 443, 645, 870, and 905 nm channels for EPIC pixel  $i$ ,  $A$  is the pixel area,  $\mu_o = \cos\theta_o$ ,  $N$  is the total number of pixels used, and  $\chi$  is the normalized bi-directional reflectance factor for scene type  $K$  that is determined through the cloud screening process and the geography corresponding to the location of pixel  $i$ . The values of  $\chi$  will be taken from lookup tables like those used by CERES (e.g., Suttles et al., 1988). Figure 27 shows a Galileo flyby image of Earth, showing sun-glint region. Figure 28 depicts the pattern of  $\chi$  for clear ocean from Minnis and Harrison (1984) simulated for three of the Triana positions viewing the Pacific Ocean. Note, the bright area near the middle of the globe corresponds to the regions most likely to be affected by sun-glint. The reflectance for clear ocean increases toward the limb because of enhanced Rayleigh and aerosol scattering.



**Figure 27** Galileo flyby image of Earth, showing sun-glint region.

The albedo for the hemisphere is

$$\alpha_{SWT}(t) = \pi L_{SW}(t) / \chi_T(t) / S. \quad (3)$$

where  $S$  is the insolation over the viewed sunlit portion of the Earth. The value of  $\alpha_{NIRT}$  can be derived using the average reflectances from the 870 and 905 nm channels to compute  $R_i$  from (2). The near-infrared albedo  $\alpha_{NIRT}$  can be estimated from (3) using the measured near-infrared radiance  $L_{NIR}(t)$  and  $\chi_{NIRT}$ . Unless there are significant differences in the weightings of  $R_i$  for the near infrared and the total shortwave in (2) or if near infrared bi-directional reflectance models become available, then the ratios for the radiances and fluxes will be almost identical. With proper temporal averaging, these albedo values can be compared directly to GCM-derived albedos to verify the climate model calculations.

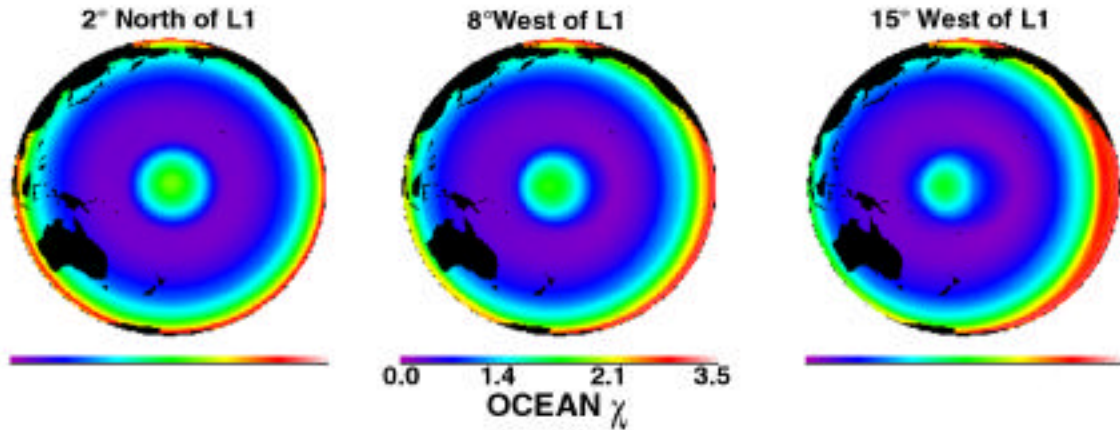


**Figure 28** Variation of normalized bi-directional reflectance factor over clear ocean for simulated Triana views of the Pacific Ocean. Sun-glint area corresponds to the bright region near the center of each image.

The longwave ADM could also be estimated as

$$\gamma_T(t) = \frac{\sum_{i=1}^N L_{IR}(t)_i A_i}{\sum_{i=1}^N L_{IR_i}(t) A_i / \gamma(K_i, \theta, \phi)}, \quad (4)$$

where  $L_{IR}$  is the narrowband infrared radiance for some imager pixel  $i$  and  $\gamma$  is the limb-darkening function from some established lookup table (e.g., Suttles et al., 1989).

Although the EPIC does not have infrared channels, it may be possible at some point in the Triana program to use infrared radiances from the matched pixels from other satellites as discussed earlier or from CERES as discussed below. In that manner, it would be possible to provide a reasonable estimate of the OLR for the hemisphere viewed by Triana.

#### 5.2.4 Test of EOS-CERES Using NISTAR and EPIC

The EOS-CERES and NISTAR broadband radiometers do not directly measure the same quantity, first because of the full day required for CERES to see every pixel on Earth compared to NISTAR's instantaneous view, and second because the flux measured by NISTAR bears little relation to the "top-of-atmosphere flux" data product from CERES. They share only the use of the same broad shortwave and longwave wavebands (CERES has no NIR channel).

Nevertheless, the barriers to using NISTAR as an integral test for CERES data products are surmountable. We think the effort to do so is worthwhile *not* because NISTAR is better calibrated (it isn't), but because NISTAR tests exactly those approximations which CERES must use to move from a single-time, single-angle view to a time- and angle-averaged view. While the CERES approximations are highly evolved, they necessarily involve assumptions which make the final data products much less certain than the underlying calibrated radiation measurements.

Via modeling and interpolation using auxiliary data sets and assumptions about diurnal scene variations (Young et al., 1998), CERES is producing a synoptic data set of albedo and OLR (outgoing longwave radiation) on a 1° grid every 3 hours. This synoptic data set can be convolved with scene-appropriate angular-directional models (ADMs) and summed over all Triana-viewed Earth pixels to simulate the NISTAR measurement at each synoptic time. The EPIC will be required for scene identification.

Any one such comparison would of course be hard to interpret. As a large catalog of such comparisons is accumulated, however, sharper conclusions may be drawn by subsetting the catalog in various ways. For example, each synoptic hour will provide a comparison over a particular part of the globe so that problematic geographical regions may be discernible.

Differences between the NISTAR and convolved CERES radiances will constitute an upper bound on the total error in the CERES global albedo and OLR because the Triana viewing geometry is in one of the most sensitive portions of shortwave ADMs. Flux errors from CERES will likely be less than the Triana-based estimate because the multiple angle view from the CERES scanners will average out many of the ADM errors.

If the Europeans successfully launch GERB, the first Geostationary Earth Radiation Balance experiment, in 2001, it should also be possible to test GERB against NISTAR when GERB views only daylit parts of the Earth.

### **5.2.5 The Ratio of Near-Infrared to Visible Albedo: Implications for Climate**

Anomalies have been discovered in the ratio NIR/VIS of near-infrared to visible albedo of clouds measured from aircraft (Stephens and Tsay, 1990; Francis et al., 1997;

Valero et al., 1997, 1999) and from the Nimbus-7 satellite (Collins, 1998). Current radiative transfer models cannot explain these anomalies. This was part of the motivation for adding a near-infrared channel to NISTAR.

Most studies of this anomaly were based upon data sets of a few hours duration from aircraft campaigns, and thus could be dismissed as ephemeral or unrepresentative. Therefore, it came as somewhat of a surprise when a similar anomaly was discovered in the global record from the Nimbus-7 satellite, recurring continuously from 1979 to 1987 (Collins, 1998). Because the NIR channel on Nimbus-7 was wide-field-of-view, the anomaly could not be attached to individual Earth pixels, but it was revealed by Collins using the method shown in Fig. 29. The ratio NIR/VIS has long been used as a measure of differences in cloud radiative properties between actual and modeled cloud systems (Stephens and Tsay, 1990). Anomalies in the measured spectral albedo ratio can also be linked directly to anomalies in the magnitude of atmospheric absorption (Collins, 1998).

This EPS image does not contain a screen preview.  
It will print correctly to a PostScript printer.  
File Name : Triana.fig2.ps  
Title : Graphics produced by IDL  
Creator : IDL Version 4.0.1 (sunos sparc)  
CreationDate : Thu Jul 3 15:54:35 1997  
Pages : 1

**Figure 29** Ratio of near infrared to visible albedo as a function of broadband albedo for climate model CCM3 (solid line) and Nimbus-7 ERB observations (dashed line). Lines represent the mean ratio for ocean regions between 50S and 50N for 1979-1987. Vertical bars indicate the range of albedo ratios computed for each individual year.

Figure 29 plots the NIR/VIS albedo ratio versus the total shortwave albedo as a dashed line, while a solid line shows simulations from the NCAR CCM3. The Nimbus-7 data and model simulation are global and extend from 1979 to 1987. Farther to the left in the plot (relatively cloud-free conditions), the observed and modeled albedo ratios are

close. Farther to the right (increasing cloudiness and/or cloud albedo), the observations and simulations increasingly diverge, regardless of cloud type or cloud phase. The anomaly occurs for all tropical and mid-latitude ocean regions and exhibits minimal seasonal and inter-annual variability. Almost identical anomalies are obtained when the Nimbus-7 data are compared with radiative transfer calculations based upon International Satellite Cloud Climatology Project (ISCCP) cloud data; therefore the anomalies are not an artifact of the CCM3 climate model.

Since Nimbus-7, no broadband near-infrared channel has been flown on a radiation space instrument. NISTAR not only restarts this measurement, but also provides several significant improvements over Nimbus-7. Perhaps the most important improvement will be the much better calibration and stability of the NISTAR radiometers. The Nimbus shortwave and near-infrared radiometers gradually degraded in the space environment (Kyle et al, 1995; Tashima and Hartmann, 1999). Calculations of the spectral albedos which include and exclude the degradation, and analysis of the time series of the spectral anomalies in the Nimbus data, both suggest that the long-term changes in the Nimbus instruments do not affect the detection of a cloud-albedo anomaly (Collins, 1998). Nonetheless, the conclusions from the Nimbus analysis should be evaluated with an independent set of observations.

The near-infrared radiometer will serve several purposes: first, it will help to test the Nimbus-7 result of Collins (1998) with accuracy and signal to noise ratio far superior to the Nimbus-7 ERB instruments. Second, it will provide a globally integrated test of the episodic but highly time- and space-localized findings of discrepant near infrared to total cloud albedo ratios (Stephens and Tsay, 1990; Francis et al., 1997; Valero et al., 1997). Third, because the near-infrared channel is sensitive to vegetation and snow/ice cover in addition to clouds, the near-infrared to total ratio is an attractively simple and fundamental analysis tool for studying global change, and Triana is the perfect vantage point to begin using that tool. (No current or planned LEO or GEO Earth radiation budget satellites have a broadband near-infrared channel, although CERES is apparently planning to add one in the post-2003 timeframe, which should serve as a nice complement to that on Triana.)

Simulated time series of the shortwave albedos and spectral albedo ratios for the Pacific Ocean are shown in Figures 30 and 31, respectively. The values are calculated for a subsatellite point of 0N, 160W for which 88% of the planetary surface viewed from

Triana is covered by ocean. For simplicity, we have assumed that Triana will view this point once per day. The modeled time series for 1984 is derived by averaging fluxes computed from the NCAR Column Radiation Model applied to 3-hourly atmospheric state information from ISCCP (Collins, 1998). The observational time series is constructed by averaging fluxes measured by the Nimbus-7 wide-field-of-view radiometers. Although the correct procedure for computing the radiation at L-1 involves

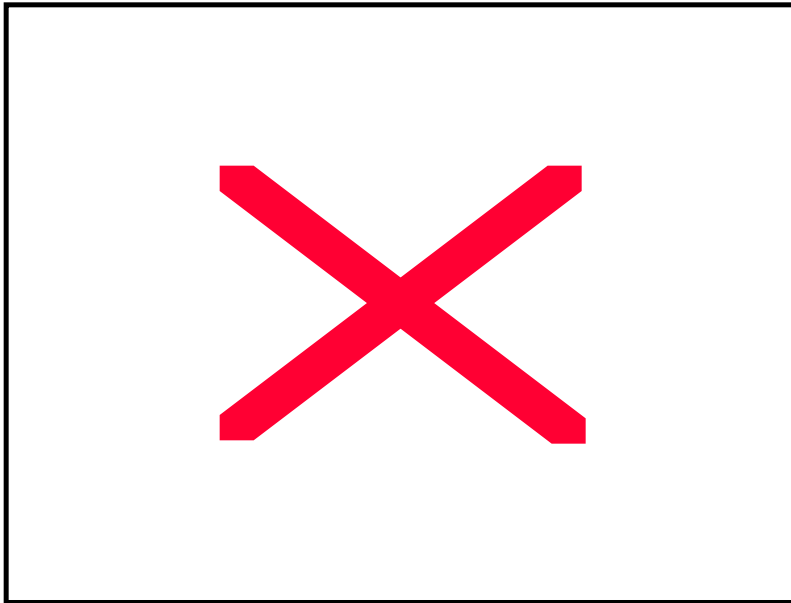


**Figure 30** Simulation of modeled and measured shortwave albedo for 1984 over the Pacific Ocean for a sub-satellite point at 0N, 160W. The calculations using the NCAR Column Radiation Model are shown in green, and the estimates based upon the Nimbus-7 broadband observations are shown in red.

integrating over the radiance field, geometrical averaging of fluxes provides

reasonably accurate estimates. The ISCCP calculations are sampled at local noon, corresponding to the local noon equator crossing time of Nimbus-7.

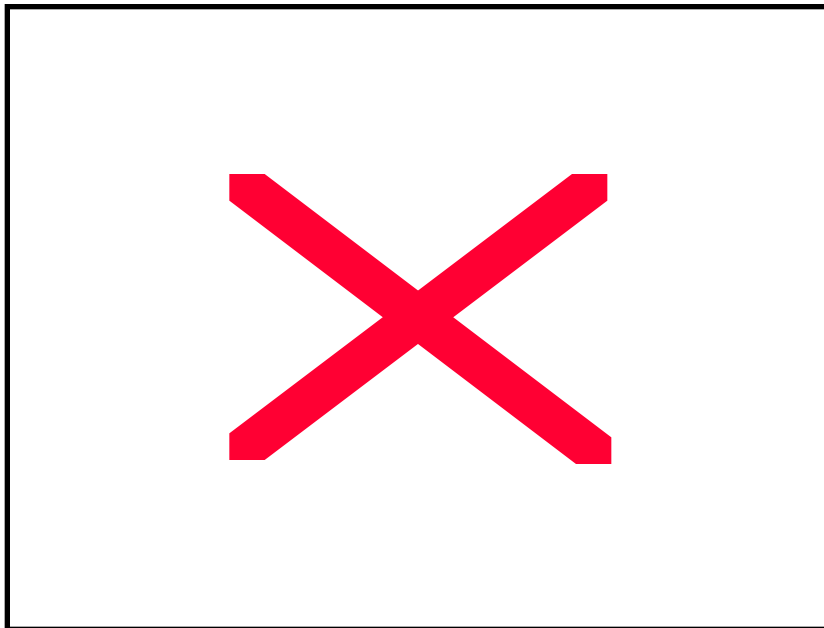


**Figure 31** Simulation of modeled and measured ratios of near-infrared to visible albedo. Temporal and spatial sampling are identical to Fig 30.

Figures 30 and 31 illustrate that while the model is able to reproduce the observed albedo time series, the modeled albedo ratio is consistently larger than the observed albedo ratio. The results also show that there is considerable monthly and seasonal temporal variability in the albedo and albedo ratios, showing the necessity of long time series to acquire the needed information. Variability on seasonal and interannual time scales will be used to track the anomalies in cloud spectral radiation associated with synoptic weather patterns (e.g., the Madden Julian oscillation) and with ENSO.

If the measured not the modeled lines in Figs. 29 and 31 are true, it would signify a major uncertainty in the Earth's energy balance. Other lines of evidence point to a similar conclusion, notably the globally averaged record of shortwave insolation at the surface, which shows a considerable deficit compared to global models. But this remains controversial.

While NISTAR, like Nimbus-7's NIR channel, cannot resolve individual cloud masses, it is clearly of interest to begin to look at the NIR/VIS ratio on a global scale with a modern radiometer. We believe that because of its intrinsic interest to the vegetation, cloud, and snow/ice communities, this ratio also has the potential to become, in future, an important global change variable.

### **5.2.6 Tests of Radiative Transfer Models**

Comparison of the spectral albedos from Triana against model calculations will require an extensive modeling infrastructure. The model calculations will require information on the cloud physical and microphysical properties, atmospheric thermodynamic profiles, profiles of ozone, and spectral surface albedos. In the analysis of Nimbus-7, the cloud and atmospheric properties were obtained from the NCAR GCM and from the ISCCP data sets. For Triana, equivalent data sets can be obtained by combining data from Earth Observing System (EOS) satellites, from operational meteorological centers, and from the Triana cloud products. In order to calculate spectral albedos as measured by Triana, it is necessary to specify spectral albedos in the same wavelengths at the Earth's surface. The Nimbus-7 study was limited to ocean regions since spectral albedos for the ocean surface have very small uncertainties. The visible and near-infrared albedos for land surfaces and the polar caps are much less certain. Observational data is limited to small geographic regions, and the spectral albedos

calculated with land-surface models (for example, the land models used in coupled GCMs) have not been validated over most of the globe. Since the Nimbus-7 spectral radiometers had wide field-of-view apertures, spectral land surface albedos cannot be inferred using data from these instruments. However, for Triana it will be necessary to model radiative transfer over land and ice-covered surfaces as well as over ocean regions. Work is already underway for characterizing surface albedo at near-infrared wavelengths, 870 and 1600 nm, from AVHRR and VIRS (e.g. Sun-Mack et al., 1999). The effort to measure surface albedos over enough near-IR wavelengths to derive relatively accurate values globally will continue using additional channels on MODIS and other Terra instruments.

A strategy will be developed for analyzing the Triana data using the modeling infrastructure developed for the Nimbus-7 measurements. This strategy can be thoroughly tested before the launch of Triana. Like Triana, Nimbus-7 also imaged the entire disk of the planet as viewed from the orbital altitude. Thus the analysis techniques originally developed for Nimbus should be applicable to Triana. The first step is to compute spectral albedos for land and ice from a global land-surface model (LSM). We will use the NCAR LSM (Bonan, 1998) or comparable model to generate these albedos. The albedos will be generated from a simulation of the Nimbus time period using observed sea-surface temperatures. The LSM, like many models of its class, includes a realistic time-varying prescription of the types and geographic distribution of vegetation (Bonan, 1996). The comparison of Nimbus-7 data against model calculations will be extended to land and ice surface using albedos from the LSM. We will then test the sensitivity of the results by varying the spectral albedos within a reasonable range of uncertainty. The spectral and broadband albedos from the land-surface model will be also evaluated with data from CERES (broadband only), field observations, and the MODIS data. Extensive MODIS clear-sky spectra should become available for oceanic and continental regions during late 2000. It should also be possible to compare just the Triana data for the Pacific Ocean basin against the model. This comparison should be minimally affected by uncertainties in the land-surface albedos.

Once such a modeling infrastructure is available, the possibilities for further tests of radiative transfer models become great, not just with NISTAR but also with EPIC. Because of Triana's simple viewing geometry and relatively simple data processing requirements compared to LEO satellites, scientists and students would be able to study a wide variety of phenomena without many of the complexities usually associated with

remote sensing. Because of the lunar calibration for EPIC and absolute calibration for NISTAR, the scientific community would be able to focus on geophysical applications of a stable, high-accurate data set. This could have important repercussions both for remote sensing and climate.

### **5.3 Plasma-Mag**

The Plasma-Mag instruments are intended to measure the magnetic field and the velocity distribution functions of the electron, proton, and alpha components of the solar wind (Faraday cup) at high time resolution. A much-improved time resolution is possible because Triana is a 3-axis stabilized spacecraft permitting near-continuous measurements at several times per second. Previous solar-wind measurements from the spin-stabilized WIND spacecraft could only be made when the Faraday cup pointed towards the Sun. The system to be used to reduce and interpret the data from the Plasma-Mag instruments is derived from the algorithms in use for WIND, which have been shown durable and well suited for scientific work.

Plasma-Mag contains a triaxial fluxgate magnetometer that will investigate solar-wind magnetic fields with a sensitivity level of better than 0.1 nT. The present design has been optimized for small size, low power, simplicity, and a very large dynamic range. Using the latest technology, it achieves a dynamic range of almost 8 orders of magnitude in field measurement capability simplifying its implementation aboard the Triana spacecraft.

The tophat electrostatic analyzer will make measurements of the electron between 3 eV and 2 KEV. The 3D measurement will be accomplished by electronically simulating the data sampling of an electron spectrometer on a spinning spacecraft. The instrument has a set of anodes distributed uniformly in azimuth, each with a field of view  $50^\circ \times 7^\circ$  in azimuth and elevation.

In addition to Sun and solar-wind studies, the data will also be used to provide early warning of solar events that might cause damage to power generation, communications, and other satellites (see Figure 32 for an example of Plasma-Mag measurements). Together, the Plasma-Mag suite of instruments will provide a 1-hour warning to the appropriate agencies that safeguard electrical equipment on Earth and satellites in Earth orbit. Present plans include routinely giving the data to NOAA with

only a 5-minute data processing delay from detection of an event at the Triana spacecraft position to the time that it is delivered.

The data shown in Figure 32 are obtained with WIND instruments that are similar to those carried onboard Triana. The similarity allows the algorithms and analysis techniques to be adapted to the new instruments with a great degree of certainty for success. Triana instruments are an improvement over those used previously, especially because of the 3-axis stabilized spacecraft. Because of this, the frequency of measurements will be much higher, allowing the scale in Figure 32 to be minutes instead of days. The high-time resolution of the measurements is necessary for revealing the wave structure of charged particles streaming past the Triana spacecraft. Triana, combined with other spacecraft already at L-1, will allow the detection and analysis of large-scale magnetic and plasma structures.

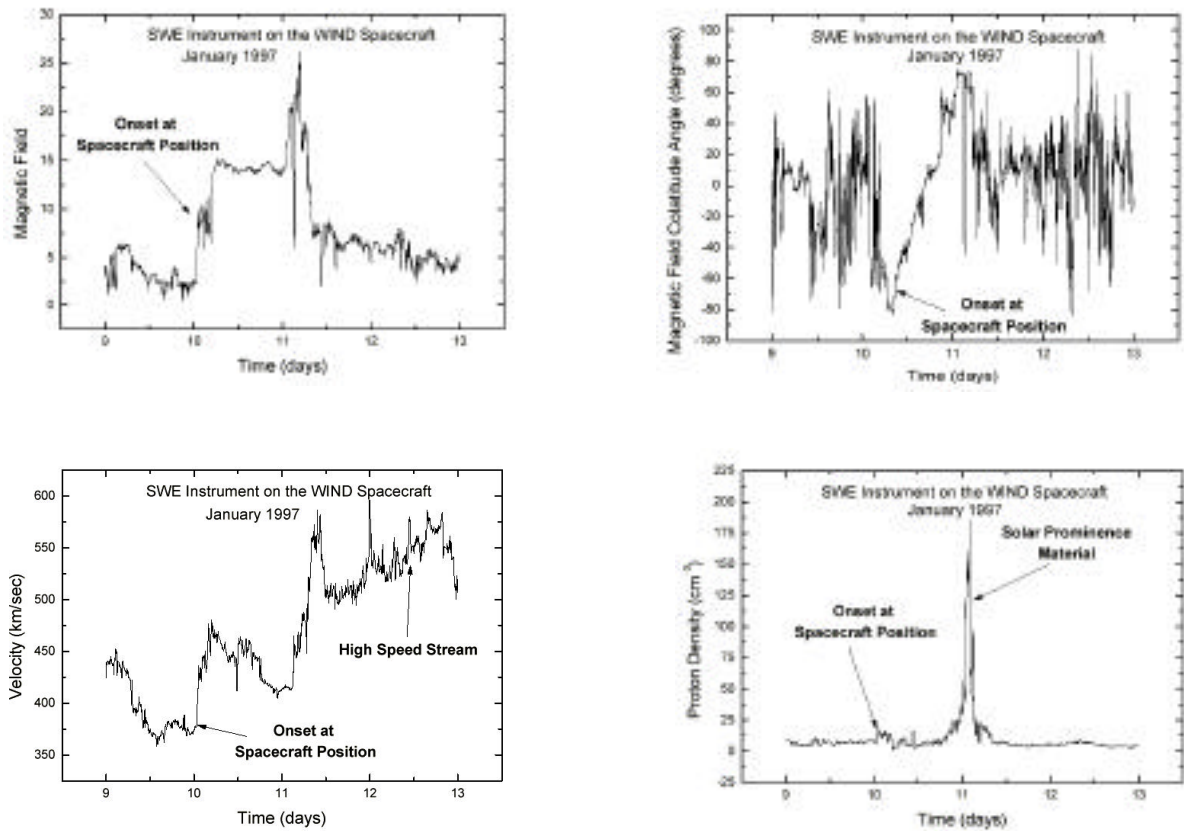


**Figure 32** Simulation of the Triana Plasma-Mag Instrument detection of a solar event showing the magnetic field, magnetic field angle change, solar wind velocity, and the particle density. The data are from the SWE instrument on board the WIND spacecraft from January 1997.

Because of the growth of satellite communications for civilian and military purposes, monitoring of the solar weather has become a mandatory function of government. Plasma-Mag will add to, or replace, the first generation space-weather monitors, such as WIND, IMP-8, and ACE. For example, ACE, the most recently launched, is concentrated upon solar wind isotopic composition, rather than particulars of the solar wind flow. Thus, Plasma-Mag provides an essential augmentation of present solar wind observations.

### **5.3.1 Scientific Goals and Objectives**

In the recent past, the emphasis in solar wind research has been on its composition (Ulysses and ACE) and on phenomena at large heliocentric distances (Ulysses, Voyager). At 1AU, Plasma-Mag will contribute new information at low solar latitudes about Coronal-Mass Ejections (CMEs), magnetic clouds, and the electron “super halo”. This will be an improved follow-on investigation to the data provided from WIND. Plasma-Mag studies will be focused on two major problems – 1) the source and structure of the slow solar wind, and 2) mechanisms for heating the solar corona.

The mechanisms for heating the solar corona to temperatures that are much hotter than the photosphere are not well understood. Waves in the solar wind appear to undergo a turbulent cascade to heat the wind at small scales. Reconnection events also lead to heating and acceleration of particles. More generally, the coupling between magnetic and electric fluctuations and particle distribution functions is a fundamental plasma interaction, important in a variety of contexts. The mechanisms are not well understood, and are difficult to study directly.

The improved time resolution of Triana/Plasma-Mag provides an opportunity to determine the mechanism by which small-scale fluctuations dissipate in plasmas. A time resolution of less than 1s would provide information to determine how the plasma responds to the simultaneously measured magnetic fields. It would also provide critical observational input to test and further develop theories of wave damping and the heating and acceleration of particles expected to take place near the proton cyclotron frequency. Moments of the distribution functions, at the highest resolution, would make it possible to determine if the waves are Alfvénic (or on a higher frequency extension of this wave mode), and if so, to discern their direction of propagation. Detailed distribution functions would also enable us to test kinetic theories of the interaction, since the time resolution enables measurement at spatial scales comparable to the proton gyroradius.

### 5.3.2 Multi-Point Solar Wind and Space Weather Studies

Triana, as a second spacecraft at L-1 in a halo orbit similar to ACE, but with its orbit phase-shifted by  $90^\circ$ , would significantly improve the accuracy of the National Space Weather predictions. The improvement will occur because one spacecraft will always be near the ecliptic plane and Sun-Earth line. This effort will **not** require the continuous transmission of the highest resolution measurements. On-board calculated averages and moments transmitted at significantly lower rates (e.g., 1/min) will be sufficient.

It has been well established that the magnetic field and plasma scale length in interplanetary space is significantly less than  $80 R_e$  (Earth-radius), the radius of the orbit of ACE around the L-1 point (Russell et al., 1980; Crooker et al., 1982; Kelly et al., 1986; Richardson and Paularena, 1998; Paularena et al., 1998; Collier et al., 1998). Therefore, when ACE is at a large distance from the Sun-Earth line, there is a significant reduction in the accuracy of space weather predictions based on the collected data. It has been argued that IMP-8 and WIND, when in the solar wind in front of the magnetosphere, are a reliable source of relevant space data. While this is often correct, the proximity of these spacecraft to Earth does not leave sufficient warning time for incoming events.

Triana would also provide a monitor of the solar wind in addition to any other spacecraft that may still be available at the time of its launch. This would allow the detailed study of the non-radial correlation with solar wind fluctuations. This study was begun with earlier spacecraft such as the Explorers, IMP, and ISEE, but new opportunities would now be available. For example, if WIND or a STEREO spacecraft were measuring the solar wind at a variety of positions away from L-1, this would provide correlation at multiple baselines. These measurements would help to determine the symmetry of the fluctuations in the wind that in turn determine the way in which energetic particles propagate in the heliosphere. This basic understanding is also central to determining how, for example, solar events affect the Earth and its near-space environment, and thus is important for determining the effects of solar activity on spacecraft and manned space flights.

The combination of ACE, Triana, WIND, and IMP-8, would provide the necessary four-point studies to investigate curvatures of shock and discontinuity surfaces. When the four spacecraft are separated by large distances (on the order of  $200 R_e$ ), we

can measure curvatures in relatively stable structures (e.g., magnetic clouds). We expect to observe curvatures in the heliospheric current sheet (Szabo et al., 1999). The four-spacecraft constellation would afford a unique opportunity to resolve the question of multi-layer heliospheric current sheets. Tracing the passage of a specific current sheet from one spacecraft to the next would allow discrimination between the general case of multiple current sheets or a single wavy sheet. A four spacecraft constellation would allow the determination of the size of typical magnetic holes.

### **5.3.3 Small-Scale Structures and High Time Resolution Measurements**

Very narrow regions in the interplanetary medium, with abrupt magnetic field strength decreased to nearly zero, have been observed for a long time (Burlaga and Ness, 1968; Burlaga, 1968), and have been termed magnetic holes by Turner et al. (1977). Two major classes of these magnetic holes have been distinguished: “D-sheets” associated with field rotations (Burlaga and Ness, 1968) and “linear” magnetic holes (Turner et al., 1977; Fitzenreiter and Burlaga, 1978). D-sheets are of particular interest since they might be the interplanetary signatures of reconnection events. Linear magnetic holes, on the other hand, are believed to be pressure-balanced structures. However, to date, no sufficiently high time resolution plasma data are available to study these structures. Magnetic holes near Earth, occurring a rate of about 1.5/day, move past a spacecraft in the time range of 2 to 130 seconds, the median time being 50 seconds. These phenomena would easily be observed by Triana/Plasma-Mag.

### **5.3.4 Tangential Discontinuities**

A discontinuity in which the magnetic field has no component normal to the discontinuity surface is called a tangential discontinuity. The kinetic theory of the internal structure of interplanetary tangential discontinuities has recently reached a level of maturity (DeKeyser and Roth , 1997) that allows meaningful comparison between theoretical predictions and in-situ observations without constraining all of the model parameters. In order to remove some of the theoretical ambiguities, very high time resolution plasma and magnetic field observations are necessary. The Plasma-Mag instrumentation will provide such a data set, significantly contributing to kinetic theory modeling efforts.

The high-time resolution plasma and magnetic field instruments onboard Triana will open a window into the inner structures of weak- and slow-interplanetary shocks, which should lead to a better understanding of their formation and dissipation mechanisms. Interplanetary shocks have been studied for a very long time. Even the internal structure of MHD shocks is comparatively well understood primarily from Earth bow-shock observations. However, very little is known about the structural variations due to the various types of MHD shock. The Earth's bow shock will provide Triana an excellent opportunity to study fast reverse strong MHD shocks. Interplanetary shocks may be too difficult to study from Triana, because their much greater speed past the spacecraft leaves too little time for reliable measurements.

## 6. Data Distribution

The Triana mission will be supported by a Ground Data System (GDS) to command and control the spacecraft and capture and disseminate the science and image data. An overview of the GDS is shown in Figure 33.

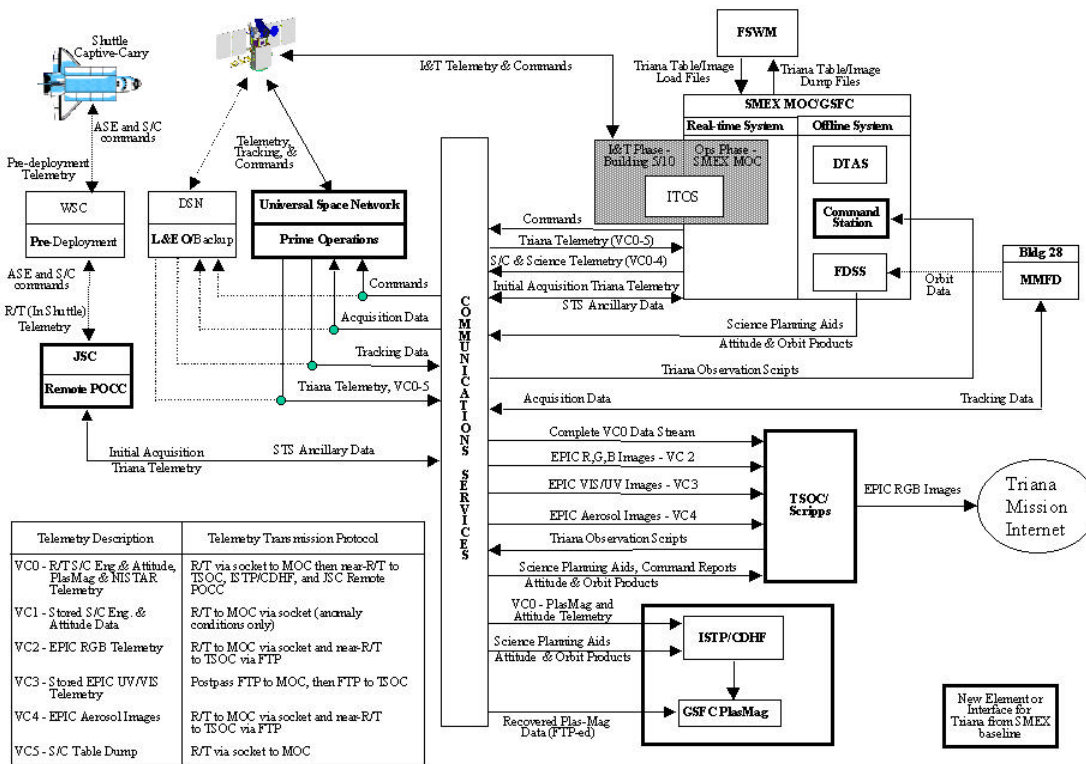


Figure 33 A schematic of the Triana Ground Data System architecture.

A globally distributed network of five to seven Remote Ground Stations (RGS), five prime and two backup, provides continuous contact with the Triana spacecraft and a continuous feed of telemetry and science/image data to the other ground elements. Each RGS views the Triana spacecraft for up to 8 hours. While in contact with the satellite, each RGS receives the 100-140 kbps downlink, and will then parse the data stream into at least three separate categories—1) spacecraft and instrument health and status data, 2) time-critical science and image data, and 3) non-time-critical science data. Both the Mission Operations Center (MOC) at GSFC and the Triana Science and Operations Center (TSOC) at Scripps receive satellite health and status.

The MOC will separate the time-critical Plasma-Mag instrument science data and forward it to the processing center at GSFC. This processed Plasma-Mag data will be sent to NOAA within minutes of receipt at GSFC. The remainder of the time-critical science/image data is immediately transmitted to the Scripps TSOC for processing and posting.

To minimize bandwidth requirements and therefore costs, the active RGS stores the non-time-critical science data and transmits this data set to the MOC once the Triana spacecraft is no longer in view of the RGS. The MOC transmits this stored science data to the TSOC for processing. While the post-contact transmission time is variable, depending on the time that the RGS was in contact with the satellite and the bandwidth available between the RGS and the MOC, in general the TSOC can expect to receive the stored science data less than sixteen hours after its collection.

The MOC operations crew is responsible for tracking and maintaining the health and status of the instruments and the spacecraft subsystems. The near-real-time telemetry data received from the RGS is processed at the MOC as it is received and displayed to the MOC operations crew. Should any parameters be observed to be out of prescribed limits, or any other anomalies seen on the data, the operations crew is responsible for implementing the appropriate approved corrective action plan. The MOC is also responsible for monitoring the telemetry to verify successful receipt of all uplinked commands. Commands destined for the three science instruments are based on “command scripts” sent to the MOC from the TSOC, nominally once per week. To support the TSOC’s generation of these scripts, the MOC provides spacecraft status and orbit data to the TSOC on a periodic basis.

At the TSOC, the time-critical science/image data and the delayed science data is received from the MOC and processed, posted, and stored. Figure 34 shows the functions that are taking place in the TSOC. Within the TSOC, there are two basic processing strings—science and image processing. The science processor will host the various algorithms that have been supplied by the Triana co-investigators. The NISTAR data will be processed and stored and a “ready for check” message will be sent to NIST. The NIST co-investigator will confirm that the data was collected properly and did not arrive during filter movement, spacecraft slew, or during an instrument calibration period. The TSOC controller will then mark the data as valid for science investigation.

The EPIC science data will be decompressed and have the current instrument calibration parameters applied. The data will be processed using the appropriate co-investigator supplied algorithm and then stored. The various co-investigators can then either use the TSOC facility for additional science analysis or request a download the pertinent portions of the science data for evaluation at their own facility.

The visible science channels (443, 551, and 645 nm) that are collected every fifteen minutes will be routed to the TSOC image product generator. Here the images will be geo-located, geo-registered, and then processed for posting on the Triana web site. With projected downlink and processing delays, the images will be posted approximately 30-45 minutes after being collected by the satellite.

The TSOC will store all the raw and processed science and image data for the life of the Triana mission plus three years. Raw and processed science and image data will be sent to a NASA data archive for long term storage.

To enhance the ability of Triana data products to inspire and to educate, the TSOC is located in the same UCSD facility as the EarthKAM Operations Center. EarthKAM is a NASA program hosted at UCSD and designed to engage the educational community in inquiry-based learning to conduct Earth Science research based on remotely-sensed data, including images taken by students with a camera in Earth orbit. The TSOC hardware and software designs have been selected for compatibility with EarthKAM operations and specific Triana educational web based products can be created and made available to the existing EarthKAM student and educator infrastructure.

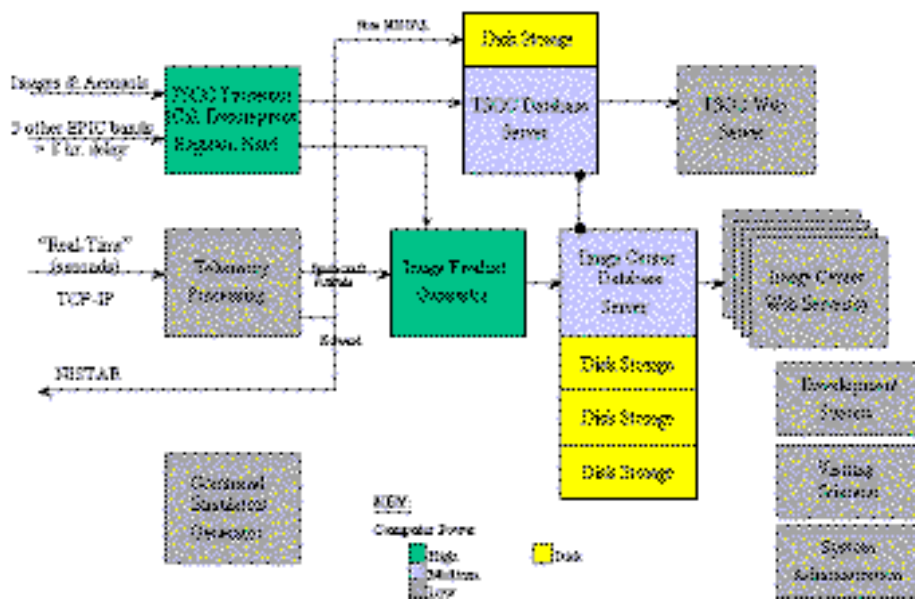


**Figure 34** A schematic of the Triana Science and Operations Center.

## **APPENDIX A: Scripps-EPIC**

### **I) Instrument Description**

The Scripps-Earth Polychromatic Imaging Camera (Scripps-EPIC) provides high resolution images of the Earth from the L-1 orbit. The camera consists of a Cassegrain telescope with a 12-inch aperture and a  $0.62^\circ$  field of view, mated to a 10-color filter-wheel assembly and shutter, followed by a 4 mega-pixel, UV-sensitive charge coupled device (CCD). Performance characteristics of EPIC are provided in Table A-1.

The 10 filters are contained in two filter wheels. The three shutter apertures provide nominal exposure times of 2 ms, 10 ms, and 40 ms or greater. Exposures of 40 ms or greater are obtained by varying the motor speed. Intermediate exposures (between 2 ms and 40 ms) are obtained by up to 8 multiple exposures of the 2- and 10-ms apertures. These multiple exposures can be made on a 100 ms cadence.

The focal plane is a 2048 x 2048 CCD, backside-thinned and backside-illuminated to optimize quantum efficiency down to 300 nm (modified LMFS-type CCD 442A). The CCD is passively cooled to  $-40^\circ\text{C}$  on orbit to reduce dark current and other noise effects.

Commands from the ground or as a result of on-board pre-planned sequences are sent to the EC to request images, initiate on-board image processing, or collect EPIC instrument status and housekeeping data. The EC includes sufficient on-board memory (320 MB) to store a large number of images in various stages of processing or compression. The flight software includes CCD flat-fielding, thresholding, region-of-interest selection, and the ISO-standard 12-bit JPEG compression algorithm as image processing options. Unprocessed raw CCD frames can also be provided for downlink. The number and type of images that can be sent to the ground are only limited for practical purposes by the Triana telemetry capacity and the amount of on-board image processing or compression.

**Table A-1: EPIC Performance Characteristics**

Telescope: Cassegrain, with adjustable secondary for on-orbit focus			
Aperture			12.00 inches
Effective focal length			111.1 inches
Field of view			0.62 degrees
Wavefront error			0.054 waves RMS at 633 nm on-axis
A 3-element field lens group provides off-axis corrections			
Filters:			
	Wavelength (nm)	Full Width (nm)	Purpose
	317	1	Ozone, SO <sub>2</sub>
	325	1	Ozone
	340	3	Aerosols
	388	3	Aerosols, Clouds
	393.5	1	Cloud Height
	443	10	Blue, Aerosols
	551	10	Green, Aerosols
	645	10	Red, Aerosols
	870	15	Clouds, Aerosols
	905	30	Water Vapor
Shutter:			
	Individual exposure times of 2 ms, 10 ms, and 40 ms to >1 minute		
	Multiple exposures for timings between 2 ms and 40 ms at 2 ms resolution		
Focal plane:			
CCD format	2048 x 2048 pixels		
Pixel size	15 microns x 15 microns, 100% fill factor		
CCD type	Thinned, backside illuminated		
Spectral range	200 - 950 nm (QE > 25%)		
Pixel full well depth	>80,000 electrons		
Digital intensity conversion	0 - 4095, 12 bits at 20 electrons per bit		
Readout	Single or dual (opposite corners)		
Pixel readout rate	500 kHz		
CCD operating temperature	-40°C, by passive cooling		
Dark current	<5 electrons per second per pixel		
Readout noise	<20 electrons RMS		
Minimum image cadence	>15 seconds		
Image output formats	Raw (bit map) and 12-bit JPEG/JFIF		
Instrument power (normal operations):			
Electronics	32 W		
Operational heaters	30 W		
Total	62 W		
Instrument mass:			
CTA	6.8 kg		
MEB	3.2 kg		
EC	55.0 kg		
Total	65.0 kg		

## II) Radiometric Calibration Before Launch

As of the time of preparation of this report, instrument assembly is not completed so that there are no results from end to end testing of the EPIC instrument. However, it is planned that there be extensive absolute radiometric calibration both at room temperature and in thermal and vacuum conditions. The latter is necessary because the CCD is expected to operate at L-1 at temperatures of about  $-40^{\circ}\text{C}$  under vacuum conditions, while the telescope and optics will operate at nearly room temperature. The sensitivity of the CCD is temperature dependent, especially at the UV wavelengths. Current relative sensitivity is expressed in terms of CCD quantum efficiency QE (shown in Figure A-1).

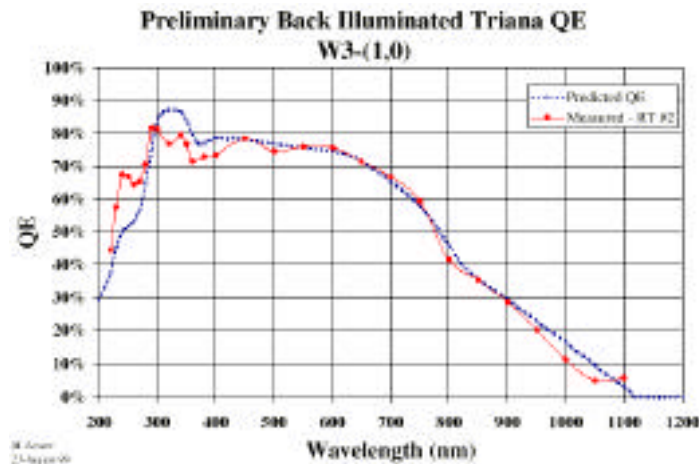


**Figure A-1** Quantum efficiency of the EPIC CCD vs. wavelength.

The product of the transmission of the telescope, filters, and fractional QE of the CCD essentially determine the sensitivity of the EPIC spectroradiometer system. The next figure of importance is the signal to noise ratio SNR of EPIC. This is determined by the CCD's electron well depth which is equal to 120,000 electrons. If the exposure is adjusted to fill the well to 90%, then the SNR is the square root of the number of electrons, or about 330:1, or about an accuracy of about 0.3%. As determined by the design specifications, the system is supposed to achieve 200:1, or about 0.5% accuracy. The accuracy as stated applies to the brightest scenes over the clouds, with reduced accuracy over dark regions (e.g., clear-sky scenes over oceans). When needed, the accuracy can be increased by combining scenes. That is, if 4 scenes are combined, the accuracy is doubled at the expense of halving the spatial resolution to 16 km.

The radiometric calibration will consist of determining the sensitivity of each of the 2048 x 2048 CCD elements using NIST calibrated lamps to illuminate a spherical

cavity producing a uniform light field over the entrance aperture of the telescope. Once the radiometric calibration is accomplished, it is necessary to determine any change in end to end sensitivity while EPIC is in flight. For this purpose, views of the Moon will be used to calibrate EPIC.

### III) In-Flight Calibration Using the Moon

One day per month will be set aside for calibration of EPIC and NISTAR. Most of this time will be devoted to EPIC as described here. The EPIC spectrometer will take a series of images (about 50) with the Moon positioned near the center of the CCD. Each image will be displaced a few CCD pixels from the previous image. The displacements are caused by lunar orbital motion between exposures (about 15 seconds apart) and by spacecraft jitter (~10 pixels in 15 seconds). After the central portion of the CCD is characterized with the first 50 exposures, another 50 will be obtained distributed over the entire CCD to relate fully the sensitivity of one pixel to another (flat fielding). This procedure must be repeated for each filter position.

In subsequent months the procedure will be repeated and examined for changes in each pixel and for drifts in groups of pixels. Over time an end to end transmission and sensitivity history will be built for each wavelength band. The result can be interpolated to produce a continuous daily change in calibration during the operation of EPIC. Figures A-2 and A-3 show the geometry of the Moon-spacecraft system and the placement of the lunar images on the CCD during the calibration.

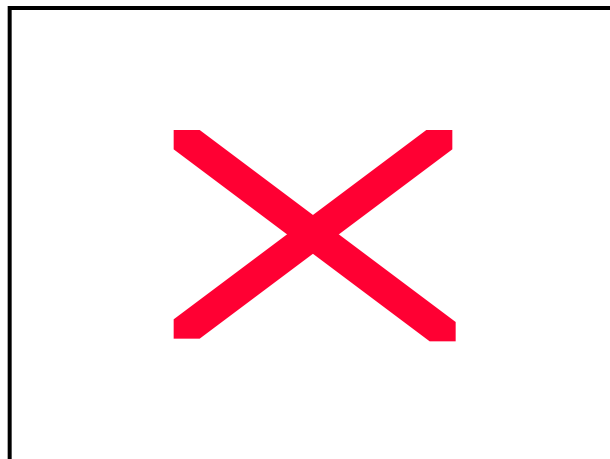


**Figure A-2** Lunar geometry during EPIC calibration.

The case shown in Figures A-2 and A-3 is for the minimum number of lunar images needed to produce useful results. The planned number of images per filter is larger. It is expected that the acquisition of the images and their transmission to the ground will take about 8 hours. The limiting factors are the transmission rate of images to the ground and the finite amount of onboard memory for storing images. The algorithm involves a time

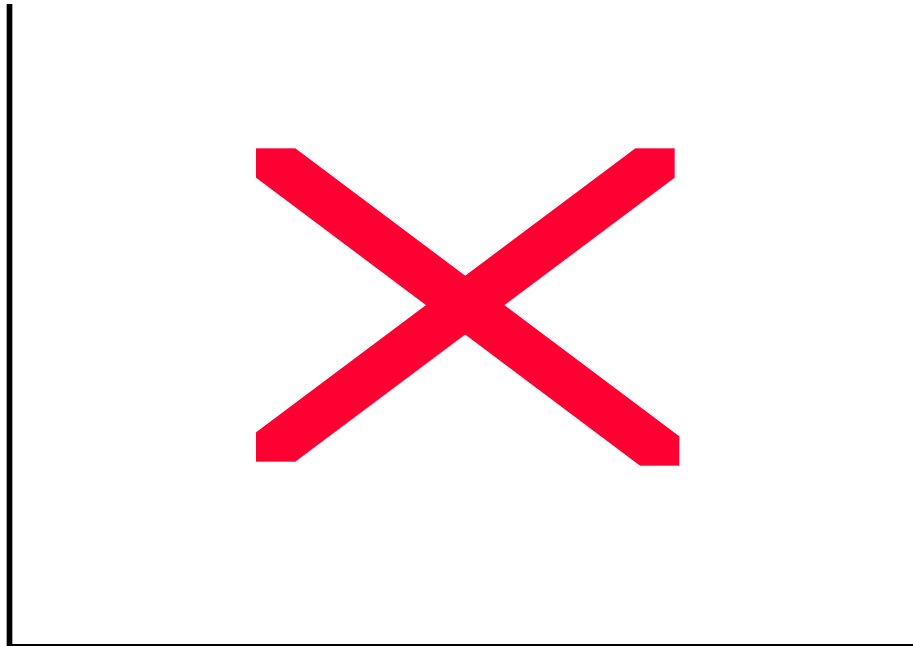


**Figure A-3** Flat fielding of the EPIC 2048x2048 CCD.

consuming solution of optimal minimization of least squares to an over-determined system of equations. The solution for all 10 wavelengths will take 1 to 2 days on the planned Sun or Silicon Graphics workstations.

## **APPENDIX B: Scripps-NISTAR**

Active cavity radiometers (ACRs) have been used for years to measure solar radiation and Earth radiation from low Earth orbit. NISTAR is a low-noise, near room-temperature ACR that will provide unprecedented sensitivity in a space qualified instrument. The key features that enable low noise and drift are: high-sensitivity positive temperature coefficient (PTC) thermistors for low-noise high-gain temperature control, digital servo loops employing a drop-floor algorithm for the most efficient use of measurement time, and AC-bridge based measurement electronics that provide sub-ppm resolution, all coupled to a low-mass, low-conductance receiver cavity design. A prototype radiometer was recently reported (Rice et al., 1999) at NIST and used to demonstrate the feasibility of measuring a microwatt signal with a signal-to-noise ratio of 100:1 or better with an ambient temperature instrument.

### **I) Design**

Orbiting the L-1 point aboard Triana, the  $\sim 0.5^\circ$  full Earth disk will be within the  $1^\circ$  full-angle field of view of NISTAR. NISTAR consists of four channels, three electrical substitution radiometers and a silicon photodiode detector, that will make continuous measurements of the sunlit Earth disk. The three radiometers will be used to make simultaneous measurements in three bands. Band-A is unfiltered and therefore measures the total radiant flux coming from the Earth both emitted and reflected across all wavelengths. The radiometer is spectrally flat with very broadband response that ranges from below 200 nm to beyond 100  $\mu\text{m}$ . Band-B is the solar channel and employs a water-free quartz filter that transmits from 200 nm to 4  $\mu\text{m}$ . By cutting off radiation above 4  $\mu\text{m}$  the thermal emission from the Earth is blocked. Band-C is a near-infrared channel defined by a filter that transmits from 720 nm to 4  $\mu\text{m}$ . This spectral range represents approximately half of the reflected energy from the Sun, separating the UV-VIS from the near and shortwave IR solar reflected radiation. The filters are mounted in a 12-position wheel with redundant filters for Bands B and C thereby allowing monitoring of filter degradation during the lifetime of the mission.

A silicon photodiode detector based radiometer channel has been included in the instrument in order to obtain a faster time series ( $< 1$  second) than what can be obtained by the radiometers. This channel provides for a number of measurements such as tracking the stability of the filters, verifying the co-alignment of NISTAR with EPIC, and providing a continuous broadband measurement of the solar reflected radiation from the

Earth with high temporal resolution. The spectral response of the photodiode channel is 190 nm to 1100 nm.

## II) Principle of Operation of the ACRs

A PTC thermistor and a wire-wound low-temperature coefficient heater are bonded to the outside of the 30° conical receiver cavity. The PTC thermistors are polycrystalline barium strontium titanate with dopants added to make them semiconductors. A sharp rise in the resistance  $R$  with increasing temperature  $T$  occurs above the Curie temperature associated with a ferroelectric phase transition. This results in  $dR/dT$  values of up to 1000  $\Omega/K$  with an operating resistance of only 10 k  $\Omega$ .

By careful tradeoff between several critical parameters, the NISTAR ACRs were designed for optimum power measurements in the tens of microwatt range. The optical signal incident on the receiver is only 1  $\mu W cm^{-2}$ , however the emission from the receiver cavity to space is estimated to be 30  $\mu W cm^{-2}$  when the shutter is open.

There are four digital control loops, three receiver cavity control loops and one for the heat sink. The PTC temperature sensor resistance measurements are performed with AC-Bridge circuits operating between 35 and 155 Hz. The AC-Bridge circuit enables the measurement to take place in a very narrow bandwidth about the excitation current frequency, effectively rejecting noise at all other frequencies. This low-noise arrangement is able to measure resistors such as the PTC thermistor at noise levels comparable to the intrinsic thermistor Johnson noise. The NISTAR AC-bridge circuit has been designed to have a full scale of 20k  $\Omega$  with a resolution of 0.010  $\Omega$  or 0.5 ppm.

The PID digital control loops are realized in software where the error signal from the AC-bridge is used to control a DAC driving the heater circuit for each device. An A/D converter measures the voltage across the receiver heater. The measured electrical power is derived from the square of this voltage divided by the known resistance of the receiver heater. The NISTAR electronics have both a circuit to apply power and an independent circuit to measure the voltage drop across the heater, thereby improving the reliability of the measurement. The time series of this electrical power during shutter cycles is used to deduce the optical power. The measured irradiance is then determined by dividing the measured optical power by the measured area of the precision aperture mounted in front of the receiver cavity.

### **III) Drop Floor Algorithm**

A very simple feed-forward technique taken from control theory, which we refer to as a drop-floor algorithm, was chosen to reduce the time for the receiver to return to equilibrium after a shutter motion. Since the radiant power received from the Earth is a slowly varying signal, the values measured during the last shutter cycle are a good starting point, or guess, for the servo to start from. The prior integrator value is stored for the two cases of shutter open and closed, then as the shutter begins its motion the current integrator value is frozen then transitioned to the prior value in a manner that is proportional to the instantaneous aperture area that is exposed. This forces the heater power to increase or decrease in proportion to the shutter motion, thereby minimizing any temperature disturbance in the receiver. Hence, the loop is always controlling at its optimum noise performance.

### **IV) Characterization and Calibration**

The quantities and their uncertainties that dominate the beginning of mission absolute scale for NISTAR are as follows: responsivity of the receiver cavities, aperture area, filter transmission, and temperature dependence of the electronics. This is a partial list of the parameters that will be determined during the calibration and characterization of NISTAR at NIST.

A number of on-orbit checks will be routinely performed to check the stability and degradation of the instrument with time: 1) routine look at deep space to check the 'zero' of the instrument, 2) measurements of solar reflected radiation from the Moon, 3) intercomparisons with redundant filters to track the filter degradation, and 4) cross checks between the different channels to look at relative drifts.

A calibration chamber has been developed that will allow complete operational testing of the NISTAR instrument before integration to the Triana spacecraft. The chamber is equipped with a liquid nitrogen shroud, temperature controlled interface/support plate, and four Brewster windows. This will allow the instrument to be temperature cycled throughout its operational range in a low-background environment. An important part of the characterization effort is to determine the end-to-end operational parameters for the flight electronics as a function temperature. The four Brewster windows will allow optical access to the radiometer channels using a polarized laser beam. A complete optical setup including a laser power stabilizer and an optical-trap

detector standard has also been developed. The arrangement produces a collimated light source with known power (0.03%) that is stable to 10 ppm/hour. This will allow optical power measurements that are directly traceable to the national standards.

#### **V) NISTAR Performance**

The NISTAR ACRs were designed to have a noise floor of less than 10 nW, defined here to be the level at which the signal to noise is equal to one for a single 1 second measurement. The NISTAR electronics have a measurement resolution of 10 m and internal equivalent noise of less than that. Tests with the flight electronics have yielded results of 7 m for measurements of a 10K resistor. To date the complete flight instrument has not been tested under cryogenic vacuum test conditions since the flight electronics have yet to be completed. However, tests using commercially available electronics with a similar prototype radiometer to those used in NISTAR have produced results approaching 10 nW. The prognosis for achieving the science goals of the mission is excellent based on the preliminary results to date.

## APPENDIX C: References

Austin, J., N. Butchart, and K.P. Shine, Possibility of an Arctic ozone hole in a doubled-CO<sub>2</sub> climate, *Nature*, 360, 221-225, 1992.

Battisti, D.S., C.M. Bitz, and R.E. Moritz, Do general circulation models underestimate the natural variability in the Arctic climate? *Journal of Climate*, 10, 1909-1920, 1997.

Bonan, G.B., A land surface model (LSM version 1.0) for ecological, hydrological, and atmospheric studies: Technical description and user's guide, National Center for Atmospheric Research technical note NCAR/TN-417+STR (NCAR, P.O. Box 3000, Boulder, CO. 80307), 150 pp., 1996.

Bonan, G.B., The land surface climatology of the NCAR Land Surface Model coupled to the NCAR Community Climate Model, *J. Climate*, 11: 1307-1326, 1998.

Bornman, J.F., and A.H. Teramura, Effects of ultraviolet-B radiation on terrestrial plants, in *Environmental UV Photobiology*, edited by A. R. Young et al., Plenum Press, New York, 427-471, 1993.

Burlaga, L.F. and N.F. Ness, Macro- and microstructure of the interplanetary magnetic field, *Can. J. Phys.*, 46, S962, 1968.

Burlaga, L.F., Micro-Scale structures in the interplanetary medium, *Solar Phys.*, 4, 67, 1968.

Cavalieri, D.J., P. Gloersen, C.L. Parkinson, J.C. Comiso, and H.J. Zwally, Observed hemispheric asymmetry in global sea ice changes, *Science*, 278, 1104-1106, 1997.

Chen, B., D.H. Bromwich, K.M. Hines, and X. Pan, Simulations of the 1979-1988 polar climates by global climate models, *Annals of Glaciology*, 21, 83-90, 1995.

Collier, M.R., J.A. Slaven, R.P. Lepping, A. Szabo, and K. Ogilvie, Timing accuracy for the simple planar propagation of magnetic field structures in the solar wind, *Geophys. Res. Lett.*, 25, 2509-2512, 1998.

Collins, W.D., A global signature of enhanced shortwave absorption by clouds. *J Geophys. Res.*, 103, 31669-31679, 1998.

Correll, D.L., C.O. Clark, B. Goldberg, V.R. Goodrich, D.R. Hayes Jr., W.H. Klein, and W.D. Schecher, Spectral ultraviolet-B radiation fluxes at the earth's surface; long-term variations at 39 degrees North, 77 degrees West, *J. Geophys. Res.*, 97, 7579-7591, 1992.

Crooker, N.U., G.L. Siscoe, C.T. Russell, and E.J. Smith, Factors controlling degree of correlation between ISEE 1 and ISEE 3 interplanetary magnetic field measurements, *J. Geophys. Res.*, 87, 2224-2230, 1982.

Curry, J.A., and E.E. Ebert, Annual cycle of radiation fluxes over the Arctic Ocean: Sensitivity to cloud optical properties, *Journal of Climate*, 5, 1267-1279, 1992.

Curry, J.A., and G.F. Herman, Relationship between large-scale heat and moisture budgets and the occurrence of Arctic stratus clouds, *Monthly Weather Review*, 113, 1441-1457, 1985.

Curry, J.A., W.B. Rossow, D. Randall, and J.L. Schramm, Overview of Arctic cloud and radiation characteristics, *Journal of Climate*, 9, 1731-1764, 1996.

Curry, J.A., and P.J. Webster, *Thermodynamics of Atmospheres and Oceans*, Academic Press, San Diego, 471 pp., 1999.

Dave, J.V., Multiple scattering in a non-homogeneous, Rayleigh atmosphere, *J. Atmos. Sci.*, 22, 273- 279, 1965.

De Gruijl, F.R., and J.C. Van der Leun, Influence of ozone depletion on the incidence of skin cancer: quantitative prediction, in *Environmental UV Photobiology*, edited by A. R. Young et al., Plenum Press, New York, 89-112, 1993.

DeKeyser, J. and M. Roth, Equilibrium conditions for the tangential discontinuity magnetopause, *J. Geophys. Res.*, 102, 9513-9530, 1997.

DriscHEL, D., and R. Saravanan, Three-dimensional quasi-geostrophic contour dynamics, with an application to stratospheric vortex dynamics, *Q. J. R. Meteorol. Soc.*, 120, 1267-1297, 1994.

Ebert, E., A pattern recognition technique for distinguishing surface and cloud types in the polar regions, *Journal of Climate and Applied Meteorology*, 26, 1412-1427, 1987.

Farquhar, R.W., Preliminary considerations for establishment of a satellite in the neighborhood of centers of libration, M.S. Thesis, Univ. Calif. Los Angeles, Engineering, 1960.

Farquhar, R.W., The control and use of libration-point satellites, PhD. Thesis, Stanford University, Dept. of Astronautics and Aeronautics, 1968.

Fels, S.B., J.D. Mahlman, M.D. Schwarzkopf, and R.W. Sinclair, Stratospheric sensitivity to perturbations in ozone and carbon dioxide radiative and dynamical response, *J. Atmos. Sci.*, 37, 2265-2297, 1980.

Fitzenreiter, R.J. and L.F. Burlaga, Structure of current sheets in magnetic holes at 1AU, *J. Geophys. Res.*, **83**, 5579, 1978.

Francis, P.N, J.P. Taylor, P. Hignett, and A. Slingo, On the question of enhanced absorption of solar radiation by clouds, *Q. J. R. Meteorol. Soc.*, 123: 419-434, 1997.

Gerstl, S.A.W., and C. Simmer, Radiation physics and modeling for off-nadir satellite sensing of non-Lambertian surfaces, *Remote Sensing of Environment*, 20; 1-29, 1986.

Gerstl, S.A.W., Angular Reflectance Signature of the Canopy Hotspot in the Optical Regime, 4<sup>th</sup> Intl. Coll. On Spectral Signatures of Objects in Remote Sensing, Aussois, France, ESA report SP-287, 129, 1988.

Gerstl, S.A.W., Building a Global Hotspot Ecology with Triana Data, Proc. EOS/SPIE Symp. on Remote Sensing, Ecosystems and Hydrology III, Remote Sensing for Agriculture, Univ. of Florence, Italy, 20 - 24 Sept. 1999.

Green, A., and G. Williams, Ultraviolet radiation and skin cancer: epidemiological data from Australia, in *Environmental UV Photobiology*, edited by A. R. Young et al., Plenum Press, New York, 233-254, 1993.

Herlihy, E., P.H. Gies, C.R. Roy, and M. Jones, Personal dosimetry of solar UV radiation for different outdoor activities, *Photochemistry and Photobiology*, 60, 288-294, 1994.

Herman, J.R., R.D. McPeters, and D. Larko, Ozone depletion at northern and southern latitudes derived from January 1979 to December 1991 Total Ozone Mapping Spectrometer data, *J. Geophys. Res.* **98**, 12783-12793, 1993.

Herman, B.M., T.R. Caudill, D.E. Flittner, K.J. Thome, and A. Ben-David, Comparison of the Gauss-Seidel spherical polarized radiative transfer code with other radiative transfer codes, *Appl. Opt.*, **34**, 4563-4572, 1996.

Herman, J.R. and E.A. Celarier, Earth surface reflectivity climatology at 340 nm to 380 nm from TOMS data, *J. Geophys. Res.* **102**, 28003-28011, 1997.

Herman, J.R., P.K. Bhartia, O. Torres, C. Hsu, C. Seftor, and E. Celarier, Global distribution of UV-absorbing aerosols from Nimbus-7/TOMS data, *J. Geophys. Res.*, **102**, 16,911-16, 922, 1997.

Herman, J.R., D. Larko, and J. Ziemke, Regional changes in global UV reflectivity from clouds and aerosols, accepted by *J. Geophys. Res.*, 1999a.

Herman, J.R., N. Krotkov, E. Celarier, D. Larko, and G. Labow, The distribution of UV radiation at the Earth's surface from TOMS measured UV-backscattered radiances, *J. Geophys. Res.* 104, 12059-12076, 1999b.

Hoskins, B.J., M.E. McIntyre, and A.W. Robertson, On the use and significance of isentropic potential vorticity maps, *Q. J. R. Meteorol. Soc.*, **111**, 877-946, 1985.

Hsu, N. Christina, J.R. Herman, and Clark Weaver, Determination of radiative forcing of Saharan dust using combined TOMS and ERBE data, submitted to *J. Geophys. Res.*, 1999a.

Hsu, N. Christina, Jay R. Herman, O.Torres, B.N. Holben, D. Tanre, T.F. Eck, A.Smirnov, B. Chatenet, and F. Lavenu, Comparisons of the TOMS aerosol index with sun photometer aerosol optical thickness, *J. Geophys. Res.* 104, 6269-6279, 1999b.

Hsu, N.C., J.R. Herman, J.F. Gleason, O. Torres., and C.J. Seftor, Satellite detection of smoke aerosols over a snow/ice surface by TOMS, *Geophys. Res. Lett.*, 26, 1165-1168, 1999c.

Hsu, N.C., J.R. Herman, P.K. Bhartia, C.J. Seftor, A.M. Thompson, J.F. Gleason, T.F. Eck, and B.N. Holben, Detection of biomass burning smoke from TOMS measurements, *Geophys. Res. Letts.*, **23**, 745-748, 1996.

Kalliskota, S., J. Kaurola, P. Taalas, J.R. Herman, E. Celarier, and N. Krotkov, Comparison of daily UV doses estimated from Nimbus-7/TOMS measurements and ground-based spectroradiometric data, accepted, *J. Geophys. Res.*, 1999.

Kaufman, Y.J., and B. Gao, Remote sensing of water vapor in the near IR from EOS/MODIS, *IEEE Transactions Geoscience Remote Sensing*, 30, 871-884, 1992.

Kelly, T.J., N.U. Crooker, G.L. Siscoe, C.T. Russell, E.J. Smith, On the use of sunward libration-point-orbiting spacecraft as an interplanetary magnetic field monitor for magnetospheric studies, *J. Geophys. Res.*, 91, 5629-5636, 1986.

Kiehl, J.T., and B.P. Briegleb, The relative roles of sulfate aerosols and greenhouse gases in climate forcing, *Science*, 260, 311-314, 1993.

Krotkov, N.A., P.K. Bhartia, J.R. Herman, V. Fioletov, and J. Kerr, Satellite estimation of spectral surface UV irradiance in the presence of tropospheric aerosols 1: Cloud free case, *J. Geophys. Res.*, **103**, 8779-8793, 1998.

Krotkov, N., J.R. Herman, P.K. Bhartia, Z. Ahmad, and V. Fioletov, Satellite estimation of spectral surface UV irradiance 2: Effect of horizontally homogeneous clouds, submitted to *J. Geophys. Res.*, 1999.

Kyle, H.L., R. Hucek, P. Ardanuy, L. Penn, J. Hickey, and B. Groveman, In-flight calibration of the Nimbus-7 Earth radiation budget (ERB) sensors. 3. Long Term Changes., *J. Atmos. Oceanic Tech.*, 12: 1163-1176, 1995.

Lubin, D., and E. Morrow, Evaluation of an AVHRR cloud detection and classification method over the central Arctic Ocean, *Journal of Applied Meteorology*, 37, 166-183, 1998.

Lubin, D., E.H. Jensen, and H.P. Gies, Global surface ultraviolet radiation climatology from TOMS and ERBE data, *J. Geophys. Res.*, 103, 26,061-26,091, 1998.

McKenna, D.S., R.L. Jones, J. Austin, E.V. Browell, M.P. McCormick, A.J. Krueger, and A.F. Tuck, Diagnostic studies of the Antarctic vortex during the 1987 Airborne Antarctic Ozone Experiment: Ozone Miniholes, *J. Geophys. Res.*, 94, 11641-11668, 1989.

Minnis, P., and E.F. Harrison, Diurnal variability of regional cloud and clear-sky radiative parameters derived from GOES data, Part I: analysis method, *J. Climate Applied Meteorology*, 23, 993-1011, 1984.

Minnis, P., P.W. Heck, and D.F. Young, Inference of cirrus cloud properties using satellite-observed visible and infrared radiances, Part II: Verification of theoretical cirrus radiative properties, *J. Atmos. Sci.*, 50, 1305-1322, 1993.

Minnis, P., and W.L. Smith, Jr., Cloud and radiative fields derived from GOES-8 During SUCCESS and the ARM-UAV Spring 1996 Flight Series, *Geophys. Res. Lett.*, 25, 1113-1116, 1998.

Minnis, P., D.P. Garber, D.F. Young, R.F. Arduini, and Y. Takano, Parameterization of reflectance and effective emittance for satellite remote sensing of cloud properties, *J. Atmos. Sci.*, 55, 3313-3339, 1998.

Moan, J., and A. Dahlback, Ultraviolet radiation and skin cancer: epidemiological data from Scandinavia, in *Environmental UV Photobiology*, edited by A. R. Young et al., Plenum Press, New York, 255-293, 1993.

Müller, R., P.J. Crutzen, J.-U. Groos, C. Brühl, J.M. Russell III, H. Gernandt, D.S. McKenna, and A.F. Tuck, Severe chemical ozone loss in the Arctic during the winter of 1995-96, *Nature*, 389, 709-712, 1997.

Nguyen, L., P. Minnis, J.K. Ayers, W.L. Smith, Jr., and S.P. Ho, Intercalibration of geostationary and polar satellite data using AVHRR, VIRS, and ATSR-2 data, *Proc. AMS 10th Conf. Atmos. Rad.*, Madison, WI, June 28 - July 2, 1999.

Paularena, K.I., G.N. Zastenker, A.J. Lazarus, and P.A. Dalin, Solar wind plasma correlations between IMP-8, INTERBALL-1 and WIND, *J. Geophys. Res.*, 103, 14601-14617, 1998.

Pilewskie, P., and F.P.J. Valero, Optical depths and haze particle sizes during AGASP III, *Atmos. Env.*, 27A, no. 17/18, 2895-2899, 1993.

Pinto, J.O., Autumnal mixed-phase cloudy boundary layers in the Arctic, *J. Atmos. Sci.*, 55, 2016-2038, 1998.

Platnick, S., and S. Twomey, Determining the susceptibility of cloud albedo to changes in droplet concentration with the Advanced Very High Resolution Radiometer, *Journal of Applied Meteorology*, 33, 334-347, 1994.

Polissar, A.V., P.K. Hopke, W.C. Malm, and J.F. Sisler, Atmospheric aerosol over Alaska: I. Spatial and seasonal variability, *J. Geophys. Res.*, 103, 19,035-19,044, 1998.

Rice, J.P., S.R. Lorentz, and T.M. Jung, The Next Generation of Active Cavity Radiometers for Space-Based Remote Sensing, Proceedings of the 10<sup>th</sup> American Meteorological Society, 85-88, 1999.

Richardson, J.D., and K.I. Paularena, The orientation of plasma structure in the solar wind, *Geophys. Res. Lett.*, 25, 2097-2100, 1998.

Russell, C.T., G.L. Siscoe, and E.J. Smith, Comparison of ISEE 1 and ISEE 3 interplanetary magnetic field observations, *Geophys. Res. Lett.*, 7, 381-384, 1980.

Salby, M.L., and P.F. Callaghan, Fluctuations of total ozone and their relationship to stratospheric air motions. *J. Geophys. Res.*, 98, 2715-2727, 1993.

Serreze, M.C., R.G. Barry, and J.E. Walsh, Atmospheric water vapor characteristics at 70 degrees North, *Journal of Climate*, 8, 719-731, 1995.

Shaw, G.E., Atmospheric turbidity in the polar regions, *Journal of Applied Meteorology*, 21, 1080-1088, 1982.

Shindell, D.T., D. Rind, and P. Lonergan, Increased polar stratospheric ozone losses and delayed eventual recovery owing to increasing greenhouse-gas concentrations, *Nature*, 392, 589-592, 1998.

Smith, G.L., Simulation of full Earth disc measurement at L-1 of reflected solar radiation, 5<sup>th</sup> Conference on Sensors, Systems and Next Generation Satellites, EOS/SPIE Symposium, University of Florence, 20-24 Sept. 1999.

Solomon, S., Stratospheric ozone depletion: A review of concepts and history, *Reviews of Geophysics*, 37, 275-316, 1999.

Stamnes, K., R.G. Ellingson, J.A. Curry, J.E. Walsh, and B.D. Zak, Review of science issues, deployment strategy, and status for the ARM North Slope of Alaska - Adjacent Arctic Ocean Climate Research Site, *Journal of Climate*, 12, 46-63, 1999.

Stephens, G.L., and S.-C. Tsay, On the cloud absorption anomaly, *Q.J.R. Meteorol. Soc.*, 116(493): 671-704, 1990.

Stone, R.S., Variations in western Arctic temperatures in response to cloud radiative and synoptic-scale features, *J. Geophys. Res.*, 102, 21,769-21,776, 1997.

Sun-Mack, S.Y., Y. Chen, T.D. Murray, P.Minnis, and D.F. Young, Visible clear-sky and near-infrared surface albedos derived from VIRS for CERES. *Proc. AMS 10<sup>th</sup> Conf. Atmos. Rad.*, Madison, WI, June 28 – July 2, 422-425, 1999.

Suttles, J.T., R.N. Green, P.Minnis, G.L. Smith, W.F. Staylor, B.A. Wielicki, I.J. Walker, D.F. Young, V.R. Taylor, and L.L. Stowe, Angular Radiation Models for Earth-Atmosphere System: Volume – Shortwave Radiation. *NASA RP 1184 Vol. I*, 84 pp., 1988.

Suttles, J.T., R.N. Green, G.L. Smith, B.A. Wielicki, I.J. Walker, V.R. Taylor, and L.L. Stowe, Angular Radiation Models for Earth-Atmosphere System: Volume II – Longwave Radiation. *NASA RP 1184 Vol. II*, 144 pp., 1989.

Szabo, A., R. P. Lepping, and D. E. Larson, Crossing the Heliospheric Current Sheet, in "Interball in the ISTP Program", pp. 231-237, eds. D. G. Sibeck and K. Kudela, NATO ASI Series, Kluwer Academic, Netherlands, 1999.

Tashima, D.H., and D.L. Hartmann, Regional trends in Nimbus-7 OLR: Effects of a spectrally nonuniform albedo, *Journal of Climate*, 12, 1458-1466, 1999.

Teitelbaum, H., and R. Sadourny, The role of planetary waves in the formation of polar stratospheric clouds. *Tellus*, 50A, 302-312, 1998.

Teitelbaum, H., M. Moustououi, P.F.J. Van Velthoven, and H. Kelder, Decrease of total ozone at low latitudes in the southern hemisphere by a combination of linear and nonlinear processes, *Q. J. R. Meteorol. Soc.*, 124, 2625-2644, 1998.

Teramura, A.H., J.H. Sullivan, and L.H. Liska, Interaction of elevated UV-B radiation and CO<sub>2</sub> on productivity and photosynthetic characteristics in wheat, rice, and soybean, *Plant Physiology*, 94, 470-475, 1990.

Torres, O., J.R. Herman, P.K. Bhartia, and Z. Ahmad, Properties of Mt. Pinatubo aerosols as derived from Nimbus-7 TOMS measurements, *J. Geophys. Res.*, 100, 14043-14055, 1995.

Torres, O., P.K. Bhartia, J.R. Herman, and Z. Ahmad, Derivation of aerosol properties from satellite measurements of backscattered ultraviolet radiation. Theoretical basis, *J. Geophys. Res.*, 103, 17099-17110, 1998.

Trepte, Q., Y. Chen, S. Sun-Mack, P. Minnis, D.F. Young, B.A. Baum, and P.W. Heck, Scene identification for the CERES cloud analysis subsystem. *Proc. AMS 10<sup>th</sup> Conf. Atmos. Rad.*, Madison, WI, June 28-July 2, 169-172, 1999.

Tsay, S.-C., K. Stamnes, and K. Jayaweera, Radiative energy budget in the cloudy and hazy Arctic, *J. Atmos. Sci.*, 46, 1002-1018, 1989.

Turner, J.M., L.F. Burlaga, N.F. Ness, and J.F. Lamaille, Magnetic holes in the solar wind, *J. Geophys. Res.*, 82, 1921-1924, 1977.

UNEP, Environmental Effects of Ozone Depletion: 1991 Update. United Nations Environmental Programme Panel Report Pursuant to Article 6 of the Montreal Protocol on Substances that Deplete the Ozone Layer, UNEP, P.O. Box 30552, Nairobi, Kenya. Also available from the U.S. Environmental Protection Agency, Washington, D.C., 1991.

Valero, F.P.J., T.P. Ackerman, and W.J.Y. Gore, The absorption of solar radiation by the Arctic atmosphere during the haze season and its effects on the radiation balance, *Geophys. Res. Lett.*, 11, 465, 1984.

Valero, F.P.J., T.P. Ackerman, W.J.Y. Gore and M.L. Weil, Radiation Studies in the Arctic, in *Aerosols and Climate*, A. Deepak, Hampton, Va., 1988.

Valero, F.P.J., R.D. Cess, M. Zhang, S.K. Pope, A. Bucholtz, B. Bush, and J. Vitko, Absorption of solar radiation by clouds: Interpretation of collocated aircraft measurements, *J. Geophys. Res.*, 102, 29,917-29,927, 1997.

Valero, F.P.J., P. Minnis, S.K. Pope, A. Bucholtz, B.C. Bush, D.R. Doelling, W.L. Smith, Jr., and Xiquan Dong, The absorption of solar radiation by the atmosphere as determined using satellite, aircraft, and surface data during the ARM Enhanced Shortwave Experiment (ARESE), accepted, *J. Geophys. Res.*, 1999.

Waugh, D.W., R.A. Plumb, R.J. Atkinson, M.R. Schoeberl, L.R. Lait, P.A. Newman, M. Loewenstein, D.W. Toohey, L.M. Avallone, C.R. Webster, and R.D. May, Transport out of the lower stratospheric Arctic vortex by Rossby wave breaking, *J. Geophys. Res.*, 99, 1071-1088, 1994.

Weiler, C.S., and P.A. Penhale (editors), *Ultraviolet Radiation in Antarctica: Measurements and Biological Effects*, American Geophysical Union Antarctic Research Series, Volume 62, American Geophysical Union, Washington, D.C., 257 pp., 1994.

Zerefos, C.S., D.S. Balis, A.F. Bais, D. Gillotay, P.C. Simon, B. Mayer, and G. Seckmeyer, Variability of UV-B at four stations in Europe, *Geophys. Res. Lett.*, 24, 1363-1366, 1997.

Zigman, S., Ocular damage by environmental radiant energy and its prevention, in *Environmental UV Photobiology*, edited by A. R. Young et al., Plenum Press, New York, 149-183, 1993.

## **APPENDIX D: Acronyms**

ACE	Advanced Composition Explorer
ACR	Active Cavity Radiometer
ADM	Angular Dependence Model
AERONET	Aerosol Robotic Network
AI	Aerosol Index
ARESE	ARM Enhanced Shortwave Experiment
ARM	Atmospheric Radiation Measurement program
ATSR-2	Along Track Scanning Radiometer
AVHRR	Advanced Very High Resolution Radiometer
AVIRIS	Airborne Visible Infrared Imaging Spectrometer
BRDF	Bi-directional Reflectance Distribution Function
CART	Clouds and Radiation Testbed
CCD	Charge Coupled Device
CCM3	Community Climate Model
CERES	Clouds and Earth's Radiant Energy System
CME	Coronal Mass Ejection
DAAC	Distributed Active Archive Center
DOE	U.S. Department of Energy
EarthKAM	Earth Knowledge Acquired by Middle school students
EC	EPIC Controller
ECMWF	European Center for Medium-range Weather Forecasting
ENSO	El Nino / Southern Oscillation
ENVISAT	European Space Agency Environmental Satellite
EOS	Earth Observing System
EP	Earth Probe
EPA	U.S. Environmental Protection Agency
EPV	Ertel Potential Vorticity
EPIC	Scripps-Earth Polychromatic Imaging Camera

ERB	Earth Radiation Budget
ERBE	Earth Radiation Budget Experiment
FAA	Federal Aviation Administration
FIRE	First ISCCP Regional Experiment
FIRE.ACE	First ISCCP Regional Experiment III Arctic Cloud Experiment
FWHM	Full Width at Half Maximum
GCM	General Circulation Model
GDS	Ground Data System
GEO	Geostationary Earth Orbit
GMS	Japan – Geostationary Meteorological Satellite
GOES	U.S. Geostationary Operational Environmental Satellite
GOME	Global Ozone Monitoring Experiment
HDF	Hierarchical Data Format
I/F	normalized EPIC radiance values
IMP-8	Interplanetary Monitoring Platform
INDOEX	Indian Ocean Experiment
IR	Infra-Red
ISCCP	International Satellite Cloud Climatology Project
ISEE	International Sun-Earth Explorer
L-1	Lagrange 1 point between the Earth and the Sun
L-2	Lagrange 2 point, beyond the Earth on the Earth-Sun line
LEO	Low Earth Orbit
LER	Lambert Equivalent Reflectivity
LOWTRAN	Radiative Transfer Program
LSM	Land System Model
LW	Longwave
MHD	Magnetohydrodynamics
MOC	Mission Operations Center
MODIS	MOderate-Resolution Imaging Spectroradiometer
MSG	Meteosat – European Space Agency Geostationary satellite
NCAR	National Center for Atmospheric Research
NCEP	National Center for Environmental Prediction
NIST	National Institute of Standards & Technology
NISTAR	Scripps-NIST Advanced Radiometers
NMC	U.S. National Meteorological Center
NOAA	National Oceanographic and Atmospheric Administration
NSF	National Science Foundation
OLR	Outgoing Longwave Radiation
PID	Process Identity
POEM	Polar-Orbit Earth Observation Mission
POLDER	Polarization and Directionality of Earth's Reflectances
PSC	Polar Stratospheric Cloud
PTC	Positive Temperature Coefficient
QE	Quantum Efficiency
RGS	Remote Ground Stations
SeaWifs	Sea-Viewing Wide Field Sensor

SHEBA	Surface Heat Budget of the Arctic
SMEX-Lite	Small Explorer
SNR	Signal to Noise Ratio
SOHO	Solar and Heliospheric Observatory
STEREO	Solar Terrestrial Relations Observatory
SW	ShortWave
SWE	Solar Wind Experiment
SZA	Solar Zenith Angle
TIROS	Television and Infrared Observational Satellite
TISA	Time and Space Averaging
TOA	Top of Atmosphere
TOMS	Total Ozone Mapping Spectrometer
TOVS	TIROS Operational Vertical Sounder
TRMM	Tropical Rainfall Mapping Mission
TSOC	Triana Science and Operations Center
UARS	Upper Atmospheric Research Satellite
VIRS	Visible Infrared Scanner
VZA	Viewing Zenith Angle
WIND	Solar Wind Observatory